2019

A path for microsecond structural health monitoring for high-rate nonstationary time-varying systems

Jonathan Hong
Iowa State University

A path for microsecond structural health monitoring for high-rate nonstationary time-varying systems

by

Jonathan Hong

A dissertation submitted to the graduate faculty

in partial fulfillment of the requirements for the degree of

DOCTOR OF PHILOSOPHY

Major: Civil Engineering (Intelligent Infastructure Engineering)

Program of Study Committee:
Simon Laflamme, Co-major Professor
Chao Hu, Co-major Professor
Jacob Dodson
Aleksandar Dogandzic
Anuj Sharma
In-Ho Cho

The student author, whose presentation of the scholarship herein was approved by the program of study committee, is solely responsible for the content of this dissertation. The Graduate College will ensure this dissertation is globally accessible and will not permit alterations after a degree is conferred.

Iowa State University

Ames, Iowa

2019

DEDICATION

I would like to dedicate this dissertation to my loving wife Jenny and to our precious children Isaiah and Eliana, whose love and encouragement were vital to the completion of this work.

TABLE OF CONTENTS

Page

LIST OF TABLES

Page

LIST OF FIGURES

Page

ACKNOWLEDGMENTS

I would like to take this opportunity to express my many thanks to those who helped me with various aspects of conducting this research. I have been very fortunate to have been afforded the best advisors, Dr. Simon Laflamme, Dr. Chao Hu, and Dr. Jacob Dodson. Their guidance, patience, and support have been instrumental to this research. Dr. Jason Foley, Dr. Janet Wolfson, Alex Gracia, Frank Fairchild, George Jolly, John Deep, the Fuzes branch under contract number FA8651-17-D-0002, Air Force Office of Scientific Research under award number FA9550-17-1-0131, and National Science Foundation under Grant No. 1300960 and 1463252 for making this research possible through entrusting me to conduct this research and the providing of financial support. Dr. Alain Beliveau, Dr. Dave Jerome, Dr. Jeff Hanes, Dr. Jeff Simmers, Dr. Joey Maestas, and Applied Research Associates Emerald Coast Division for their support and accommodation of my needs during this process. My committee members previously not mentioned, Dr. Aleksandar Dogandzic, Dr. Anuj Sharma, and Dr. In-Ho Cho, for challenging me to strive for higher heights. My collaborators, Dr. Austin Downey, Dr. Bryan Joyce, Dr. Liang Cao, Dr. Yelda Turkan, Jin Yan, Laura Micheli, and Nisha Puri. It was my pleasure working with you. My research colleagues, Alessandro Cancelli, Irvin Pinto, James Scheppegrell, Sangeeth Balakrishnan, and Yongqiang Gong, for the friendship and humor that has helped me through the difficult times. Others, whose names I may have forgotten, thank you. My father Dr. In-Gyu Hong and mother Kyung-Bok Hong for their prayers, support, and teaching me the value in education. My brother (future Dr.) Nathan Hong and sister Deborah Park for their love, encouragement, and companionship. My in-laws Myong Suk Kim, Richer Pak, Sei Kon Suh, Tami Kim, J.D., Dr. Joon Kim, Grace Hong, and Bruce Park for their unwavering support starting from my undergraduate years. And most importantly, I would like to thank God, Who has made this research possible through His Son, Christ Jesus.

ABSTRACT

In this dissertation, a new area of research identified as high-rate state estimation is established along with its associated research challenges, and a path for a solution is provided. High-rate dynamic systems are defined as systems being exposed to highly dynamic environments that are comprised of high-rate and high-amplitude events (greater than 100 g_n for a duration under 100 ms). Engineering systems experiencing high-rate dynamic events, including airbag, debris detection, and active blast protection systems, could benefit from real-time observability for enhanced performance. This task of high-rate state estimation is particularly challenging for real-time applications, where the rate of an observer's convergence needs to be in the microsecond range. On the other hand, the benefits include a high potential to reduce economic loss and save lives.

The problem is discussed in-depth addressing the fundamental challenges of high-rate systems. A survey of applications and methods for estimators that have the potential to produce accurate estimations for a complex system experiencing highly dynamic events is presented. It is argued that adaptive observers are important to this research. In particular, adaptive data-driven observers are found to be advantageous due to their adaptability to complex problems and lack of dependence on system model.

An adaptive neuro-observer is designed to examine the particular challenges in selecting an appropriate input space for high-rate state estimation to increase convergence rates of adaptive observers. It is found that the choice of inputs has a more significant influence on the observer's performance for high-rate dynamics when compared against a lower rate environment. Additionally, misrepresentation of a system dynamics through incorrect input spaces produces large errors in the estimation, which could potentially trick the decision making process in a closed-loop system in making bad judgments.

A novel adaptive wavelet neural network (WNN)-based approach to compress data into a combination of low- and high-resolution surfaces is proposed to automatically detect concrete cracks and other forms of damage. The adaptive WNN is designed to sequentially self-organize and self-adapt in order to construct an optimized representation. The architecture of the WNN is based on a single-layer neural network consisting of Mexican hat wavelet functions. The approach was verified on four cracked concrete specimens.

A variable input space concept is proposed for incorporating data history of high-rate dynamics, with the objective to produce an optimal representation of the system of interest minimizing convergence times of adaptive observers. Using the embedding theory, the algorithm sequentially selects and adapts a vector of inputs that preserves the essential dynamics of the high-rate system. The variable input space is integrated with a WNN, which constitutes a variable input observer. The observer is simulated using experimental data from a high-rate system. Different input space adaptation methods are studied and the performance is compared against an optimized fixed input strategy. The variable input observer is further studied in a hybrid model-/data-driven formulation, and results demonstrate significant improvement in performance gained from the added physical knowledge.

An experimental test bed, developed to validate high-rate structural health monitoring (SHM) methods in a controllable and repeatable laboratory environment, is modeled as a clamped-pinned-free beam with mass at the free end. The Euler-Bernoulli beam theory is applied to this unique configuration to develop analytical solutions of the system. The transverse vibration of a clamped-pinned-free beam with a point mass at the free end is discussed in detail. Results are derived for varying pin locations and mass values. Eigenvalue plots of the first five modes are presented along with their respective mode shapes. The theoretical calculations are experimentally validated and discussed.

CHAPTER 1. OVERVIEW

1.1 Introduction

This dissertation is a compilation of peer-reviewed journal articles that form the chapters. Chapter 2 presents the article titled, "Introduction to state estimation of high-rate system dynamics" [1], where a new area of research was identified. Systems undergoing harsh extreme environments also defined as high-rate dynamics (systems experiencing large accelerations/decelerations of > 100 g_n for a duration of <100 ms.) can and will often times experience a sudden plastic deformation to the structure or electronics. The damage can worsen exponentially with time, if left untreated. Rapid identification and mitigation methods can prevent catastrophic failure. It was identified that state estimation for these systems are more appropriate than damage identification methods to maximize the use of the system's remaining usable life.

An examination of high-rate systems revealed three distinct characteristics inherent to these systems. These include 1) large uncertainties in the external loads, 2) high levels of non-stationarities and heavy disturbances; and 3) generations of unmodeled dynamics from changes in system configuration. A brief yet thorough review of observers was conducted based on the needs of a high-rate system. Of the identified complexities of a high-rate system, adaptive observers were found to be the most applicable. Yet, the slow convergence of adaptive observers was an obstacle that needed to be addressed.

Chapter 3 presents the article titled, "Study of input space for state estimation of high-rate dynamics" [2]. The input space of an estimator is studied. Typical input spaces are comprised of sensor measurements as they become available. Rarely do observers optimize the input space. Using the embedding theorem [3], an input space is constructed using past data. The input space technique coupled with an adaptive neuro-observer demonstrated enhanced convergence times. The demonstration is made through simulations conducted on high-rate data acquired from a laboratory

environment. A fixed input space optimized over the entire data set ahead of time is compared with changes in the optimal input space. Through this study, it is established that the proper selection of input space can dramatically improve the performance of adaptive systems.

Chapter 4 presents the article titled, "Adaptive wavelet neural network for terrestrial laser scanner-based crack detection" [4]. An adaptive wavelet neural network estimator is applied to a point cloud of data acquired from a laser scanner for automatic crack detection. The adaptive wavelet neural network estimator is similar in construction as the adaptive neuro-observer used in the input space study [2]. The power of the estimator is demonstrated in its universal approximation capability.

Using Kohonen's self organizing network method [5], the percent overlap in wavelets is varied to control the resolution of estimates allowing for an initial course, yet more compact representation of the data. This course representation is scanned for high concentration of wavelets to determine crack locations. The crack location is then rescanned for a higher resolution representation to further analyze the crack to determine the condition of the structure. Thus an automatic crack detection strategy is introduced along with a method to compress the data for easy storage.

Chapter 5 presents the article titled, "Variable input observer for nonstationary high-rate dynamic systems" [6]. A novel variable input observer (VIO) is introduced. The embedding theorem [3], formally applicable only to stationary systems, is extended to nonstationary systems for the first time through the application to stationary segments of data. Using Mutual information (MI) theory [7] and false nearest neighbors (FNN) algorithm [8], the input space selection is automated. A smooth adaptation of the input space is proposed to eliminate error spikes and produce superior estimations compared with other input space adaptation approaches. Furthermore, integrating physical knowledge to the VIO, making it a hybrid observer, generated better results as opposed to a pure data-driven VIO.

Chapter 6 presents the article titled, "Transverse vibrations of clamped-pinned-free beam with mass at free end" [9]. The theoretical solution to a high-rate laboratory apparatus is provided. A laboratory apparatus defined as a clamped-pinned-free beam with mass at free end was designed and

built for validation of high-rate structural health monitoring techniques. Using the Euler-Bernoulli beam theory [10], the eigenvalues and mode shapes are calculated. The theoretical solution is validated through experimental data. For future studies, a path for algorithm validation is presented first through a laboratory apparatus designed with repeatable nonstationary time-varying parameters and second through a proposed hybrid observer.

Chapter 7 summarizes the key contributions of this research. More specifically, they are listed as follows.

- Chapter 2 established a new area of research identified as high-rate state estimation, identified three key research challenges as: 1) Large uncertainties in the external loads; 2) high levels of non-stationarities and heavy disturbances; and 3) generations of unmodeled dynamics from changes in system configuration, and presented a path to solving the problem through the use of adaptive data-driven observers determined by a literature search.

- Chapter 3 determines that proper input space selection has the ability to dramatically enhance the convergence times of adaptive observers.

- Chapter 4 validates an adaptive wavelet network through an application to automatic crack detection.

- Chapter 5 introduces a novel variable input observer with automatic input space selection using the embedding theorem. The application of the embedding theorem that was previously limited to stationary data sets is made applicable to nonstationary systems by applying the theorem to stationary segments of data. It also demonstrates a smooth transitioning method between input spaces for better estimations, and identifies that hybrid methods of adding knowledge of a system have the potential to outperform pure data- or model-driven strategies.

- Chapter 6 derives the theoretical solution to a high-rate laboratory apparatus identified as a clamped-pinned-free beam with mass at free end using the Euler-Bernoulli beam theory. The transcendental equation is derived for a general case of the system with arbitrary pin location and arbitrary mass.

1.2 References

[1] J. Hong, S. Laflamme, J. Dodson, and B. Joyce, "Introduction to state estimation of high-rate system dynamics," *Sensors*, vol. 18, no. 217, pp. 1–16, 2018.

[2] J. Hong, S. Laflamme, and J. Dodson, "Study of input space for state estimation of high-rate dynamics," *Structural Control and Health Monitoring*, vol. 25, no. 6, p. e2159, 2018.

[3] F. Takens, "Detecting strange attractors in turbulence," *Dynamical systems and turbulence, Warwick 1980*, pp. 366–381, 1980.

[4] Y. Turkan, J. Hong, S. Laflamme, and N. Puri, "Adaptive wavelet neural network for terrestrial laser scanner-based crack detection," *Automation in construction*, vol. 94, pp. 191–202, 2018.

[5] T. Kohonen, "The self-organizing map," *Neurocomputing*, vol. 21, no. 1–3, pp. 1–6, 1998.

[6] J. Hong, S. Laflamme, D. J. Cao, L., and B. Joyce, "Variable input observer for nonstationary high-rate dynamic systems," *Neural computing and applications*, pp. 1–12, 2018.

[7] A. Fraser and H. Swinney, "Independent coordinates for strange attractors from mutual information," *Physical Review A*, vol. 33, no. 2, pp. 1134–1140, 1986.

[8] M. Kennel, R. Brown, and H. Abarbanel, "Determining embedding dimension for phase-space reconstruction using a geometrical construction," *Physical Review A*, vol. 45, no. 6, pp. 3403–3411, 1992.

[9] J. Hong, J. Dodson, S. Laflamme, and A. Downey, "Transverse vibration of clamped-pinned-free beam with mass at free end," *Journal of sound and vibration (Submitted)*, 2019.

[10] S. Timoshenko and D. Young, *Vibration problems in engineering*. New York: Wiley, 1974.

CHAPTER 2. INTRODUCTION TO STATE ESTIMATION OF HIGH-RATE SYSTEM DYNAMICS

J. Hong, S. Laflamme, J. Dodson, and B. Joyce

Abstract

Engineering systems experiencing high-rate dynamic events, including airbags, debris detection, and active blast protection systems, could benefit from real-time observability for enhanced performance. However, the task of high-rate state estimation is challenging, in particular for real-time applications where the rate of the observer's convergence needs to be in the microsecond range. This paper identifies the challenges of state estimation of high-rate systems and discusses the fundamental characteristics of high-rate systems. A survey of applications and methods for estimators that have the potential to produce accurate estimations for a complex system experiencing highly dynamic events is presented. It is argued that adaptive observers are important to this research. In particular, adaptive data-driven observers are advantageous due to their adaptability and lack of dependence on the system model.

2.1 Introduction

High-rate dynamics are described as a dynamic response from a high-rate (<100 ms) and high-amplitude (acceleration > 100 g_n) event such as a blast or impact. Systems which experience high-rate dynamics may undergo rapid changes that could lead to loss of economic investment or human lives [1]. There are unique challenges associated with research of structural health monitoring for systems experiencing high-rate dynamics. A system subject to high-rate dynamic environments can often experience a sudden plastic deformation, and damage can extend to the structure, electronics, and/or sensors. Rapid state estimation for these systems can be used within a feedback loop to prevent further damage and complete failure [2]. For example, rapid detection is required in the deployment of a blast mitigation system or in adapting control decisions for a hypersonic vehicle following a ballistic impact. In the problem of high-rate dynamic systems, the state estimator needs to be fast as well as robust to large uncertainties, non-stationarities, and heavy disturbances. State estimation is required when the desired states cannot be directly measured [3]. The area of research has been pioneered by Wiener [4], which led to Kalman's work [5, 6]. Kalman adopted a practically structured approach, with applications found notably in the spacecrafts used in the Apollo and Polaris missions. Since then, optimal estimation research has substantially grown in popularity. In addition, advances in estimation and control theory, along with computer science, have enabled the development of observers with rapid convergence properties. Such observers have the potential to produce safer and smarter systems capable of responding to real-time events. In particular, the capability of an estimator on a mechanical system to sense, analyze, and predict the health of a system, while experiencing high-rate dynamic environments, could be invaluable for many different domains. However, this identification and adaptation task can only be conducted provided an in-time state estimation during the high-rate dynamic event, where high-rate is herein defined as the microsecond range.

The high-rate problem in mechanical systems contains many complexities that can be summarized as having

- large uncertainties in the external loads;

- high levels of non-stationarities and heavy disturbances; and
- generations of unmodeled dynamics from changes in system configuration.

A high-rate estimator must also be capable of handling these three main particularities that differentiate high-rate dynamic systems from other systems. State estimation is often required for high-rate systems because of the large levels of noise, uncertainties, and disturbances that contaminate the sensor outputs. However, the end goal of the state estimation could be different depending on the application. A popular application is damage or fault detection, in particular when a fast decision needs to be made to protect the integrity of the system, for instance a shutdown. Another application is in the adaption of physical models. For example, a different control law could be desirable for a damaged system. Whatever the application may be, state estimation is the first enabling step.

The objective of this paper is to analyze existing applications and methods of state estimation that could be useful in solving the high-rate state estimation problem for complex systems that may have nonlinear and time-varying dynamics. Advantages and disadvantages of each method, with the focus on microsecond convergence rates, capable of producing accurate estimations will be surveyed. The system's observability, or how well the system can be reconstructed from measurements, is a critical concept that underlies the mathematical constructs of state estimators. It is very difficult to formulate a fully observable model of a complex physical system with high-rate system dynamics [7]. Because the focus of this paper is on the high-rate estimators' performance, we do no go into details about the observability of these complex systems. Here, attention to what aspects negatively impact convergence of estimators and the comparison between observers will give insight into how convergence rates between observers may compare. In cases when simplicity versus complexity of estimators (i.e., for computation, properties, implementation, etc.) is mentioned, the connection should be made to convergence rates in the sense that simplicity correlates to faster convergence rates. However, the performance of observers is application-specific, and the findings will be dependent on the type of scenario. The observers presented were found to be most applicable to high-rate systems. The objective is to familiarize the reader with some key observer

background, and gain some insight into advanced techniques to improve observer performance with respect to the high-rate state estimation problem.

The rest of this chapter is organized as follows. Section 2.2 discusses applications where high-rate state estimation could be useful. Section 2.3 describes the specific challenges associated with state estimation of high-rate dynamics. Section 2.4 gives the background on general types of observers and their broad applications. Section 2.5 makes a case for adaptive observers and their application to high-rate dynamics. Section 2.6 discusses the key contributions of this research and the organization of this dissertation.

2.2 Applications for High-Rate State Estimation

This section discusses engineering systems for which high-rate state estimation can be particularly useful. Examples include civil structures exposed to blast, automotive safety systems against collisions, debris strikes to space shuttles, and aerial vehicles.

2.2.1 Civil Structures Exposed to Blast

The increase in number of terrorist attacks on civilian and military structures is a growing concern. One must also consider accidental events such as gas leaks, vehicular collisions, and chemical mishaps, all having the potential to cause instantaneous, important changes to civil structures. These important events have the potential to jeopardize the structural integrity resulting in partial or total loss. Passive blast mitigation strategies have been developed to absorb some shock. These methods include friction elements, laminated windows, hardened concrete, etc. [8, 9, 10]. However, passive mitigation techniques are limited in performance. As an improvement, semi-active and active mitigation methods have been researched and discussed.

One example of active blast mitigation is proposed by Wadley et al. in [11]. The authors discussed using high-speed actuators to deploy pre-compressed cellular material when a blast wave is detected. Electromagnetic emission sensors are capable of detecting the blast milliseconds before the wave arrival, therefore allowing time for the actuators to react. Using this technique, the

material is able to absorb the shock waves through momentum cancellation. This method offers a larger shock absorption potential over passive methods. Nevertheless, the method is not capable of adaptive actuation based on the blast dynamics. While the utilization of adaptive actuation may improve blast mitigation performance, the reliance on a control rule adds computational time, let alone the reaction time of the actuation. As an example, the time of arrival of a blast produced by a 10 kg Trinitrotoluene (TNT) fluctuates between 0.3 and 100 ms for a distance of 1 to 40 m, requiring the sensing, estimation, and actuation process to be less than the time of arrival. In this situation, a high-rate observer would be critical in enabling the technology.

2.2.2 Automotive Safety Systems against Collisions

Fatal car accidents are on the rise [12] and improvements in our current safety measures have potential to decrease this number significantly. Current research in this field is geared toward smarter safety systems. An example is seen in [13], where the authors proposed a stereovision-based sensing method using stereo cameras and intelligent algorithms. The system classifies the occupant to determine if a child is present or if one of the passengers is in an unsafe position before deploying airbags. Although airbags play an important role in saving lives [14], this method addresses the issue that airbag systems unfortunately do sometimes cause unnecessary or even fatal injuries [15]. The child detection aspect is rather simple in that it can be done at the moment the vehicle is started. However, the unsafe position calculation is more challenging due to the fact that the calculation has to be done as an accident is occurring, in a fraction of a second [16]. The authors use a thin plate spline algorithm to boast processing times of 960 ms for the entire operation. It follows that smart vehicle safety systems could benefit from a high-rate observer robust to the nonstationary behaviors of the human body. It may, similar to the blast mitigation technology, enable the integration of more complex and better performing feedback systems.

2.2.3 Space Shuttle and Aerial Vehicles Prone to In-Flight Anomalies

The loss of the Columbia space shuttle in 2003 has brought light to the destructive potential of debris strikes. During the launch phase, a piece of insulating foam broke off and impacted the leading edge of the left wing, while traveling at a velocity of 705 m/s [17]. This caused a breach in the thermal protection system ultimately leading to the destruction during re-entry [18]. This catastrophe led to the research and development of the NASA Debris Radar (NDR). The NDR uses sophisticated methods to target and track debris during launch. It is also capable of automatic debris characterization assigning ballistic numbers to assess the material type, size, release location, and threat associated with the object [19]. However, the NDR is an offsite ground radar system. There are scenarios where ground intervention is not possible, for instance during communication delays or visibility limitations. Furthermore, the NDR only provides information during ascent. In the case of Columbia, the damage occurred during launch, but the loss occurred during re-entry. It follows that an onboard spacecraft structural health monitoring system could improve the in-time detectability of damage. Analogous to space shuttles, aerial vehicles often face the possibility of damage arising from impact with foreign objects including bird, hail, and lightning strikes. Any damage during flight can cause issues in dangerous navigational uncertainties. Because of the speed at which space shuttles and aerial vehicles travel and the rate at which damage may occur, a high-rate estimator has the potential to substantially improve safety through early detection of anomalies.

In addition, the aerospace industry is making advancements in hypersonic aerial vehicles and airframes that have the possibility of facing challenges similar to those of space shuttles. Hypersonic is defined as speeds of Mach 5 or greater [20]. Mach 5 at an altitude of 10,000 m and -50 °C corresponds to 1.5 km/s (0.93 mi/s). In comparison, the average Boeing passenger aircraft cruises at 600 mph or about Mach 0.8. It follows that a hypersonic vehicle travels at speeds at least six times greater than conventional passenger airplanes. At these speeds, there are possibilities for problems to quickly turn catastrophic. For instance, the distance traveled at Mach 5 is equivalent

to 1.5 m (4.9 ft) over 1 ms. A 1.5 MHz sampling rate is necessary to obtain a 1 mm (0.04 in) travel resolution, thus requiring a high-rate observer.

2.3 Challenges in State Estimation for Systems Experiencing High-Rate Dynamics

State estimation of high-rate dynamics offers unique challenges. By definition of high-rate, estimators applicable to this research area will require rapid convergence. Take the hypothetical example of a civil structure exposed to blast equipped with an actively controlled protection system. The large uncertainties in the external loads appears in the form of lack of knowledge on the blast. The time, location, and size of the blast are all unknown. When a structure experiences a blast, it is likely to experience some damages, which amount to non-stationarities and heavy disturbances. Structural damage will result in the generation of unmodeled dynamics in the form of changes in dynamic parameters, which will affect the controller performance. In this section, we describe the details of the complexities associated with high-rate systems.

2.3.1 High-Rate Systems-Specific Challenges

More precisely, high-rate systems are characterized by system complexities to include noise, uncertainty, unknown inputs, time varying parameters/states, and disturbances. Due to the high amplitude of events, noise can be introduced in many ways such as metal parts chattering at interfaces, circuit boards flexing, etc. There are many uncertainties in high-rate systems due to material response at high rates of loading being unknown [21] as well as uncertainties in boundary conditions. Unknown inputs are due to environmental influences that excite the system, and may include different dynamics, levels of chaos, and amplitudes for a single system. High-rate systems normally contain some time-varying component that results from damage or changes in mechanical configuration from deformation of parts. In addition, disturbances may be present from the turbulent nature of the system which may excite resonances at the system or sensor levels. The

challenges to making accurate estimations in the presence of these system complexities are briefly discussed in what follows.

Conventional estimators fail at quickly estimating states when noise and uncertainties are present [22]. In practical applications, noise may arise from sensor measurements, algorithm implementation, contaminating estimation values, etc. The KF can be used to suppress noise if the noise function is appropriately built into its architecture. This noise suppression comes with added computational costs. To reduce the convergence time, the observer gain may be increased. This, however, can negatively impact the precision of the estimation as the noise can be amplified. One solution is a Uniform Robust Exact Observer (UREO) as proposed in [23]. It is tunable, and can achieve optimal convergence, while maintaining precision under measurement noise.

Uncertainty is another common issue for many practical applications. For example, a major challenge for observer-driven algorithms used to estimate reaction rates in stirred tank bioreactors is in the difficulty of modeling the growth kinetics of micro-organisms [24]. Various techniques have been researched to deal with system uncertainties. For structural damage detection, methods for the formulation of objective functions using incomplete model data have been developed [25]. Self-tuning fusion Kalman filters based on steady-state Riccati equations are demonstrated for systems with completely unknown model parameters and noise variances [26].

There are cases for which the inputs to the system are unknown due to lack of sensors or faults in the system. For these cases, special design considerations can be made to guarantee accurate state or parameter estimations. In particular, the High Gain Observer (HGO) in [27] incorporates an auxiliary-variable to estimate unknown unsteady inputs. Reference [28] describes the usefulness of an Unknown Input Observer (UIO) for making estimations when only the output to estimate state variables is available. Originally, UIOs for a plant could be designed if and only if the plant was of minimum phase. Further development of the UIO in [28] provides alternatives to the minimum phase condition. UIO for nonlinear systems with both noise and uncertainties also require further research. One possibility is presented in [22], where a robust UIO for nonlinear systems is capable of handling both noise and uncertainty.

System models containing nonlinearities other than those from the time-varying parameters are termed parameter varying nonlinear (PVNL) systems. A sufficient condition for asymptotic convergence is developed for a two degree-of-freedoms Arcak nonlinear observer in [29]. The Arcak observer form contains two observer gain matrices of which the method is extended to optimize the second observer gain. The technique is further augmented to PVNL systems using finite dimensional relaxation method for quadratic parameter dependent Linear Matrix Inequalities (LMI).

Systems operating at high-speeds may encounter unmodeled higher order dynamics, which can cause resonance, also considered as disturbances. Such resonance can lead to a decrease in estimation performance and irregular accuracy. Disturbance observers (DOB), usually used in control applications, estimate a disturbance using a low-pass filter and an inverse of the nominal model. The estimated signal is used to cancel disturbances within a system, which in turn makes the system robust to uncertainties and disturbances [30]. In general, high robustness is difficult to achieve using DOB because of estimation delays attributed to pole allocation. A position-acceleration integrated disturbance observer (PAIDO) was proposed as a high-performance DOB [31]. The PAIDO structure incorporates accelerometer measurements to enlarge the frequency bandwidth of the disturbance estimation to provide better robustness [32].

Another challenge is that many of the above mentioned techniques add complexities to the estimation algorithms, which slow the computational time. The decrease in computational time is another big hurdle for high-rate estimation for obvious reasons. The next section will give an example of a high-rate laboratory experiment and argue that a simple fast estimator is not sufficient for high-rate systems.

2.3.2 High-Rate Dynamic Example

An example of a high-rate laboratory experiment is shown in Figure 2.1. Figure 2.1(a) is a picture of an MTS-66 drop tower designed to generate various impact conditions. In Figure 2.1b is an electronics unit which consists of four circuit boards with high-g Meggitt 72 accelerometers mounted on each. These high-g accelerometers are able to accurately measure accelerations of

120,000 g_n or 120 kg_n [33], where 1 g_n = 9.81 m/s^2 = 32.2 ft/s^2. The electronics are potted in the canister with potting material to secure all parts in place. Figure 2.1c shows the deceleration profile from three different tests, exhibiting varying time series behaviors for all three tests. These differences are attributed to the complex high-rate nature of the experiment.

Although the experimental setup may appear simple, this high-rate problem contains many complexities. When the drop tower is operated, the cables, which are hardwired from the accelerometers to the data acquisition system, whip violently adding noise to the measurements. Careful consideration in wires are taken to minimize the noise effect, but noise cannot be eliminated. The metal interfaces rattle upon large impacts, also adding noise. The uncertainties in this example include the unknown high-rate response of the circuit board and potting materials, and the unknown changing boundary conditions such as the bond of the potting material to the interior of the canister. The precise input to the system resulting from the drop tower impact is unknown. Disturbances created from sensor and/or system resonance is not obvious in these tests, however, it is not uncommon in larger impact tests.

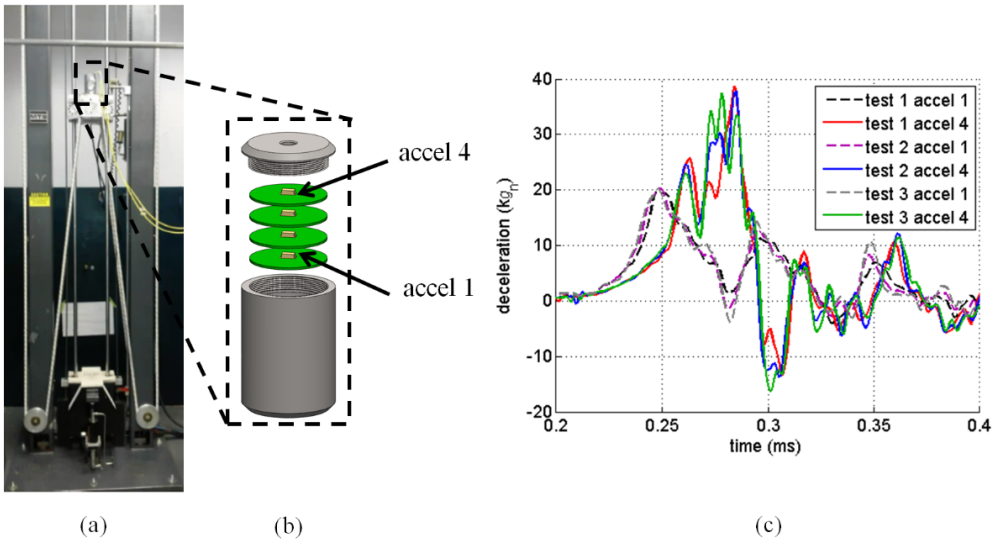

Figure 2.1: Experimental setup: (**a**) MTS-66 drop tower; (**b**) electronics unit; and (**c**) deceleration from three tests.

The deceleration event in drop tower tests typically lasts for 0.5 ms. Due to the short duration of high-rate events, fast estimators are required. Furthermore, the estimator must be capable of handling system complexities mentioned above. In contrast, examples of fast estimators can be seen in the sensorless control of induction motors or alternating current (AC) motors, commonly used in industrial applications [34]. Different methods have been explored for estimating states of induction motors. Bodson et al. in [35] demonstrate precise motor controls in 73 ms using backward difference for the position measurement using low-pass filtering with a nonlinear observer constructed using a mathematical model of the system. Xu et al. in [36] show an adaptive sliding observer capable of a computation time for one update of 19 µs, and an Extended Kalman Filter (EKF) capable of 86 µs using a 250 MHz processor. Zhang et al. in [37] compare the performance of a Luenberger observer (LO), sliding mode observer (SMO), and an EKF. Using a 150 MHz processor, one update took the LO and SMO 5 µs to converge, while the EKF took 100 µs. These observers demonstrate the capability of performance in the microsecond range appealing to the high-rate problem.

While the research efforts surveyed above represent important progress in state estimation, in most cases a particular state-estimator type addresses a specific system complexity challenge. As argued previously, the critical challenge with high-rate state estimation is associated with the presence of most of the discussed complexities in a single system. In the next section, a brief survey on observers is conducted to develop a foundation for a potential solution. The survey is intended to provide the reader with a broad background to understand the possible impact that the choice of an observer may have on systems experiencing high-rate dynamics.

2.4 Background on Observers and Their General Applicability

This section reviews typical families of observers in view of the applicability to the state-estimation problem. The most simplistic class of observers are those designed for linear and idealized systems. Such observers have, typically, fast computation time and convergence due to the triviality of computations. The Luenberger Observer (LO) [38] is a classic observer used for linear systems

with well-defined numerical models. The LO has proven itself to be valuable in the areas of system monitoring and regulations, detecting, and identifying failures in dynamic systems [39]. However, since the LO is heavily dependent on the mathematical model of the system, disturbances, dynamic uncertainties, and nonlinearities can be particularly challenging. The KF [40] can be used in linear applications where noise is present and characterized as Gaussian [36]. The reason for the word "filter" stems from the fact that the algorithm filters through noisy data to converge to accurate estimations. While the KF typically produces estimations with higher accuracy than the LO, its implementation is more complex [37] due to possibly unmodeled nonlinearities in the system model and ill-conditioning of the covariance matrix [41]. The Sliding Mode Observer (SMO) [42] can be an alternative to provide very good robustness [43, 44, 45, 46, 47], but is sensitive to the choice of gain [48]. The SMO exhibits ripples in the presence of external noise [37].

Tuning of observers for linear systems can be conducted through the pole placement method. The pole placement method allows the tuner to determine observer gain matrix values based on the desired eigenvalues for system stability and convergence. The preferred location of the eigenvalues depends on the application. Generally, the further to the left in the complex plane or the more negative the real part of the pole, the faster the convergence rate. Placing the poles too far left may amplify noise [49]. The LO, KF, and SMO may exhibit high convergence rates for linear systems. However, the majority of practical problems are nonlinear and complex. For this reason, observers built for nonlinear systems are more appropriate for applications to the high-rate state estimation problem. They are discussed in what follows.

2.4.1 Observers for Nonlinear Systems

Observers for nonlinear systems can be classified into three main estimation methods: data-driven, statistical, and model-driven methods [50]. Popular data-driven methods include nonlinear autoregressive moving average (NARMAX) models [51], fuzzy logic [52] and neural network (NN) estimators [53]. The performance of data-driven method is linked to the quality of data mining and interpretation algorithms, and an additional limitation can be found in the computational time

required to achieve an appropriate estimate [54]. Data-driven methods were developed as tools to process information without knowledge of a system's dynamics, particularly useful for handling very complex systems. For instance, Geetha et al. [55] compared the performance of an NN and an Extended Kalman Filter (EKF) based state filter for the application to a Continuous Stirred Tank Reactor (CSTR). The performance metric indicated that the NN displayed smaller errors in the estimations over a unit sampling time than the EKF, because the CSTR had complex, nonlinear dynamics, which are difficult to characterize.

Statistical methods include Least Squares Estimator (LSE) [56], Maximum Likelihood Estimator (MLE) [57], and Particle Filters [58]. The advantage of statistical methods is the probabilistic prediction capabilities based on known parameters. These techniques can be used for nonlinear models with non-normal data. They bypass the need for linearized dynamic equations allowing global convergence of estimations. Statistical methods with simple properties such as the Least Squares method are popular in control, signal processing, and prediction theory applications. For instance, Ortega [59] discusses a method for reducing an online Least Squares parameter estimator to a set of regression vectors, which guarantees a finite convergence time. The weakness of this approach is the algorithm's extreme sensitivity to noise. Franzho and Sherman [60] introduced a minimum variance spectral estimator, also known as Capon's maximum likelihood spectral estimator, that converges to a signal point spectrum even with no knowledge of the noise spectral characteristics, making it robust to contaminating noise types. Bai et al. in [61] proposed a robust statistical estimator that takes an analytic center approach for bounded error parameter estimation. The analytic center estimate minimizes the logarithmic average output error and can be implemented in a sequential form. This method comes with increased computational complexity. In [62], a Modified Recursive Least Squares estimation technique was developed for adaptive control applications were the weaker sufficiently exciting [63] condition is more likely to be satisfied than the stronger persistently exciting [64] condition. A general limitation of statistical methods is the reliance on available data sets for training and/or extraction of probability distribution functions.

Model-driven methods include the EKF, Unscented Kalman Filter (UKF), variations of the SMO, HGO, Nonlinear Extended State Observer (NESO), Robust State Estimators (RSE), and many more. The EKF uses a linear approximation of the nonlinear system [65] either by taking the derivative of the nonlinear function or by applying a Taylor series expansion to the desired order of the approximation. Depending on the order of the approximation, the observer is termed reduced, full, or higher order [41]. A challenge with the EKF is the linearization of the system making the corresponding propagation equations available only to the neighborhood of the estimate [66]. The EKF can be difficult to implement, difficult to tune, and highly unstable unless the system is nearly linear on the time scales of the update calculations [67]. It requires longer time for convergence compared with the LO and SMO as its computations are more complex [37]. The EKF is also difficult to apply to nonlinear systems with time varying parameters, particularly in the presence of noise [24]. The UKF uses the true nonlinear model and approximates a Gaussian distribution of the state random variable. The UKF avoids the use of complex Jacobian and Hessian matrices, making it easier to implement than the EKF with simpler computations [68]. Crassidis and Markley [69] demonstrated the superiority of the UKF with respect to the EKF in terms of accuracy, computational costs, and ease of implementation. Charles et al. [70] discussed the Utkin and Walcottzak variations of the SMO observers, both being robust estimators. However, both variations of the SMO underperform in the estimation of states when some inputs are unavailable. HGO uses a sufficiently high observer gain that will guarantee good performance of the observer in terms of accuracy and speed of convergence [71]. For most cases, the HGO is used as an LO-type estimator with large gain and the application is for estimating slowly varying states or inputs [27]. A disadvantage of the HGO is strong chattering when the gain is very large [72]. The NESO actively estimates the states, uncertainty, and unknown disturbances even when the system is unknown [73, 29]. The RSE guarantees robustness of the designed estimator if time invariant nominal system matrices, constant filter design parameters, and stationary external inputs conditions are met. The computational complexity is comparable with that of the KFs [74].

There are other model-driven observers used to estimate nonlinear systems. To name a few, in [75], an SMO was implemented on a system that was linearized using global linearization. Ticlea and Besancon [76] discussed an immersion-based observer design, where the dimension of the state is increased beyond what is done in the ESO, in order to obtain a new representation better suited for observer design. The Fokker-Planck Equations (FPE) are used to transform space and time fractional partial differential equations to a system of ordinary differential equations that are more easily solved [77], which could reduce computational time. Daum in [78] designed an exact nonlinear recursive filter where instead of linearizing nonlinear equations as conducted with the EKF, the filter solves a special class of nonlinear problems exactly with comparable computation complexity to the EKF. The coordinate transformations with output injections method is studied in [79, 80, 81, 82]. The authors in [83] propose a dynamic observer using the Moore-Penrose generalized matrix inverse of the state matrix. The model-driven estimation method has attracted much attention because it can produce accurate state estimations when it is not possible or practical to have sensors to characterize every state [84]. Furthermore, the mathematical models required for control purposes are readily available [85]. Table 2.1 summarizes the observers discussed in this section in terms of general applicability to the problem of high-rate state estimation.

2.5 Adaptive Observers

A useful tool to cope with the problem of system complexities are adaptive observers (AOs). AOs can be used to estimate states and parameters using input-output measurements, ideal for handling uncertainty in state estimation [86]. They are typically characterized by asymptotic stability but slow convergence rates [87]. These observers are often modifications of the observers discussed in Section 2.4 that use linear transformations, such as the LO, SMO, and versions of the KF. In particular, adaptive observers have been proposed to estimate the unmeasurable states for different classes of nonlinear systems [88].

Adaptive versions of the HGO and the EKF have been studied in [89]. The high gain aspect of the HGO serves to eliminate the nonlinear part of the system, while allowing rapid convergence,

Table 2.1: Summary of observers in terms of general applicability to the problem of high-rate state estimation.

Observer Type	Application to High-Rate State Estimation	Reference
Luenberger Observer (LO)	Very fast convergence rates, but generally applies to linear systems with precise nominal models, thus inadequate for high-rate problem.	[39]
Sliding Mode Observer (SMO)	High robustness and improved results for inaccurate models, but sensitive to choice of gain limiting the convergence rate.	[43, 44, 45, 46, 47, 48]
Extended Kalman Filter (EKF)	High accuracy for nonlinear systems with added noise, but complex implementation leading to poor convergence rates.	[41, 37]
Unscented Kalman Filter (UKF)	Better convergence rates and higher accuracy than the EKF for it uses true nonlinear model, avoids complex Jacobian and Hessian matrices, and is easier to implement.	[68]
High-Gain Observer (HGO)	Accurate and fast convergence rates for estimating slowly varying states or inputs making it inadequate for high-rate problems.	[71, 27]
Nonlinear Extended State Observer (NESO)	Offers robustness to system uncertainty and external disturbances. Outperformed both HGO and SMO in a comparative study.	[73, 39]
Robust State Estimator (RSE)	Guarantees robustness for time invariant systems, constant filter design parameters, and stationary external inputs, however the convergence rate is similar to Kalman Filters.	[74]

thus making it a good candidate for nonlinear systems. On the other hand, the EKF filters out system or process noise, therefore advantageous for field applications. The two were combined to create a high-gain extended Kalman filter (HG-EKF) [89], which possesses the advantages of both estimators. The authors showed that the resulting HG-EKF could converge at a desired speed with the tuning of only one parameter, while also being capable of noise rejection. Although promising, a key issue with the HG-EKF is with the exponential convergence occurring only at the beginning of the estimation process from the initial condition. Large perturbations in the system are difficult to estimate if they are not already modeled within the system. This issue was overcome with the development of the adaptive gain extended Kalman filter (AG-EKF) [89]. The main advantages of this observer are the noise rejection and the ability to estimate perturbations. The trade-off is that the convergence rate of the AG-EKF is slower than the HGO or HG-EKF due to the algorithm's complexity.

While showing great promise, AOs are known to have slower convergence rate. In related studies, Shahrokhi and Morari [87] attributed this problem to the utilization of single observation errors. An arbitrarily fast convergence rate is achieved with the use of a discrete identifier, which

uses multiple output errors. Global asymptotic stability is assured for sufficiently rich inputs. This method is shown to be robust and insensitive to input types and initial conditions. Khaytati and Zhu [88] identifies that complicated adaptation laws are the cause of slow convergence. As a solution, an adaptive observer with exponential parameter estimation dynamics for nonlinear systems with unmeasured regression terms is introduced, requiring Lipschitz and bounded nonlinearity constraints. In this AO configuration, a parameter can be selected as large enough to increase the rate of convergence. However, if the value is too large, it will attenuate the gain matrix. Rajamani [90] shows that the stability of the system is not based on eigenvalues alone. The eigenvalues have to be located sufficiently far left in the complex plane and the eigenvectors need to be sufficiently well-conditioned. This condition is limited in the sense that the Lipschitz constant of the nonlinear part has to be small. To obtain less conservative results, a generalized Lipschitz condition is used in conjunction with an adaptive observer for a wider class of nonlinear systems [3]. Byrski and Byrski [91] proposed a modification of a modulating functions method (MFM), which enables rapid identification of step changes to parameters with minimal time delays in the estimations. There are several different solutions to increasing the rate of convergence for adaptive observers as potential candidates to high-rate estimation problems as previously discussed and summarized in Table 2.2.

Table 2.2: Adaptive observer addressed challenges and solutions to increase convergence rates.

Addressed Challenge	**Solution**	**Reference**
Sensitivity to noise	HG-EKF	[89]
Sensitivity to large perturbations	AG-EKF	
Arbitrary fast convergence	Using multiple output errors	[87]
Adaptation laws	Exponential parameter estimation	[88]
Broad applicability	Generalized Lipschitz condition	[3]
Fast identification of step changes	MFM	[91]

Model-driven methods have the advantage of providing precise measures of damage due to the availability of models, therefore enabling condition assessment and system prognosis. However, they require knowledge of the physical model, which is a difficult task for real-world systems. Additionally, high-rate systems may experience changes in the structure requiring different model

parameters than initially specified. Statistical methods can identify faults through a probabilistic measure, and may be used to conduct prognosis by evaluating the probability of faults, but require knowledge of probability distribution functions. The statistical properties are usually calculated from numerous tests, which is difficult to achieve for high-rate systems. Data-driven methods, in general, can provide accurate estimations based on pattern recognition and classification. Alternatively, they require precise examples and extensive training over available data set. Due to the spontaneous occurrence of high-rate events, little insight is provided in the external loads and system changes. Model- and statistics-driven methods will require significant developments to be applicable to high-rate systems.

Adaptive data-driven methods, on the other hand, can be seen as black-box systems capable of handling uncertainties found in state estimation [86]. These methods were developed as tools to process information without any knowledge of a system's dynamics. This makes data-driven methods particularly useful for dealing with very complex systems. Geetha et al. in [55] compared an NN estimator against an EKF-based state filter for continuous stirred tank reactors. The results of the study indicated smaller errors in the estimations over a unit sampling time with the use of NN estimators over the EKF due to the complex nonlinear dynamics difficult to characterize. DeCruyenaere et al. in [92] showed that data-driven neural networks were generally capable of outperforming KFs particularly when the system includes nonlinearities or non-Gaussian process noise. Mosavi in [93] showed that, while Kalman filters had higher accuracy in global positioning systems, recursive neural networks offered overall better performance due to their faster computations times.

Hybrid approaches also count advantages by combining strengths in model- and data-driven techniques. A model-driven approach can supplement data-driven methods by accounting for already understood dynamics. Conversely, data-driven methods can supplement a model-driven observer by approximating complex or difficult-to-model processes. For example, Psichogios et al. in [94] used a neural network to capture the complex, nonlinear growth rate of bacteria in a bioreactor that could then be used in a first-principles system model to find the overall biomass concentration. Hu et al. in [95] used a multiscale framework approach with EKF to make state-

of-charge and capacity estimation. These examples demonstrate the need for data-driven methods for complex systems. This characteristic of the adaptive data-driven method may be particularly useful for high-rate systems, which face similar challenges.

2.6 Conclusions

High-rate state estimation is a challenging task especially for complex engineering systems requiring real-time observability to ensure adequate performance. Example applications discussed civil structures exposed to blast, automotive safety systems, and space shuttle and aerial vehicles prone to in-flight anomalies. These examples highlighted the high potential of high-rate state estimators to improve the resiliency of high-rate engineering systems and save lives. The paper presented a survey of existing applications and methods for state estimation that could be useful in solving the high-rate state estimation problem.

The specific challenges associated with the high-rate problem were presented. They include large uncertainties on external loads, high levels of non-stationarities and heavy disturbances, and generations of unmodeled dynamics from mechanical changes. An induction motor study was presented to make a distinction between high-rate systems and fast systems. Additionally, a variety of observers developed to compensate for system complexities of noise, uncertainty, unknown inputs, time varying parameters/states, and disturbances to improve on performance were discussed. However, these observers do not address the combination of these challenges which forms the high-rate problem.

In providing a discussion on the suitability of various observers, the strengths and weaknesses of various methods were introduced at a broad level. Three main categories of observers were reviewed: data-driven, statistical-driven, and model-driven observers. Generally, data-driven observers are advantageous when the complexity of a system does not allow for an accurate physical representation. Statistical methods perform well when prior data is available to produce a good understanding of the statistical properties of the system's behavior. Model-driven observers produce fast and accurate estimations for systems with well defined models. The discussion extended to adaptive versions of these observers, termed adaptive observers (AOs). It was argued that given

the complex nature of high-rate systems, data-driven observers have a particular promise because of the difficulty with creating a representation, and that specifically their adaptive form can be leveraged to adapt to large levels of uncertainties and complexities. However, AOs are characterized by slow convergence. Work addressing AOs' convergence has been reviewed, and it was concluded that work remains to be done in producing fast AOs.

Of particular interest is the utilization of AOs in hybrid configurations, which may take advantage of prior knowledge on a system for improved performance. They can be leveraged to replace dynamics too complex to model with a data-driven approach, possibly leading to significantly improved computational time. It follows from the discussion presented in this paper that adaptive observers and hybrid observers offer a path to developing high-rate observers capable of microsecond estimation.

2.7 References

[1] R. Lowe, J. Dodson, and J. Foley, "Microsecond prognostics and health management," *IEEE Reliability Society Newsletter*, vol. 60, pp. 1–5, 2014.

[2] J. Connor and S. Laflamme, *Structural Motion Engineering*. Springer International, 2014.

[3] M. Ekramian, F. Sheikholeslam, S. Hosseinnia, and M. Yazdanpanah, "Adaptive state observer for lipschitz nonlinear systems," *Systems & Control Letters*, vol. 62, no. 4, pp. 319–323, 2013.

[4] A. Gelb, "Dual contributions of optimal estimation theory in aerospace applications," *IEEE Control Systems Magazine*, vol. 6, no. 1, pp. 3–13, 1986.

[5] R. Kalman, "A new approach to linear filtering and prediction results," *Journal of Basic Engineering*, vol. 82, no. Series D, pp. 35–45, 1960.

[6] M. Grewal and A. Andrews, "Applications of kalman filtering in aerospace 1960 to the present," *Journal of Basic Engineering*, vol. 3, no. 3, pp. 69–78, 2010.

[7] L. Guo, Y. Guo, S. Billings, and D. Coca, "Approximate observability of infinite dimensional bilinear systems using a volterra series expansion," *Systems and Control Letters*, vol. 75, pp. 20–26, 2015.

[8] L. H. Lin, E. Hinman, H. F. Stone, and A. M. Roberts, "Survey of window retrofit solutions for blast mitigation," *Journal of Performance of Constructed Facilities*, vol. 18, no. 2, pp. 86–94, 2004.

[9] Y. Zhengqiang, L. Aiqun, and X. Youlin, "Fluid viscous damper technology and its engineering application for structural vibration energy dissipation," *Journal of Southeast University (Natural Science Edition)*, vol. 32, no. 3, pp. 466–473, 2002.

[10] E. Hinman, "Blast safety of the building envelope," *Whole Building Design Guide, National Institute of Building Sciences*, 2005.

[11] H. N. Wadley, K. P. Dharmasena, M. He, R. M. McMeeking, A. G. Evans, T. Bui-Thanh, and R. Radovitzky, "An active concept for limiting injuries caused by air blasts," *International Journal of Impact Engineering*, vol. 37, no. 3, pp. 317–323, 2010.

[12] "Transportation." https://www.census.gov, 2012.

[13] S.-J. Lee, M.-S. Jang, Y.-G. Kim, and G.-T. Park, "Stereovision-based real-time occupant classification system for advanced airbag systems," *International Journal of Automotive Technology*, vol. 12, no. 3, pp. 425–432, 2011.

[14] B. Meier, "Study shows air bags save lives, but says seat belts are needed, too," *The New York Times*, 1992.

[15] K. Cunningham, T. Brown, E. Gradwell, and P. Nee, "Airbag associated fatal head injury: Case report and review of the literature on airbag injuries," *Journal of Accident & Emergency Medicine*, vol. 17, no. 2, pp. 139–142, 2000.

[16] R. Din, "Injuries of the foot and ankle joint and their mechanisms," *Societatea Inginerilor de Automobile*, 2004.

[17] J. D. Walker, "From columbia to discovery: Understanding the impact threat to the space shuttle," *International Journal of Impact Engineering*, vol. 36, no. 2, pp. 303–317, 2009.

[18] D. Smith, "Megalightning and the demise of sts-107 space shuttle columbia: A fresh look at the available evidence." http://www.columbiadisaster.info, 2009.

[19] B. M. Kent, "Return-to-flight electromagnetic measurementsthe nasa shuttle ascent debris radar system," in *8th European Conference on Antennas and Propagation*, pp. 1–3, IEEE, 2014.

[20] "Hyersonic." http://www.merriam-webster.com, 2016.

[21] H. Kolsky, "An investigation of the mechanical properties of materials at very high rates of loading," *Proceedings of the Physical Society. Section B*, vol. 62, no. 11, p. 676, 1949.

[22] S. Mondal, G. Chakraborty, and K. Bhattacharyya, "Robust unknown input observer for nonlinear systems and its application to fault detection and isolation," *Journal of Dynamic Systems, Measurement, and Control*, vol. 130, no. 4, pp. 1–5, 2008.

[23] L. Fraguela, M. T. Angulo, J. Moreno, and L. Fridman, "Design of a prescribed convergence time uniform robust exact observer in the presence of measurement noise," *IEEE 51st Annual Conference on Decision and Control*, pp. 6615–6620, 2012.

[24] R. M. F. Oliveira, E. Ferreira, F. Oliveira, and S. Azevedo, "A study on the convergence of observer-based kinetics estimators in stirred tank bioreactors," *Korean Institute of Chemical Engineers*, vol. 6, no. 6, pp. 367–371, 1994.

[25] S. S. Kourehli, A. Bagheri, G. G. Amiri, and M. Ghafory-Ashtiany, "Structural damage detection using incomplete modal data and incomplete static response," *KSCE Journal of Civil Engineering*, vol. 17, no. 1, pp. 216–223, 2013.

[26] G.-L. Tao and Z.-l. Deng, "Convergence of self-tuning riccati equation for systems with unknown parameters and noise variances," in *8th World Congress on Intelligent Control and Automation (WCICA)*, pp. 5732–5736, IEEE, 2010.

[27] K. Stricker, L. Kocher, D. Van Alstine, and G. M. Shaver, "Input observer convergence and robustness: Application to compression ratio estimation," *Control Engineering Practice*, vol. 21, no. 4, pp. 565–582, 2013.

[28] K. Yamada and M. Kobayashi, "A design method for unknown input observer for non-minimum phase systems," in *International Workshop and Conference on Photonics and Nanotechnology*, pp. 1–6, International Society for Optics and Photonics, 2007.

[29] Y. Wang, R. Rajamani, and D. M. Bevly, "Observer design for differentiable lipschitz nonlinear systems with time-varying parameters," in *53rd Annual Conference on Decision and Control (CDC)*, pp. 145–152, IEEE, 2014.

[30] B. K. Kim, W. K. Chung, and K. Ohba, "Design and performance tuning of sliding-mode controller for high-speed and high-accuracy positioning systems in disturbance observer framework," *IEEE Transactions on Industrial Electronics*, vol. 56, no. 10, pp. 3798–3809, 2009.

[31] T. Yoshioka, T. T. Phuong, A. Yabuki, K. Ohishi, T. Miyazaki, and Y. Yokokura, "High-performance load torque compensation of industrial robot using kalman-filter-based instantaneous state observer," *IEEJ Journal of Industry Applications*, vol. 4, no. 5, pp. 589–590, 2015.

[32] S. Katsura, K. Irie, and K. Ohishi, "Wideband force control by position-acceleration integrated disturbance observer," *IEEE Transactions on Industrial Electronics*, vol. 55, no. 4, pp. 1699–1706, 2008.

[33] A. Beliveau, J. Hong, J. Coker, and N. Glikin, "COTS piezoresistive shock accelerometers performance evaluation," *Shock and Vibration Exchange*, vol. 83, pp. 1–10, 2012.

[34] R. Shahnazi, Q. Zhao, A. H. A. Sari, and T. Jeinsch, "Dynamic nonlinear unknown input observer for fault detection of induction motors," *23rd Iranian Conference on Electrical Engineering (ICEE)*, pp. 823–828, 2015.

[35] M. Bodson, J. Chiasson, and R. T. Novotnak, "Nonlinear speed observer for high-performance induction motor control," *IEEE Transactions on Industrial Electronics*, vol. 42, no. 4, pp. 337–343, 1995.

[36] Z. Xu, F. Rahman, and D. Xu, "Comparative study of an adaptive sliding observer and an ekf for speed sensor-less dtc ipm synchronous motor drives," in *Power Electronics Specialists Conference*, pp. 2586–2592, IEEE, 2007.

[37] Y. Zhang, Z. Zhao, T. Lu, L. Yuan, W. Xu, and J. Zhu, "A comparative study of luenberger observer, sliding mode observer and extended kalman filter for sensorless vector control of induction motor drives," in *Energy Conversion Congress and Exposition*, pp. 2466–2473, IEEE, 2009.

[38] D. Luenberger, "An introduction to observers," *IEEE Transactions on Automatic Control*, vol. 16, no. 6, pp. 596–602, 1971.

[39] W. Wang and Z. Gao, "A comparison study of advanced state observer design techniques," in *American Control Conference*, vol. 6, pp. 4754–4759, IEEE, 2003.

[40] R. E. Kalman and R. S. Bucy, "New results in linear filtering and prediction theory," *Journal of Fluids Engineering*, vol. 83, no. 1, pp. 95–108, 1961.

[41] F. E. Daum, "Nonlinear filters: Beyond the kalman filter," *IEEE Aerospace and Electronic Systems Magazine*, vol. 20, no. 8, pp. 57–69, 2005.

[42] S. Drakunov and V. Utkin, "Sliding mode observers. tutorial," in *Proceedings of the 34th IEEE Conference on Decision and Control*, vol. 4, pp. 3376–3378, IEEE, 1995.

[43] J. Li, L. Xu, and Z. Zhang, "An adaptive sliding-mode observer for induction motor sensorless speed control," *IEEE Transactions on Industry Applications*, vol. 41, no. 4, pp. 1039–1046, 2005.

[44] C. Lascu and G.-D. Andreescu, "Sliding-mode observer and improved integrator with dc-offset compensation for flux estimation in sensorless-controlled induction motors," *IEEE Transactions on Industrial Electronics*, vol. 53, no. 3, pp. 785–794, 2006.

[45] M. Tursini, R. Petrella, and F. Parasiliti, "Adaptive sliding-mode observer for speed-sensorless control of induction motors," *IEEE Transactions on Industry Applications*, vol. 36, no. 5, pp. 1380–1387, 2000.

[46] V. Utkin, J. Guldner, and J. Shi, *Sliding Mode Control in Electro-Mechanical Systems*, vol. 34. CRC press, 2009.

[47] Y. Zhang, Z. Zhao, Y. Zhang, and G. Song, "A full sliding mode sensorless control of three-level inverter-fed induction motors," in *Power Electronics Specialists Conference*, pp. 2825–2831, IEEE, 2008.

[48] X. Chen, W. Shen, Z. Cao, and A. Kapoor, "A comparative study of observer design techniques for state of charge estimation in electric vehicles," in *7th IEEE Conference on Industrial Electronics and Applications (ICIEA)*, pp. 102–107, IEEE, 2012.

[49] P. Li, "State feedback," *University of Minnesota*, pp. 98–136, 2008.

[50] J. Xu, K.-Y. Lum, L. Xie, and A.-P. Loh, "Fault detection and isolation of nonlinear systems: An unknown input observer approach with sum-of-squares techniques," *Journal of Dynamic Systems, Measurement, and Control*, vol. 134, no. 4, pp. 1–7, 2012.

[51] S. Billings, *Nonlinear System Identification: NARMAX methods in the time, frequency, and spatio-temporal domains*. John Wiley and Sons, 2013.

[52] L. A. Zadeh, "A summary and update of fuzzy logic," in *International Conference on Granular Computing (GrC)*, pp. 42–44, IEEE, 2010.

[53] B. Derrida, "Introduction to neural network models," *Nuclear Physics B*, vol. 4, pp. 673–677, 1988.

[54] I. Guyon, "Neural networks and applications tutorial," *Physics Reports*, vol. 207, no. 3, pp. 215–259, 1991.

[55] M. Geetha, J. Jerome, P. A. Kumar, and K. Anadhan, "Comparative performance analysis of extended kalman filter and neural observer for state estimation of continuous stirred tank reactor," in *Fourth International Conference on Computing, Communications and Networking Technologies*, pp. 1–7, IEEE, 2013.

[56] P. Swerling, "Modern state estimation methods from the viewpoint of the method of least squares," *IEEE Transactions on Automatic Control*, vol. 16, no. 6, pp. 707–719, 1971.

[57] I. J. Myung, "Tutorial on maximum likelihood estimation," *Journal of mathematical Psychology*, vol. 47, no. 1, pp. 90–100, 2003.

[58] N. J. Gordon, D. J. Salmond, and A. F. Smith, "Novel approach to nonlinear/non-gaussian bayesian state estimation," *IEEE Proceedings on Radar and Signal Processing*, vol. 140, no. 2, pp. 107–113, 1993.

[59] R. Ortega, "An on-line least-squares parameter estimator with finite convergence time," *Proceedings of the IEEE*, vol. 76, no. 7, pp. 847–848, 1988.

[60] A. E. Frazho and P. J. Sherman, "On the convergence of the minimum variance spectral estimator in nonstationary noise," in *International Conference on Acoustics, Speech, and Signal Processing*, pp. 3141–3143, IEEE, 1991.

[61] E.-W. Bai, M. Fu, R. Tempo, and Y. Ye, "Convergence results of the analytic center estimator," *IEEE Transactions on Automatic Control*, vol. 45, no. 3, pp. 569–572, 2000.

[62] E. Kamen, "A recursive parameter estimator yielding exponential convergence under sufficient excitation," *Systems and Signal Processing Circuits*, vol. 8, no. 2, pp. 207–228, 1989.

[63] C. R. Johnson, *Lectures on Adaptive Parameter Estimation*. Prentice-Hall, Inc., 1988.

[64] R. R. Bitmead and B. Anderson, "Lyapunov techniques for the exponential stability of linear difference equations with random coefficients," *IEEE Transactions on Automatic Control*, vol. 25, no. 4, pp. 782–787, 1980.

[65] Y. Song and J. W. Grizzle, "The extended kalman filter as a local asymptotic observer for nonlinear discrete-time systems," in *American Control Conference, 1992*, pp. 3365–3369, IEEE, 1992.

[66] M. Boutayeb, H. Rafaralahy, and M. Darouach, "Convergence analysis of the extended kalman filter used as an observer for nonlinear deterministic discrete-time systems," *IEEE Transactions on Automatic Control*, vol. 42, no. 4, pp. 581–586, 1997.

[67] S. Julier and J. Uhlmann, "Signal processing, sensor fusion, and target recognition vi," *AeroSense '97*, vol. 3068, 1997.

[68] H. Zhang, G. Dai, J. Sun, and Y. Zhao, "Unscented kalman filter and its nonlinear application for tracking a moving target," *Optik-International Journal for Light and Electron Optics*, vol. 124, no. 20, pp. 4468–4471, 2013.

[69] J. L. Crassidis and F. L. Markley, "Unscented filtering for spacecraft attitude estimation," *Journal of guidance, control, and dynamics*, vol. 26, no. 4, pp. 536–542, 2003.

[70] A. Charles, M. Nandhini, and A. Sakthivel, "A comparative study of sliding mode observers," *International Journal on Recent and Innovation Trends in Computing and Communication*, vol. 3, no. 5, pp. 2923–2929, 2015.

[71] H. K. Khalil and L. Praly, "High-gain observers in nonlinear feedback control," in *International Journal of Robust and Nonlinear Control*, vol. 24, pp. 993–1015, 2014.

[72] T. Braun, F. Strausberger, and J. Reuter, "State estimation for fast-switching solenoid valves: A study on practical nonlinear observers and new experimental results," in *20th International Conference on Methods and Models in Automation and Robotics (MMAR)*, pp. 862–867, IEEE, 2015.

[73] K. A. Mahapatro, A. D. Chavan, P. V. Suryawanshi, and M. E. Rane, "Comparative analysis of linear and non-linear extended state observer with application to motion control," *International Conference on Convergence of Technology*, pp. 1–7, 2014.

[74] T. Zhou, "On the convergence and stability of a robust state estimator," *IEEE Transactions on Automatic Control*, vol. 55, no. 3, pp. 708–714, 2010.

[75] B. Walcott, M. Corless, and S. Żak, "Comparative study of non-linear state-observation techniques," *International Journal of Control*, vol. 45, no. 6, pp. 2109–2132, 1987.

[76] A. Ţiclea and G. Besançon, "Immersion-based observer design," in *Nonlinear Observers and Applications*, pp. 115–138, Springer, 2007.

[77] F. Liu, V. Anh, and I. Turner, "Numerical solution of the space fractional fokker–planck equation," *Journal of Computational and Applied Mathematics*, vol. 166, no. 1, pp. 209–219, 2004.

[78] F. E. Daum, "New exact nonlinear filters: Theory and applications," in *SPIE's International Symposium on Optical Engineering and Photonics in Aerospace Sensing*, pp. 636–649, International Society for Optics and Photonics, 1994.

[79] G. Bastin and M. R. Gevers, "Stable adaptive observers for nonlinear time-varying systems," *IEEE Transactions on Automatic Control*, vol. 33, no. 7, pp. 650–658, 1988.

[80] R. Marino, "Adaptive observers for single output nonlinear systems," *IEEE Transactions on Automatic Control*, vol. 35, no. 9, pp. 1054–1058, 1990.

[81] R. Marino and P. Tomei, "Global adaptive observers for nonlinear systems via filtered transformations," *IEEE Transactions on Automatic Control*, vol. 37, no. 8, pp. 1239–1245, 1992.

[82] R. Marino and P. Tomei, *Nonlinear Control Design: Geometric, adaptive and robust*. Prentice Hall International (UK) Ltd., 1996.

[83] R. Samanta and G. Das, "A comparative study between luenberger full order observer and full order observer designed by generalized matrix inverse method," in *First International Conference on Automation, Control, Energy and Systems (ACES)*, pp. 1–5, IEEE, 2014.

[84] G. Besançon, "An overview on observer tools for nonlinear systems," in *Nonlinear Observers and Applications*, pp. 1–33, Springer, 2007.

[85] J. Zarei and E. Shokri, "Robust sensor fault detection based on nonlinear unknown input observer," *Measurement*, vol. 48, pp. 355–367, 2014.

[86] Y. Yang and P. Xuan, "Design of a nonlinear adaptive observer for a class of lipschitz systems," in *33rd Chinese Control Conference (CCC)*, pp. 2240–2243, IEEE, 2014.

[87] M. Shahrokhi and M. Morari, "A discrete adaptive observer and identifier with arbitrarily fast rate of convergence," *IEEE Transactions on Automatic Control*, vol. 27, no. 2, pp. 506–509, 1982.

[88] K. Khayati and J. Zhu, "Adaptive observer for a large class of nonlinear systems with exponential convergence of parameter estimation," in *International Conference on Control, Decision and Information Technologies (CoDIT)*, pp. 100–105, IEEE, 2013.

[89] N. Boizot and E. Busvelle, "Adaptive-gain observers and applications," in *Nonlinear Observers and Applications*, pp. 71–114, Springer, 2007.

[90] R. Rajamani, "Observers for lipschitz nonlinear systems," *IEEE Transactions on Automatic Control*, vol. 43, no. 3, pp. 397–401, 1998.

[91] W. Byrski and J. Byrski, "On-line fast identification method and exact state observer for adaptive control of continuous system," in *11th World Congress on Intelligent Control and Automation (WCICA)*, pp. 4491–4497, IEEE, 2014.

[92] J. DeCruyenaere and H. Hafez, "A comparison between kalman filters and recurrent neural networks," *IJCNN International Joint Conference on Neural Networks*, vol. 4, pp. 247–251, 1992.

[93] M. Mosavi, "Comparing dgps corrections prediction using neural network, fuzzy neural network, and kalman filter," *GPS Solutions*, vol. 10, 2006.

[94] D. C. Psichogios and L. H. Ungar, "A hybrid neural network-first principles approach to process modeling," *AIChE J.*, vol. 38, pp. 1499–1511, 1992.

[95] C. Hu, B. Youn, and J. Chung, "A multiscale framework with extended kalman filter for lithium-ion bettery soc and capacity estimation," *Applied Energy*, vol. 92, pp. 694–704, 2012.

CHAPTER 3. STUDY OF INPUT SPACE FOR STATE ESTIMATION OF HIGH-RATE DYNAMICS

J. Hong, S. Laflamme, and J. Dodson

Abstract

High-rate dynamic systems are defined as systems being exposed to highly dynamic environments that comprise high-rate and high-amplitude events. Examples of such systems include civil structures exposed to blast, space shuttles prone to debris strikes, and aerial vehicles experiencing in-flight changes. The high-rate dynamic characteristics of these systems provides several possibilities for state estimators to improve performance, including a high potential to reduce injuries and save lives. In this paper, opportunities and challenges that are specific to state estimation of high-rate dynamic systems are presented and discussed. It is argued that a possible path to design of state estimators for high-rate dynamics is the utilization of adaptive data-based observers, but that further research needs to be conducted to increase their convergence rate. An adaptive neuro-observer is designed to examine the particular challenges in selecting an appropriate input space in high-rate state estimation. It is found that the choice of inputs has a significant influence on the observer performance for high-rate dynamics when compared against a low-rate environment. Additionally, misrepresentation of a system dynamics through incorrect input spaces produces large errors in the estimation which could potentially trick the decision making process in a closed loop system in making bad judgments.

3.1 Introduction

High-rate dynamic systems are systems being exposed to highly dynamic environments which comprise of high-rate and high-amplitude events. When exposed to these highly dynamic events, a system can undergo rapid changes. Examples of such systems include hypersonic vehicles and impact protection systems. The ability of an estimator to sense, analyze, and predict the state or health of high-rate dynamic systems could be invaluable to mitigate intolerable costs of human life or economic loss resulting from unintended failure [1]. If the system is capable of identifying and adapting to the change in a timely manner, control decisions, such as active mitigation strategies, can be undertaken to prevent further damage and complete failure [2].

Advances in estimation and control theory, along with computer sciences, enables the development of observers with rapid convergence for estimation. Such observers have the potential to produce smarter, safer, and more effective systems capable of responding to real-time events. While conventional estimators are not robust to noise and uncertainty, algorithms have been developed to handle such complexities although not without penalties [3]. In the presence of noise, a Kalman Filter (KF)-type observer can be used to obtain accurate estimates, but with added computational costs. Likewise, methods have been developed to overcome heavy computation such as the Uniform Robust Exact Observers (UREO) [4], objective functions formulated from modal data [5] and self-tuning fusion Kalman filters [6]. Through these efforts, it is undeniable that modern research in state estimation has been geared towards producing faster and more efficient observers for systems with various levels of complexity.

With the growing number of applications needing estimators on high-rate dynamic systems, the research area of state estimation will soon require algorithms that can robustly estimate the states of high-rate dynamic systems. The objective of this paper is to illustrate the importance of addressing the high-rate dynamics-specific challenges, with a particular attention on the importance that the input space of an observer may play in high-rate dynamics state estimation.

Important challenges in high-rate dynamic systems will be introduced. A path to high-rate state estimation is discussed, which leverages adaptive observers (AO) as a promising solution for

complex nonstationary systems. The influence of the input space on a high-rate state estimator will be studied, and it will be shown that its proper design can substantially enhance the performance of AO. This investigation will be conducted through simulations of a neuro-observer on high-rate laboratory experimental data.

3.2 Applications for State Estimation of High-Rate Dynamics

As scientists and engineers are continually developing faster and more powerful mechanical and civil systems, the concerns for safety is also growing. High-rate systems operate at speeds faster than human reflexes. Thus, in order to operate safely, they require the incorporation of smarter systems capable of making decisions that will protect the lives of the operators and/or surrounding personnel, as well as the financial investments in these high-rate systems. This section discusses engineering systems for which state estimation of high-rate dynamics can be particularly useful. Examples include civil structures exposed to blast, space shuttle debris prone to debris strikes, and aerial vehicle experiencing in-flight changes. They are organized into two categories: 1) impact detection and mitigation; and 2) in-flight monitoring and rapid guidance adaptability.

3.2.1 Impact Detection and Mitigation

Designing structures to withstand blast is a growing area of research due to the increased number of terrorist attacks. Military installations are not the only targets as seen in the historical bombings on civilian buildings such as the World Trade Center in 1993 and the Alfred P. Murrah Federal Building in 1995. Sources of blast loads for civil structures are not limited to terrorist attacks, but also include accidental explosions caused by gas leaks, vehicular accidents, and chemicals mishaps. Blast creates a shock wave of energy that often exceeds the yield strength of the structural material, causing damage and jeopardizing structural integrity, and may result in partial or total collapses. Blast mitigation is typically conducted by passive strategies, including friction elements, laminated windows, hardened concrete, and more [7, 8, 9]. Semi-active and active control methods are also being investigated.

An example of an active blast mitigation method can be found in [10]. The authors proposed a pre-compressed cellular material that deploys before the blast wave arrival. The blast is detected by electromagnetic emission sensors milliseconds before arrival. The compressed material is then deployed by high-speed actuators. The compressibility of the material absorbs the shock waves and the deployment of the material causes momentum cancellation. This active method is preferred over passive methods because it allows blast mitigation using far less materials. While simulations showed promise, it was acknowledged that the release of the cellular material just prior to the arrival of the blast impulse would significantly improve the performance of the proposed procedure. The engineering of such reactive system would require the development of state estimators of high-rate dynamics. Specifically, the arrival time of a blast produced by a 10 kg TNT varies from approximately 0.3 ms at a 1 m range to approximately 100 ms at a 40 m range. It follows that the reactive system would necessitate sensing, estimation, and actuation below this 0.3 - 100 ms range.

Another example of technology for impact detection and mitigation is airbag systems. According to the United States Census Bureau, in 2009 10.8 million motor vehicle accidents occurred of which 30,797 where fatal [11]. Not all accidents lead to serious injuries, but of the ones that do, airbags have played an important role in saving many lives [12]. The airbag control unit uses a combination of sensors such as accelerometers, impact sensors, wheel tachometers, and brake pressure sensors to make a quick decision on whether to deploy the airbags or not. The sensor signals enter an amplifier and are filtered before reaching the airbag control unit. Typical modern systems use threshold levels for each sensor. If the threshold is met for multiple sensors, the airbags trigger. However, at times, airbag systems are known to cause unnecessary or even fatal injuries [13].

Improving the airbag system is ongoing research. For instance, research in [14] on stereovision-based sensing methods uses stereo cameras combined with an intelligent algorithm to determine the occupant classification (small child or unsafe position) before the deployment of airbags. To accommodate for the large distortions in the data, a thin plate spline algorithm is used to calculate a smooth function and interpolate a surface. The child detection is conducted at the moment the vehicle is started to save on computation time. On the other hand, the unsafe position has

to be identified during the impact while determining whether to disable or trigger the airbags in time. This system boasts a processing time of 960 ms. Another area that is being researched is in adaptive airbag deployment. This technology focuses on deployment force, deployment geometry, and stiffness of the airbag using multi stage inflators and venting systems [15]. Fatal accidents occur at a very fast rate, forcing the human body to collide with the interior of the vehicle in a fraction of a second [16]. Like systems which may experience impact conditions could benefit from state estimators capable of estimating high-rate dynamics. In the case of airbag systems, estimation of the high-rate dynamics or impact location of a human-being could result in rapid mitigation decisions to minimize or eliminate damage and losses by appropriate airbag deployment.

3.2.2 In-Flight Monitoring and Rapid Guidance Adaptability

Debris strike during a space shuttle launch can be catastrophic. The loss of Columbia in 2003, killing all crew members, arose from the impact of foam insulation to the leading edge of the left wing during the shuttle launch that caused a breach in the thermal protection system. The foam insulation separated 81.7 s into the flight at an altitude of 66,000 ft and traveling at a velocity of 705 m/s [17]. During re-entry, heat pierced the leading-edge insulation, which degraded the structure of the left wing. This resulted in a weakening of the structure causing loss of control and eventually destruction of the Orbiter [18]. If the damage had been detected the instant it occurred, the launch could have been aborted, avoiding the catastrophic failure. Since then, NASA has developed and uses a NASA debris radar system to target and track debris during ascent. The NASA debris system automatically detects and characterizes debris. It is capable of assigning a ballistic number to assess the material type, size, release location, and threat associated with the object [19]. While this system is very sophisticated, it uses an offsite ground radar system. Ground intervention is not always possible due to communication delays or visibility issues, and knowledge of failures is required onboard for operational capabilities [20]. Because of the rate at which space shuttles travel during launch and re-entry, even soft materials such as insulating foam behave differently and can pierce through metal panels which may be very difficult to comprehend.

Nonetheless, these phenomenons are real and estimators to observe systems under high-rate events are necessary.

More generally, during a flight, aircrafts can experience system failures or damage arising from the failure of components or from an impact with a foreign object such as a bird strike, hail impact, and lightning strike. Such events can cause larger issues if it leads to uncertainty in the navigational decision-making capabilities. In the event of an in-flight failure or damage, rapid estimations using uncertain data are required to regain and maintain control of the aircraft. The faster the estimator, the less the error it needs to compensate for. There has been significant research towards Fault Detection, Isolation and Recovery (FDIR) and prognostics health management sub-systems [21]. The traditional approach to providing fault estimation for aircraft has been to duplicate the hardware such as sensors, actuators, and flight control computers. An alternative to this redundancy is to use a model-based fault detection and diagnosis and generate redundant estimates of measured signals. To achieve robustness in the model-based methods, different techniques have been studied to include optimization methods, unknown input observers, sliding mode observers, and geometric design approaches [22].

Additionally, aerospace technology is moving toward the development of hypersonic passenger and military airframes, which will most likely face similar challenges of foreign object impacts. A typical Boeing passenger aircraft can operate at about 600 mph or equivalently about Mach 0.8. By definition, hypersonic refers to speeds of Mach 5 or greater [23]. High-rate estimators would have the benefit of increasing reaction time to anomalies by allowing faster decisions, decreasing risks associated with system failure. For example, Mach 5 at an altitude 10000 m and -50 °C corresponds to an approximate speed of 1500 m/s. If sampling at 1 Hz, there would be 1500 m travel distance between data points. Alternatively, to obtain a 1 mm resolution while traveling, a sampling rate of 1.5 MHz would be necessary. At such a rate, for each sample an observer requires to converge, the vehicle travels 1 mm. And after the convergence of the observer, there will be time delays for decision making computation and actuator reaction times. Using the input space of a system, we

can reduce the number of data points required for convergence and increase the decision speed for monitoring and controlling the high-rate system.

3.3 Challenges Associated with State Estimation of High-Rate Dynamics

Estimating the dynamics states of complex structures with high-rate dynamics is a non-trivial task. By definition, high-rate dynamic systems require rapid state estimation to optimize guidance and save lives. Moreover, fast estimators should not be confused with state estimation of "fast" dynamics. For example, state observers for induction motors capable of convergence in the microsecond range have been reported in literature using an adaptive sliding observer and an Extended Kalman Filter (EKF) with computation times of 19 μs and 86 μs, respectively for one update using a 250 MHz processor [24], and using a LO, Sliding Mode Observer (SMO), and EKF with computation times of μs, 5 μs, and 100 μs, respectively for one update using a 150 MHz processor [25]. While this demonstrates that microsecond state estimation is possible and currently exists for some applications, the induction motor itself is not a high-rate dynamic system but instead a "fast" dynamic system. There are three key factors that differentiate high-rate dynamic systems from fast dynamic systems. High-rate dynamic systems may have:

- Large uncertainties on the external loads. High-rate events will occur at an undetermined time with an uncertain amplitude. For example, a man-made blast cannot be predicted in time and its amplitude largely depends on the explosive used and the detonation distance.
- High levels of nonstationarity and heavy disturbance. A high-rate load may provoke large changes in the system's states, and could also significantly alter the system's dynamic parameters. For example, an unmanned aerial vehicle could lose a wing following a debris strike.
- Generations of unmodeled dynamics (noise) from change in mechanical configuration. The exposure to highly dynamic environments can cause significant changes, which can appear as noise in measurements. For example, noise may arise from cable movement, flexing of

the electronics, and threaded interfaces, which may rattle from loss of torque under high amplitude dynamics.

These factors seen in the form of system complexities (e.g., uncertain systems, noisy systems, etc.), have been considered in many research, and solutions to specific complexities have been proposed [5, 6, 26, 27, 28, 29, 30]. Nevertheless, research is yet to address situations when all of these factors are combined, also known as the high-rate dynamics problem. A brief survey on observers is conducted in the next subsections to develop building blocks for a potential solution. The survey is intended to provide the reader with a general background, and should be used to understand the possible impact that the choice of an observer may have on systems experiencing high-rate dynamics. It is divided between fixed and AOs.

3.3.1 Fixed Observers and High-Rate Dynamic Systems

The LO [31] is a classic observer used for linear systems with well-defined numerical models. The LO has proven itself to be valuable in the areas of system monitoring and regulations, detecting, and identifying failures in dynamic systems [32]. However, since they are heavily dependent on the mathematical model of the system, disturbances, dynamic uncertainties, and nonlinearities can be particularly challenging. The KF [33] can be used in linear applications where noise is present and characterized as Gaussian [24]. While the KF typically produces estimations with higher accuracy than the LO, its implementation is more complex [25] due to possibly unmodeled nonlinearities in the system model and ill-conditioning of the covariance matrix [34]. The SMO [35] can be an alternative to provide enhanced robustness [36, 37, 38, 39, 40], but it is sensitive to the choice of gain [41]. It also exhibits ripples in the presence of external noise [25].

Variations of these typical fixed observers have been developed to broaden their applicability to more complex systems. For instance, EKF uses a linear approximation of the nonlinear system [44] by either taking the derivative of the nonlinear function or applying a Taylor series expansion to the desired order of the approximation. A challenge with the EKF is the linearization of the system making the corresponding propagation equations available only to the neighborhood of the

Table 3.1: Summary of typical fixed observers in terms of general applicability to the problem of state estimation of high-rate dynamics.

Observer Type	Performance Summary	Applicable to High-Rate Dynamic Systems?	Ref.
Luenberger Observer (LO)	Very fast convergence rates for linear systems with precise system models	Not applicable, high-rate dynamic systems are nonlinear and uncertain	[32]
Sliding Mode Observer (SMO)	High robustness and improved results for inaccurate models, but sensitive to choice of gain limiting the convergence rate	Not suitable for high-rate dynamic systems	[36, 37, 38, 39, 40, 41]
Extended Kalman Filter (EKF)	High accuracy for nonlinear systems with added noise, but complex implementation leading to poor convergence rates	Poses challenges for real-time and high-rate applications.	[34, 25]
High-Gain Observer (HGO)	Accurate and fast convergence rates for estimating slowly varying states or inputs	Not suitable for high-rate systems	[42, 27]
Robust State Estimator (RSE)	Guarantees robustness for time invariant systems, constant filter design parameters, and stationary external inputs	Only applicable to stationary high-rate dynamic systems	[43]

estimate [45]. It requires longer time for convergence compared with the LO and SMO [25]. The EKF is also difficult to apply to nonlinear systems with time-varying parameters, particularly in the presence of noise [26]. Reference [46] introduces the Utkin and Walcottzak variations of the SMO observers. While robust, both of these variations struggle in the estimation of states when some inputs are unavailable. The high gain observer (HGO) uses a sufficiently high observer gain that will guarantee good performance of the observer in terms of accuracy and speed of convergence [42]. For most cases, the HGO is used as an LO-type estimator with large gain and the application is for estimating slowly varying states or inputs [27]. A disadvantage of the HGO is strong chattering when the gain is very large [47]. Lastly, the robust state estimator (RSE) guarantees robustness of the designed estimator if time invariant nominal system matrices, constant filter design parameters, and stationary external inputs conditions are met. However, the computational complexity is comparable with that of the KFs [43]. Table 3.1 summarizes the observers discussed in this section in terms potential weaknesses for high-rate systems.

3.3.2 Adaptive Observers and High-Rate Dynamic Systems

AOs are often modifications of the fixed observers discussed previously. For example, adaptive versions of the HGO and the EKF have been studied in [48]. The high gain aspect of the HGO serves to eliminate the nonlinear part of the system while allowing rapid convergence, thus making it a good candidate for nonlinear systems. The EKF is useful to filter out system or process noise, therefore advantageous for field applications. The two observers were combined to create a high-gain extended Kalman filter (HG-EKF), which possesses the advantages of both estimators. The authors showed that the resulting HG-EKF could converge at a desired speed with the tuning of only one parameter, while also being capable of noise rejection. Although promising, a key issue with the HG-EKF is with the exponential convergence occurring only at the beginning of the estimation process from the initial condition. Large perturbations in the system are difficult to estimate if they are not already modeled within the system. This issue was overcome with the development of the adaptive gain extended Kalman filter (AG-EKF). The main advantages of this observer are the noise rejection and the ability to estimate perturbations. The trade-off is that the convergence rate of the AG-EKF is not as good as the HGO or HG-EKF due to the algorithm's complexity.

A coupled technique of system identification and state estimation has been proposed before. Plett in [49] proposed a joint EKF method, where a weight EKF estimates the system parameters and a state EKF estimates the system states. Hu et. al. in [50] proposed an update to the joint EKF method to provide multiscale estimation. The two EFKs run concurrently to maintain accurate estimates of the state of charge (SOC) and capacity of lithium-ion (Li-ion) batteries, which degrade with age. In the multiscale case, a macro time-scale is used to adapt the slowly varying parameters, while a micro time-scale is used to adapt the fast varying states. By using a multiscale framework, the estimation process is accelerated. Nevertheless, from the high-rate view point, the Li-ion battery is a slow time-varying system with smaller uncertainties. It is argued that the minimal representation by use of input space will indeed decrease computational times.

3.3.3 A Path to State Estimation of High-Rate Dynamics

Further developments and extensions of state-of-the-art fixed and adaptive observers need to be conducted in order to broaden the applicability of observers to the problem of state estimation of high-rate dynamic systems. While many paths could be undertaken to achieve that goal, the authors are noting the particular promise of adaptive data-based observers. AOs have been proposed to estimate the unmeasurable states for different classes of nonlinear systems [51]. They are typically characterized by asymptotic stability [52], but are known to have slower convergence rates. In related studies, reference [52] attributed this problem to the utilization of single observation errors, while reference [51] explained this slow convergence by the complexity of the adaptive law. AOs can be used to estimate states and parameters using input-output measurements, ideal for handling uncertainty in state estimation [53]. Methods include fuzzy logic [54] and neural network (NN) estimators [55]. The performance of data-based method is linked to the quality of data mining and interpretation algorithms, and an additional limitation can be found in the computational time required to achieve an appropriate estimate [56].

The adaptable characteristics of a state estimator is deemed critical for high-rate dynamic systems given the high levels of uncertainties, nonstationarity, disturbance, and noise that they can undergo. Data-based solutions can also be particularly helpful at providing important flexibility by enabling state estimation without the reliance on a model, in particular for highly uncertain and nonstationary systems. For dynamic parameters undergoing large variations, a hybrid form between data- and model-based solutions could be used to accelerate convergence. For instance, a data-based technique would be used as a system identifier fed into a model-based technique. It follows that, while the authors selected an adaptive data-based approach as a possible path to the high-rate state estimation challenge, other viable techniques exist. Examples include dual methods of system identification and state estimation using KFs for time-varying systems [50], modal-based methods including numerical algorithms for subspace state space system identification [57] and eigensystem realization algorithm [58], and statistical methods including particle filters [59] and unscented Kalman filters [60].

The data-based adaptive state estimators are in essence black-box models that could be pre-trained or adapted sequentially. In the high-rate dynamics problem, pre-training could be difficult for a certain set of systems given the uncertainty on external loads. Sequential adaptation is also challenging, because the system is required to learn and perform on-the-spot. Algorithms capable of sequential adaptation and immediate performance have been studied in the field of structural control for mitigation of unknown excitations in uncertain systems [61, 62]. However, sequential adaptation will typically yield larger initial errors and a slower convergence rate, and it follows that such observer needs to be designed appropriately.

The sequential adaptive learning problem can be simplified as the construction of a function characterizing an input-output system. This problem has been researched and addressed in many fields through various machine learning methods. When looking at high-rate dynamic systems as input-output systems, a key feature that distinguishes them is the vast quantity of input data. Even in the case of a single sensor, the very large sampling rate will result in the accumulation of a vast time series vector. It results that one needs to decide which part of this time series would be fed as input, or how many delayed observations will constitute the inputs such as:

$$\begin{aligned} \hat{y}_k &= f(y_i(t), y_i(t-\tau), y_i(t-2\tau), \cdots, y_i(t-(d-1)\tau)) \\ &= f(\nu(\tau, d)) \end{aligned} \tag{3.1}$$

where $\hat{y}_k$ is the estimated state, y_i is an observation i, τ is a time delay, and d is the dimension of the input space ν, with ν termed the delay vector [63]. These parameters must be selected carefully in order to guarantee a certain level of performance. The procedure to select an input space in data-based techniques is often overlooked. The selection of input may influence computation time, adaptation speed, effects of the curse of dimensionality, understanding of the representation, and model complexity [64, 65, 66, 67]. Available selection techniques include the filter methods, where the input selection is independent of the black-box model [68], the wrapper methods, where the results from the black-box model are used to rank and select the inputs [69], and the embedding methods, where selected inputs are used for adapting the representation [70]. Automatic input

selection methods have been discussed [71, 72, 67, 73, 74], but they are traditionally applied offline and necessitates pre-training. In the case of high-rate dynamic systems, as it will be demonstrated in the next section, the selection of the input space is critical to the observer's performance, and the optimal input space varies as a function of events.

3.4 Study of System Input Space

We demonstrate the importance of the input space selection for high-rate dynamic systems by designing a neuro-observer and evaluating its performance as a function of different inputs. The design of the neuro-observer is presented in detail below. The subsequent subsection presents and discuses results from the simulation of the state estimation of a system experiencing high-rate dynamics. Note that the design of the neuro-observer was kept simple in order to focus the discussion on the importance of the input space selection. One could certainly design an adaptive observer that would provide, overall, better performance.

3.4.1 Neuro-observer Architecture

The neuro-observer is a single-layer wavelet neural network written

$$\hat{y}_k = \sum_{j=1}^{h} \gamma_j \phi_j(\boldsymbol{\nu}) \tag{3.2}$$

where h represents the number of nodes, γ the nodal weights of node j, and ϕ is the activation function taken as a Mexican hat wavelet

$$\phi(\boldsymbol{\nu}) = \left(1 - \frac{\|\boldsymbol{\nu} - \boldsymbol{\mu}\|_2}{\boldsymbol{\sigma}^2}\right) e^{-\frac{\|\boldsymbol{\nu}-\boldsymbol{\mu}\|_2}{\boldsymbol{\sigma}^2}} \tag{3.3}$$

where $\boldsymbol{\mu}$ and $\boldsymbol{\sigma}$ are the wavelet centers and bandwidths, respectively, and $\|\cdot\|_2$ is the 2-norm. The neuro-observer is designed to be capable of sequential adaptive learning, whereas no prior training is necessary. To do so, a self-organizing mapping architecture is adopted to minimize the network size [75]. This self-organization is conducted by adding a node if a new observation falls outside an Euclidean distance threshold D to the closest node. When a new node j is added, it is given a

weight γ_j initially equal to zero, a center $\boldsymbol{\mu}_j$ at the location of the new observation, and bandwidth $\boldsymbol{\sigma}_j$ of the newly added wavelet initially set at 10000. The network is then put in an adaptation mode, where weights and bandwidths are adapted following a back-propagation rule. With the back-propagation rule, an adaptive parameter ζ is varied using

$$\dot{\zeta} = \Gamma_\zeta \frac{\partial(\boldsymbol{\gamma}^T \boldsymbol{\phi})}{\partial \zeta} \tilde{y} \tag{3.4}$$

where $\tilde{y}$ is the observation error between the estimated and the measured state and Γ_ζ is the learning rate associated with the adaptive parameter ζ. The stability of the adaptation rule has been derived in [62]. In a discrete notation, Eq. (3.4) can be specialized for $\boldsymbol{\mu}_j$ and $\boldsymbol{\sigma}_j$ at node j:

$$\begin{aligned}
\gamma_j(k+1) &= \gamma_j(k) - \Gamma_{\gamma_j} \phi_j(\boldsymbol{\nu}) \tilde{y} \\
\sigma_j(k+1) &= \sigma_j(k) - \Gamma_{\sigma_j} \gamma_j \left(\frac{1}{\sigma_j^5} \mathrm{e}^{\frac{-\|\boldsymbol{\nu}-\mu_j\|^2}{\sigma_j^2}} (4\sigma_j^2 \|\boldsymbol{\nu}-\mu_j\|^2 - 2\|\boldsymbol{\nu}-\mu_j\|^4) \right) \tilde{y}
\end{aligned} \tag{3.5}$$

where k is a discrete time step.

3.4.2 Simulations

Simulations of the estimation using the neuro-observer were conducted on experimental data collected from an impact test series conducted on an electronic components package to demonstrate the importance of proper input space selection. The experimental setup is illustrated in Fig. 3.1. On the right is the electronics system of interest. The systems contains four circuit boards, each of the four boards have a surface mounted high-g shock accelerometer (Meggitt 72). These accelerometers are capable of accurately measuring acceleration upwards of 120,000 g_n or 120 kg_n [76]. The circuit boards are housed in a metal canister and filled with an electronics potting material. The system is secured in a metal fixture, shown in the middle of the figure, using a lock ring. On the left is the MTS-66 drop tower designed to generate a prescribed impact condition. Bungee cords are used to accelerate the table of the drop tower. The fixture housing the system is mounted on the drop tower table using bolts. The picture shows the table in the raised state. When the table brakes

are released, the table along with the system accelerates downward and impacts the black mass at the bottom of the drop tower creating a mechanical shock. In this section, the acceleration data is presented in terms of g_n ($1\ g_n = 9.81\ \text{m/s}^2 = 32.2\ \text{ft/s}^2$).

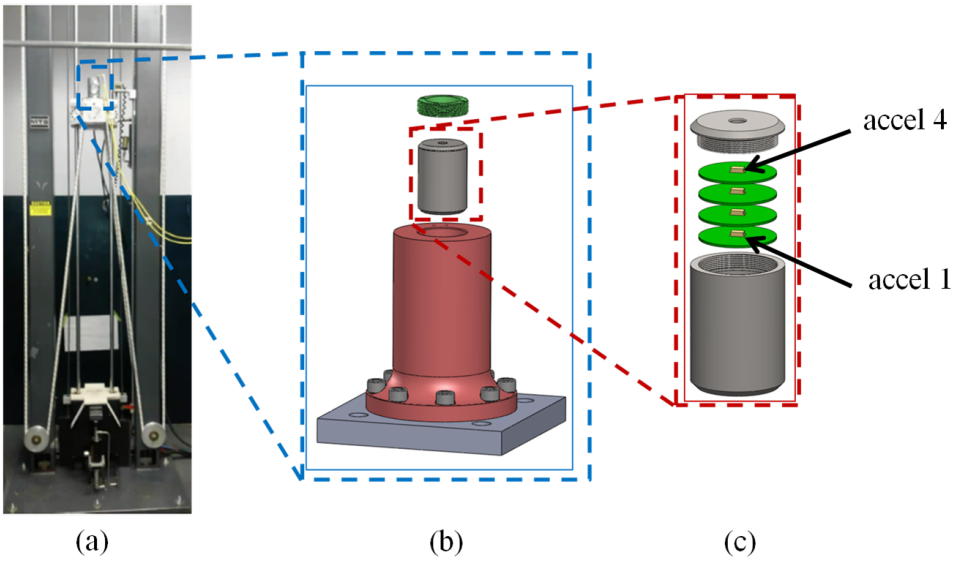

Figure 3.1: Experimental setup: (a) MTS-66 drop tower, (b) unit fixture, (c) electronics unit.

This problem contains many complexities making model-based techniques difficult to apply. The accelerometers are hardwired to the data acquisition system. When the table accelerates, so does the sensor cables, creating a violent whipping motion. Even though careful selection of cables was made, some noise is added from whipping of the cables. Additionally, whenever metal parts are coupled together in impact scenarios, such as in this case, noise is produced from the chattering of the parts. Uncertainties associated with this problem include unknown material high-rate response of the circuit boards and potting material, uncertainties in the exact placement of the accelerometers and circuit board spacing, and boundary conditions such as whether or not the potting material moves in relation to the housing. The exact input to the system resulting from the table impact is unknown. Only the measurement from the response of the accelerometers can be taken as certain. Note that such tests are considered as small impact tests within the shock dynamics community, and not enough energy was present to excite the sensor resonance. However,

it is not uncommon in larger impact tests to notice disturbances created from sensor and/or system resonance.

The studied system bears many characteristics of a high-rate system. The way data is used in the simulation greatly simplifies the problem significantly by attempting to identify a representation estimating accel 4 using accel 1, where the inputs and outputs are the systems are known. Typical field applications would either have the outputs be unknown, for instance the estimation of velocity for acceleration data, or use the inputs to conduct system identification, for instance the identification of a stiffness value. Such realistic applications require the integration of additional steps and mathematics in the algorithm, which would drive the attention away from our discussion on the opportunities and limitations in the input space.

The impact is controlled by specifying a drop height and mitigating material. Event 1 is created with a drop height of 20 in and 1/16 in thickness felt. The raw data was collected using a National Instruments PXI-6133 High-Speed cards with a sampling rate of 1 MHz coupled with a Precision Filters signal conditioning system 28144A quad-channel wideband transducer conditioner with an anti-aliasing filter of 204.6 kHz. Figure 3.2 shows three back-to-back tests of event 1 that exhibit gradual increases in the response pointing to time varying parameters possibly from the weakening of the glue that holds the accelerometers on to the circuit boards and/or from the electronics potting material de-bonding from the internal walls of the unit's metal canister. This confirms the high-rate dynamic nature of our system.

Figure 3.3 shows the experimental data from accelerometers 1 (accel 1) and 4 (accel 4) of test 2, which the simulations of the estimation using the neuro-observer are conducted on. These accelerometers are selected because of the notable difference between the two responses. The impact occurs over 0.1 ms starting at about 0.2 ms, which in turn excites the system that responds over the next 0.6 ms. In the course of the dynamic event, an acceleration level greater than 60 kg_n is observed.

In the simulations, accel 1 was used as the input and accel 4 was used as the output. The input was used to estimate the output using the neuro-observer. For the investigation, a lower rate event

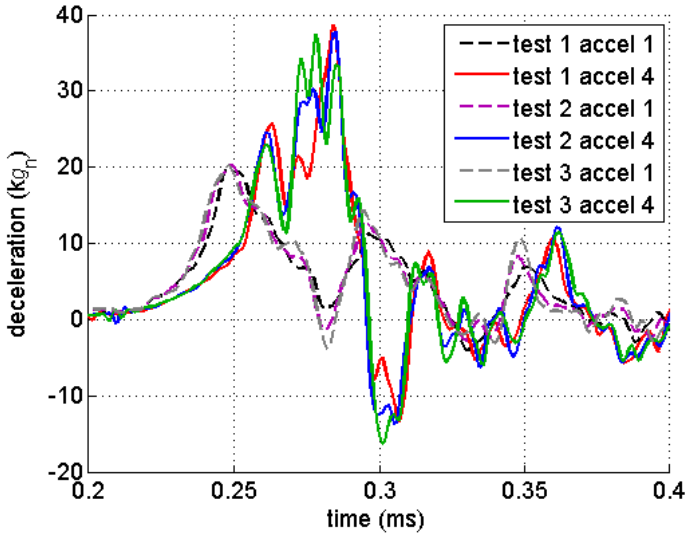

Figure 3.2: Response of three subsequent tests.

was synthetically created by filtering the experiment data at 5 kHz using a 4-pole Butterworth low pass filter, with the purpose to demonstrate the added importance of the input space for high-rate systems. From here on, high-rate data will refer to the raw data and low-rate data will refer to the filtered data. Both time series are plotted in Fig. 3.4.

Two different metrics were used to quantify the performance of the input space. The first performance metric J_1 of the estimator is taken as

$$J_1 = \frac{\|(\hat{\boldsymbol{y}} - \ddot{\boldsymbol{x}}_{\boldsymbol{4}})\|_2}{\|\ddot{\boldsymbol{x}}_{\boldsymbol{4}}\|_2} \tag{3.6}$$

with $\hat{\boldsymbol{y}} = \hat{\ddot{\boldsymbol{x}}}_{\boldsymbol{4}}$ being the estimation of the measurement of accel 4, $\ddot{\boldsymbol{x}}_{\boldsymbol{4}}$. The $\|\cdot\|_2$ represents the 2-norm. By representing the error of the estimate as described in equation 3.6, the error is normalized to fall within the values of [0,1]. Additionally, normalizing the error helps to compare the errors between various simulations.

The second performance metric J_2 of the estimator is in terms of the convergence rate. The convergence rate is defined as the time it takes from the start of the impact (>100 g_n) to when the estimation error falls and remains within an error threshold. The error threshold was determined to be 5% and is governed by the variations in the data created by the experimental setup. Because the

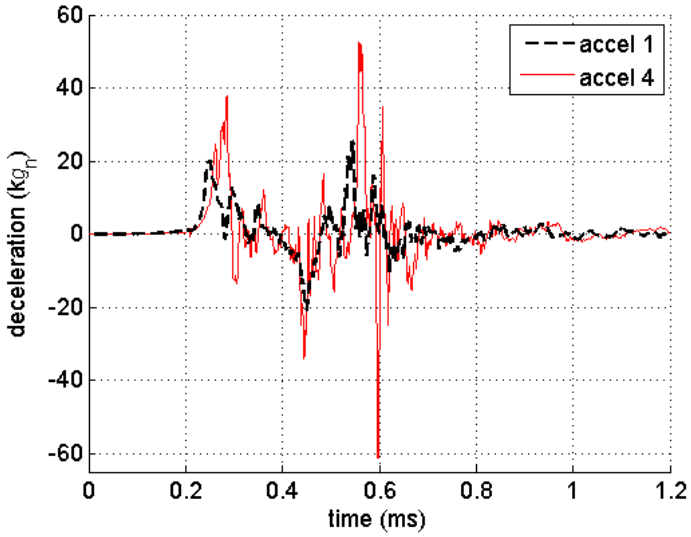

Figure 3.3: Experimental data from the accelerometer measurements.

objective of the paper is to demonstrate the importance of the input space and not the optimality of the observer solution, the computational time is used as a performance metric. For the same reason, a study on the influence of internal parameter tuning is not conducted. Here, the internal parameters Γ_σ, Γ_γ, and the initial γ and σ were tuned based on a prior study from the authors presented in [77].

A parametric study of the input space in terms of the embedding dimension and time delay was conducted on both the high- and low-rate data. The parametric study was conducted by running the estimator over a grid of possible input space $d = [2{:}1{:}10]$ and $\tau = [1{:}1{:}400]$ to find the optimal values for d and τ (Eq. (5.8) that minimized J_1). We find $d = 3$ and $\tau = 46$ for the high-rate data, and $d = 2$ and $\tau = 150$ for the low-rate data. The fitting errors using these values are plotted in Fig. 3.5. It can be noted that the optimal dimension d decreases with a smoother function (e.g., low-rate data), and that the smoother function leads to a significantly lower estimation error, yielding $J_1 = 0.238$ for the high-rate data, and $J_1 = 0.106$ for the low-rate data. Also, the estimator for the filtered data converges 0.105 ms faster. The lower performance of the estimator on the raw data is explained by the larger and higher nonlinearities in the estimated dynamics.

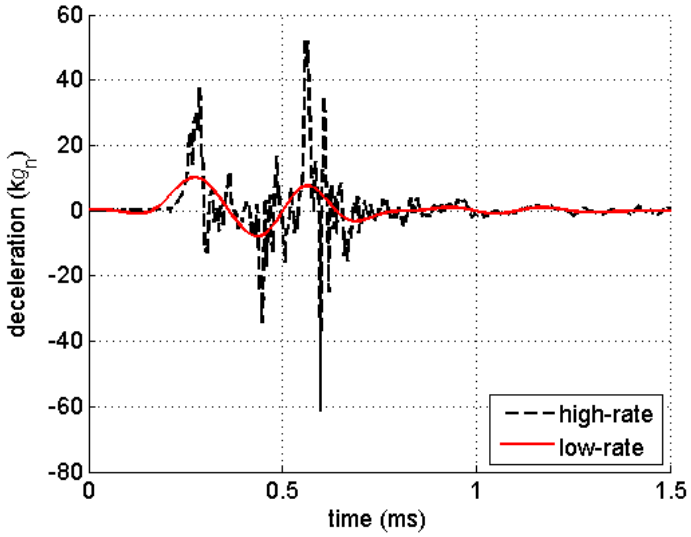

Figure 3.4: High and low rate data the simulations were conducted on.

The influence of the input space on the performance of the estimator is further studied by investigating different combinations of d and τ. The combinations and associated performance J_1 and J_2 are listed in Table 3.2, in which the change in performance, or percent difference in J_1 and J_2 relative to the optimal performance is indicated in columns 6 and 8 respectively. Note that a dimension $d = 2$ is considered as the lowest possible dimension, and therefore the under embedding is not shown for the low-rate data.

Table 3.2: Estimator performance associated with different input spaces.

data	combination	d	τ	J_1	% diff J_1	J_2 (ms)	% diff J_2
high-rate	optimal	3	46	0.238	–	0.484	–
high-rate	under embedding	2	46	0.310	30.3	0.542	12.0
high-rate	over embedding	4	46	0.454	90.8	0.876	81.0
high-rate	incorrect information	3	150	0.441	85.3	0.681	40.7
low-rate	optimal	2	150	0.106	–	0.379	–
low-rate	over embedding	3	150	0.143	34.9	0.748	97.4
low-rate	incorrect information	2	46	0.141	33.0	0.446	17.7

Results from Table 3.2 shows that utilizing the wrong input space for the high-rate dynamics results in larger decreases in performance J_1 when compared to the utilization of the wrong input

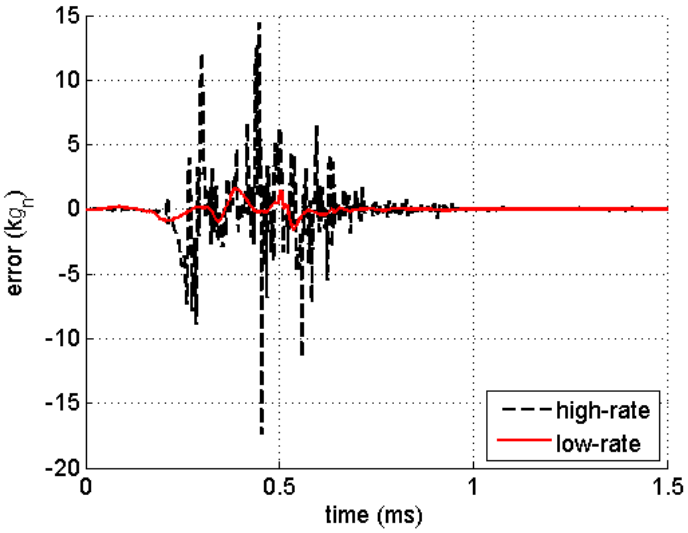

Figure 3.5: Comparison between estimation errors of high- and low-rate data.

space for the low-rate dynamics. This is similar for the J_2 performance metric, except for the effect of over embedding, which is important for both the high- and low-rate systems, yet larger for the low-rate system. For the high-rate dynamics, under embedding yields to a better performance when compared to over embedding. This can be explained by a faster convergence provided by a lower input space dimension, because a function of lower dimension can be populated faster with sequential training examples. Using the wrong τ has dramatic effects on the performance of the high-rate estimator. Fig. 3.6 is a plot of the absolute estimation errors of the high-rate dynamics under different input spaces. The absolute estimation error is used to portray the errors associated with incorrect input spaces to make the plots more readable. An input space of incorrect time delay ($d = 3$, $\tau = 150$) yields a significantly higher error peaks compared to other strategies. Under embedding ($d = 2$, $\tau = 46$) produces a large error peak at about 0.6 ms, same as for the incorrect time delay but around 50% lower in magnitude. Over embedding ($d = 4$, $\tau = 46$) also results in high peaks, yet of relatively smaller magnitude. The error peak at 0.6 ms is about equal to the under embedding error and the other peak occurs after the convergence with the other strategies. The presence of these abnormal high error peaks can lead to false alarms and incorrect decisions in the closed-loop process.

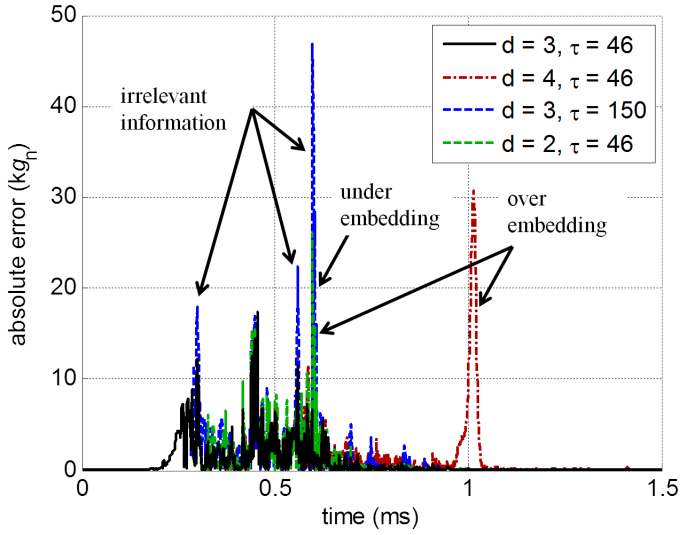

Figure 3.6: Absolute estimation errors for different input strategies for high-rate dynamics.

Figure 3.7 shows how the convergence rate is affected by the choice of different d and τ. The results show that different input spaces within the provided range can yield a difference in convergence rate over 1 ms, which is very large for high-rate dynamics. Note that a convergence rate beyond 1.5 ms means that the estimator never converged and the simulation was stopped, because the high amplitude dynamic response is approximately 1 ms. The optimal convergence rate is given by the choice $d = 3$ and $\tau = 27$ yielding a convergence rate of 0.467 ms (a 3.5% increase in performance), which differs from the input space providing the best 2-norm error (J_1) and yields $J_1 = 0.316$ (a 32.8% decrease in performance). The choice of lower dimensions d generally yields a more constant convergence rate for varying τ.

Table 3.3: Optimal d and τ for events 1 and 2.

dynamic event	combination	d	τ	J_1	% diff J_1	J_2 (ms)	% diff J_2
event 1	optimal	3	46	0.238	–	0.484	–
event 1	incorrect	4	54	0.435	82.8	1.027	112.2
event 2	optimal	4	54	0.196	–	0.490	–
event 2	incorrect	3	46	0.256	30.6	0.637	30.0

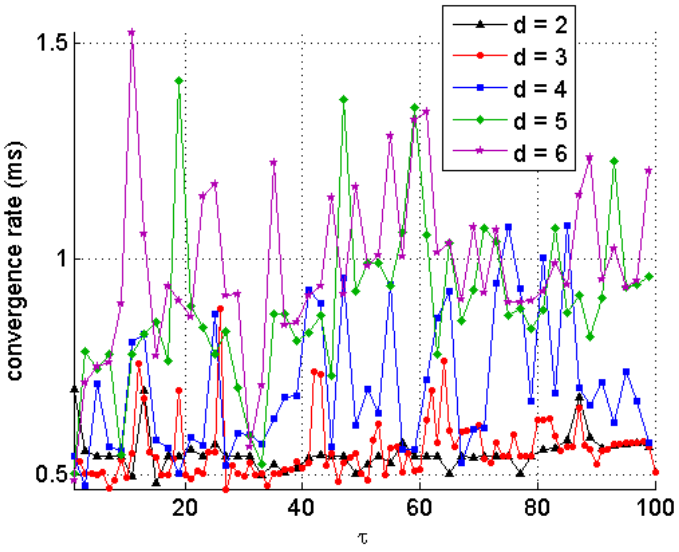

Figure 3.7: Convergence rates as a function of embedding dimensions and time delays for high-rate dynamics.

Simulations of the estimation using the neuro-observer were also conducted on experimental data from a second impact event. The second impact event was created with a drop height of 72 in and 1/2 in thickness felt, instead of a drop height of 20 in and 1/16 in thickness felt for the first impact. In reality, different environmental conditions could occur even from a slight change in impact location or angle, for example, that can produce very different results by exciting different modes with different phases. The optimal input space was determine for both events, independently. Figure 3.8 shows the different dynamic events.

The optimal d and τ for event 1 and 2 are listed in table 3.3.

The performance attained using optimal input space, optimized for the J_1 metric, for events 1 and 2 were compared. Results are listed in Table 3.3. Using the optimal input space of event 1 for event 2, there is a 30% decrease in performance for both J_1 and J_2. A significantly worst result is observed seen when using the optimal input for event 2 for event 1. These results show that while an static input space could be designed based on an event, it might be very ineffective when used for state estimation of the same system subjected to a different event.

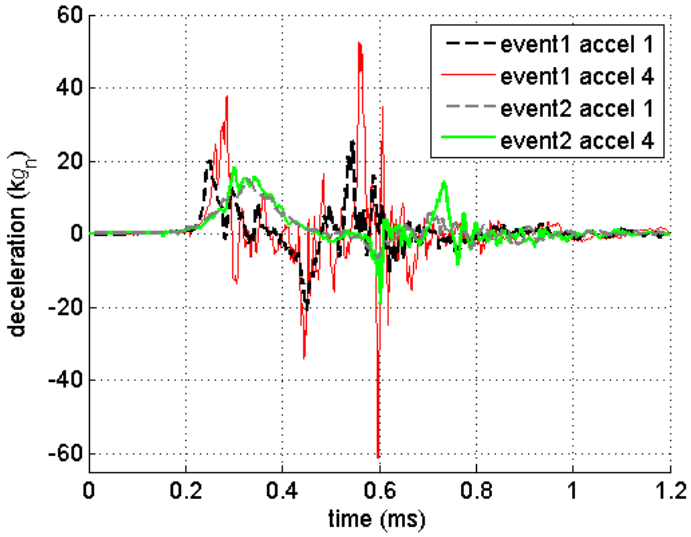

Figure 3.8: Dynamic event 1 and 2.

3.5 Conclusion

State estimation of high-rate dynamics is a challenging task, in particular for complex engineering systems experiencing highly dynamic events and requiring real-time observability to ensure adequate performance. Application of the estimators on the high-rate systems include hypersonic vehicles and impact protection systems. High-rate system state estimation-specific challenges were listed, and the applicability of typical observers at achieving that specialized task discussed. A path to state estimation of high-rate dynamics was presented. It was argued that data-based adaptive observers (AOs) could be particularly promising, because of their ability to process information without knowledge of system dynamics or the high-rate event, and their high adaptability to complex dynamics. However, the utilization of AOs comes with the cost of slower convergence rates, a critical obstacle to the state estimation of high-rate dynamics problem.

A potential solution to improving the convergence rate of AOs is through the careful design of the input space of the estimator. The influence of the input space on a high-rate state estimator was investigated. An adaptive neuro-observer was constructed and simulations were performed on

high-rate laboratory experimental data. The estimator's performance was based on the normalized 2-norm errors and convergence rates. Simulation results highlighted a few key observations:

- The use of a proper input space is critical to enhancing the performance of high-rate dynamics state estimators. The use of incorrect input space for estimation has significant negative impacts, which are much larger for high-rate data than low-rate data.
- The misrepresentation of the system dynamics through wrong input spaces produces abnormally large error peaks, which can lead to poor decisions in the closed-loop process.
- The input space is not unique to a system, but rather to a dynamic environment. Different input spaces are required for different events for optimal estimator performance.

From the simulation results, the importance of input space in evident in making the most accurate and fast estimations. The challenge is choosing the right input space for the right situation. Often, the type of high-rate dynamic event a system will experience before the event occurs is unknown, and pre-selecting the input space is a very challenging task. A solution, part of future work, is to develop algorithms automating the input space selection process as a function of different events, yielding adaptive input spaces.

3.6 References

[1] R. Lowe, J. Dodson, and J. Foley, "Microsecond prognostics and health management," *IEEE Reliability Society Newsletter*, vol. 60, pp. 1–5, 2014.

[2] J. Connor and S. Laflamme, *Structural Motion Engineering*. Springer International, 2014.

[3] S. Mondal, G. Chakraborty, and K. Bhattacharyya, "Robust unknown input observer for nonlinear systems and its application to fault detection and isolation," *Journal of Dynamic Systems, Measurement, and Control*, vol. 130, no. 4, pp. 1–5, 2008.

[4] L. Fraguela, M. T. Angulo, J. Moreno, and L. Fridman, "Design of a prescribed convergence time uniform robust exact observer in the presence of measurement noise," *IEEE 51st Annual Conference on Decision and Control*, pp. 6615–6620, 2012.

[5] S. S. Kourehli, A. Bagheri, G. G. Amiri, and M. Ghafory-Ashtiany, "Structural damage detection using incomplete modal data and incomplete static response," *KSCE Journal of Civil Engineering*, vol. 17, no. 1, pp. 216–223, 2013.

[6] G.-L. Tao and Z.-l. Deng, "Convergence of self-tuning riccati equation for systems with unknown parameters and noise variances," in *8th World Congress on Intelligent Control and Automation (WCICA)*, pp. 5732–5736, IEEE, 2010.

[7] L. H. Lin, E. Hinman, H. F. Stone, and A. M. Roberts, "Survey of window retrofit solutions for blast mitigation," *Journal of Performance of Constructed Facilities*, vol. 18, no. 2, pp. 86–94, 2004.

[8] Y. Zhengqiang, L. Aiqun, and X. Youlin, "Fluid viscous damper technology and its engineering application for structural vibration energy dissipation," *Journal of Southeast University (Natural Science Edition)*, vol. 32, no. 3, pp. 466–473, 2002.

[9] E. Hinman, "Blast safety of the building envelope," *Whole Building Design Guide, National Institute of Building Sciences*, 2005.

[10] H. N. Wadley, K. P. Dharmasena, M. He, R. M. McMeeking, A. G. Evans, T. Bui-Thanh, and R. Radovitzky, "An active concept for limiting injuries caused by air blasts," *International Journal of Impact Engineering*, vol. 37, no. 3, pp. 317–323, 2010.

[11] "Transportation." https://www.census.gov, 2012.

[12] B. Meier, "Study shows air bags save lives, but says seat belts are needed, too," *The New York Times*, 1992.

[13] K. Cunningham, T. Brown, E. Gradwell, and P. Nee, "Airbag associated fatal head injury: Case report and review of the literature on airbag injuries," *Journal of Accident & Emergency Medicine*, vol. 17, no. 2, pp. 139–142, 2000.

[14] S.-J. Lee, M.-S. Jang, Y.-G. Kim, and G.-T. Park, "Stereovision-based real-time occupant classification system for advanced airbag systems," *International Journal of Automotive Technology*, vol. 12, no. 3, pp. 425–432, 2011.

[15] "Trw introduces adaptive airbags." http://safety.trw.com, 2011.

[16] R. Din, "Injuries of the foot and ankle joint and their mechanisms," *Societatea Inginerilor de Automobile*, 2004.

[17] J. D. Walker, "From columbia to discovery: Understanding the impact threat to the space shuttle," *International Journal of Impact Engineering*, vol. 36, no. 2, pp. 303–317, 2009.

[18] D. Smith, "Megalightning and the demise of sts-107 space shuttle columbia: A fresh look at the available evidence." http://www.columbiadisaster.info, 2009.

[19] B. M. Kent, "Return-to-flight electromagnetic measurementsthe nasa shuttle ascent debris radar system," in *8th European Conference on Antennas and Propagation*, pp. 1–3, IEEE, 2014.

[20] R. Fonod, C. Charbonnel, and E. Bomschlegl, "A class of nonlinear unknown input observer for fault diagnosis: Application to fault tolerant control of an autonomous spacecraft," in *UKACC International Conference on Control*, pp. 13–18, IEEE, 2014.

[21] Y. Zhang and J. Jiang, "Bibliographical review on reconfigurable fault-tolerant control systems," *Annual Reviews in Control*, vol. 32, no. 2, pp. 229–252, 2008.

[22] X. Sun, R. J. Patton, and P. Goupil, "Robust adaptive fault estimation for a commercial aircraft oscillatory fault scenario," in *International Conference on Control*, pp. 595–600, IEEE, 2012.

[23] "Hyersonic." http://www.merriam-webster.com, 2016.

[24] Z. Xu, F. Rahman, and D. Xu, "Comparative study of an adaptive sliding observer and an ekf for speed sensor-less dtc ipm synchronous motor drives," in *Power Electronics Specialists Conference*, pp. 2586–2592, IEEE, 2007.

[25] Y. Zhang, Z. Zhao, T. Lu, L. Yuan, W. Xu, and J. Zhu, "A comparative study of luenberger observer, sliding mode observer and extended kalman filter for sensorless vector control of induction motor drives," in *Energy Conversion Congress and Exposition*, pp. 2466–2473, IEEE, 2009.

[26] R. M. F. Oliveira, E. Ferreira, F. Oliveira, and S. Azevedo, "A study on the convergence of observer-based kinetics estimators in stirred tank bioreactors," *Korean Institute of Chemical Engineers*, vol. 6, no. 6, pp. 367–371, 1994.

[27] K. Stricker, L. Kocher, D. Van Alstine, and G. M. Shaver, "Input observer convergence and robustness: Application to compression ratio estimation," *Control Engineering Practice*, vol. 21, no. 4, pp. 565–582, 2013.

[28] K. Yamada and M. Kobayashi, "A design method for unknown input observer for non-minimum phase systems," in *International Workshop and Conference on Photonics and Nanotechnology*, pp. 1–6, International Society for Optics and Photonics, 2007.

[29] Y. Wang, R. Rajamani, and D. M. Bevly, "Observer design for differentiable lipschitz nonlinear systems with time-varying parameters," in *53rd Annual Conference on Decision and Control (CDC)*, pp. 145–152, IEEE, 2014.

[30] B. K. Kim, W. K. Chung, and K. Ohba, "Design and performance tuning of sliding-mode controller for high-speed and high-accuracy positioning systems in disturbance observer framework," *IEEE Transactions on Industrial Electronics*, vol. 56, no. 10, pp. 3798–3809, 2009.

[31] D. Luenberger, "An introduction to observers," *IEEE Transactions on Automatic Control*, vol. 16, no. 6, pp. 596–602, 1971.

[32] W. Wang and Z. Gao, "A comparison study of advanced state observer design techniques," in *American Control Conference*, vol. 6, pp. 4754–4759, IEEE, 2003.

[33] R. E. Kalman and R. S. Bucy, "New results in linear filtering and prediction theory," *Journal of Fluids Engineering*, vol. 83, no. 1, pp. 95–108, 1961.

[34] F. E. Daum, "Nonlinear filters: Beyond the kalman filter," *IEEE Aerospace and Electronic Systems Magazine*, vol. 20, no. 8, pp. 57–69, 2005.

[35] S. Drakunov and V. Utkin, "Sliding mode observers. tutorial," in *Proceedings of the 34th IEEE Conference on Decision and Control*, vol. 4, pp. 3376–3378, IEEE, 1995.

[36] J. Li, L. Xu, and Z. Zhang, "An adaptive sliding-mode observer for induction motor sensorless speed control," *IEEE Transactions on Industry Applications*, vol. 41, no. 4, pp. 1039–1046, 2005.

[37] C. Lascu and G.-D. Andreescu, "Sliding-mode observer and improved integrator with dc-offset compensation for flux estimation in sensorless-controlled induction motors," *IEEE Transactions on Industrial Electronics*, vol. 53, no. 3, pp. 785–794, 2006.

[38] M. Tursini, R. Petrella, and F. Parasiliti, "Adaptive sliding-mode observer for speed-sensorless control of induction motors," *IEEE Transactions on Industry Applications*, vol. 36, no. 5, pp. 1380–1387, 2000.

[39] V. Utkin, J. Guldner, and J. Shi, *Sliding Mode Control in Electro-Mechanical Systems*, vol. 34. CRC press, 2009.

[40] Y. Zhang, Z. Zhao, Y. Zhang, and G. Song, "A full sliding mode sensorless control of three-level inverter-fed induction motors," in *Power Electronics Specialists Conference*, pp. 2825–2831, IEEE, 2008.

[41] X. Chen, W. Shen, Z. Cao, and A. Kapoor, "A comparative study of observer design techniques for state of charge estimation in electric vehicles," in *7th IEEE Conference on Industrial Electronics and Applications (ICIEA)*, pp. 102–107, IEEE, 2012.

[42] H. K. Khalil and L. Praly, "High-gain observers in nonlinear feedback control," in *International Journal of Robust and Nonlinear Control*, vol. 24, pp. 993–1015, 2014.

[43] T. Zhou, "On the convergence and stability of a robust state estimator," *IEEE Transactions on Automatic Control*, vol. 55, no. 3, pp. 708–714, 2010.

[44] Y. Song and J. W. Grizzle, "The extended kalman filter as a local asymptotic observer for nonlinear discrete-time systems," in *American Control Conference, 1992*, pp. 3365–3369, IEEE, 1992.

[45] M. Boutayeb, H. Rafaralahy, and M. Darouach, "Convergence analysis of the extended kalman filter used as an observer for nonlinear deterministic discrete-time systems," *IEEE Transactions on Automatic Control*, vol. 42, no. 4, pp. 581–586, 1997.

[46] A. Charles, M. Nandhini, and A. Sakthivel, "A comparative study of sliding mode observers," *International Journal on Recent and Innovation Trends in Computing and Communication*, vol. 3, no. 5, pp. 2923–2929, 2015.

[47] T. Braun, F. Strausberger, and J. Reuter, "State estimation for fast-switching solenoid valves: A study on practical nonlinear observers and new experimental results," in *20th International Conference on Methods and Models in Automation and Robotics (MMAR)*, pp. 862–867, IEEE, 2015.

[48] N. Boizot and E. Busvelle, "Adaptive-gain observers and applications," in *Nonlinear Observers and Applications*, pp. 71–114, Springer, 2007.

[49] G. Plett, "Extended kalman filtering for battery management system of lipb-based hev battery packs - part 3. state and parameter estimation," *J Power Sources*, vol. 134, no. n2, pp. 277–292, 2004.

[50] C. Hu, B. Youn, and J. Chung, "A multiscale framework with extended kalman filter for lithium-ion bettery soc and capacity estimation," *Applied Energy*, vol. 92, pp. 694–704, 2012.

[51] K. Khayati and J. Zhu, "Adaptive observer for a large class of nonlinear systems with exponential convergence of parameter estimation," in *International Conference on Control, Decision and Information Technologies (CoDIT)*, pp. 100–105, IEEE, 2013.

[52] M. Shahrokhi and M. Morari, "A discrete adaptive observer and identifier with arbitrarily fast rate of convergence," *IEEE Transactions on Automatic Control*, vol. 27, no. 2, pp. 506–509, 1982.

[53] Y. Yang and P. Xuan, "Design of a nonlinear adaptive observer for a class of lipschitz systems," in *33rd Chinese Control Conference (CCC)*, pp. 2240–2243, IEEE, 2014.

[54] L. A. Zadeh, "A summary and update of fuzzy logic," in *International Conference on Granular Computing (GrC)*, pp. 42–44, IEEE, 2010.

[55] B. Derrida, "Introduction to neural network models," *Nuclear Physics B*, vol. 4, pp. 673–677, 1988.

[56] I. Guyon, "Neural networks and applications tutorial," *Physics Reports*, vol. 207, no. 3, pp. 215–259, 1991.

[57] P. Van Overschee and M. Bart De, "N4sid: Subspace algorithms for the identification of combined deterministic-stochastic systems," *Automatica*, vol. 30, no. 1, pp. 75–93, 1994.

[58] J. Juang and R. Pappa, "An eigensystem realization algorithm for modal parameter identification and model reduction," *Journal of Guidance, Control, and Dynamics*, vol. 8, no. 5, pp. 620–627, 1985.

[59] S. Arulampalam, S. Maskell, N. Gordon, and T. Clapp, "A tutorial on particle filters for on-line non-linear/non-gaussian bayesian tracking," *IEEE Transactions on Signal Processing*, vol. 50, no. 2, pp. 174–188, 2002.

[60] E. Chatzi and A. Smyth, "The unscented kalman filter and particle filter methods for nonlinear structural system identification with non-collocated heterogeneous sensing," *Structural Control and Health Monitoring*, vol. 16, pp. 99–123, 2009.

[61] S. Laflamme, J.-J. E. Slotine, and J. J. Connor, "Wavelet network for semi-active control," *Journal of Engineering Mechanics*, vol. 137, no. 7, pp. 462–474, 2011.

[62] S. Laflamme, J. E. Slotine, and J. Connor, "Self-organizing input space for control of structures," *Smart Materials and Structures*, vol. 21, no. 11, p. 115015, 2012.

[63] J. Hong, S. Laflamme, and J. Dodson, "Variable input observer for structural health monitoring of high-rate systems," *Quantitative Nondestructive Evaluation*, vol. 43, p. 070003, 2016.

[64] R. Sindelar and R. Babuska, "Input selection for nonlinear regression models," *Fuzzy Systems, IEEE Transactions on*, vol. 12, no. 5, pp. 688–696, 2004.

[65] G. Bowden, G. Dandy, and H. Maier, "Input determination for neural network models in water resources applications. Part 1–background and methodology," *Journal of Hydrology*, vol. 301, no. 1-4, pp. 75–92, 2005.

[66] X. Hong, R. Mitchell, S. Chen, C. Harris, K. Li, and G. Irwin, "Model selection approaches for non-linear system identification: a review," *International journal of systems science*, vol. 39, no. 10, pp. 925–946, 2008.

[67] A. da Silva, A. P., F. V., and R. Velasquez, "Input space to neural network based load forecasters," *Int. J. Forecast*, vol. 24, pp. 616–629, 2008.

[68] A. Blum and P. Langley, "Selection of relevant features and examples in machine learning," *Artificial intelligence*, vol. 97, no. 1-2, pp. 245–271, 1997.

[69] R. Kohavi and G. John, "Wrappers for feature subset selection," *Artificial intelligence*, vol. 97, no. 1-2, pp. 273–324, 1997.

[70] I. Guyon and A. Elisseeff, "An introduction to variable and feature selection," *The Journal of Machine Learning Research*, vol. 3, pp. 1157–1182, 2003.

[71] D. Yu, J. Gomm, and D. Williams, "Neural model input selection for a mimo chemical process," *Eng. Appl. Artif. Intell.*, vol. 13, pp. 15–23, 2000.

[72] K. Li and J. Peng, "Neural input selectiona fast model-based approach," *Neurocomputing*, vol. 70, pp. 762–769, 2007.

[73] J. Tikka, "Simultaneous input variable and basis function selection for rbf networks," *Neurocomputing*, vol. 72, pp. 2649–2658, 2009.

[74] N. Kourentzes and S. Crone, "Frequency independent automatic input variable selection for neural networks for forecasting," *The 2010 Int. Joint Conf. on Neural Networks*, pp. 1–8, 2010.

[75] T. Kohonen, "The self-organizing map," *Neurocomputing*, vol. 21, no. 1–3, pp. 1–6, 1998.

[76] A. Beliveau, J. Hong, J. Coker, and N. Glikin, "COTS piezoresistive shock accelerometers performance evaluation," *Shock and Vibration Exchange*, vol. 83, pp. 1–10, 2012.

[77] J. Hong, L. Cao, S. Laflamme, and J. Dodson, "Robust variable input observer for structural health monitoring of systems experiencing harsh extreme environments," *11th International Workshop on Structural Health Monitoring*, vol. 11, pp. 1–8, 2017.

CHAPTER 4. ADAPTIVE WAVELET NEURAL NETWORK FOR TERRESTRIAL LASER SCANNER-BASED CRACK DETECTION

Y. Turkan, J. Hong, S. Laflamme, and N. Puri

Abstract

Objective, accurate, and fast assessment of civil infrastructure conditions is critical to timely assess safety risks. Current practices rely on visual observations and manual interpretation of reports and sketches prepared by inspectors in the field, which are labor intensive, subject to personal judgment and experience, and prone to error. Terrestrial laser scanners (TLS) are promising for automatically identifying structural condition indicators, such as cracks, displacements, and deflected shapes, as they are capable to provide high coverage and accuracy at long ranges. However, there is limited research conducted on employing TLS for condition assessment. TLS is an advanced 3D imaging technology that is used to rapidly measure the 3D coordinates of densely scanned points within a scene. The data gathered by a TLS is provided in the form of 3D point clouds with color and intensity data often associated with each point within the cloud. Major challenges are in storing significant amount of data and extracting appropriate features enabling condition assessment. This paper proposes a novel adaptive wavelet neural network (WNN)-based approach to compress data into a combination of low- and high-resolution surfaces, and automatically detect concrete cracks and other forms of damage. The adaptive WNN is designed to sequentially self-organize and self-adapt in order to construct an optimized representation. The architecture of the WNN is based on a single-layer neural network consisting of Mexican hat wavelet functions. The strategy is to first construct a low-resolution representation of the point cloud, then detect and localize anomalies, and finally construct a high-resolution representation around these anomalies to enhance their characterization. The approach was verified on a cracked concrete specimen. The experimental

results show that the proposed approach was capable of fitting the point cloud, and of detecting and fitting the crack. It also resulted in a 99.64% compression of data. Using the proposed method for crack detection would enable automatic and remote assessment of structural conditions. This would, in turn, result in reducing costs associated with infrastructure management, and improving the overall quality of our infrastructure by enhancing maintenance operations.

4.1 Introduction

Every four years, American Society of Civil Engineers (ASCE) releases a comprehensive assessment of the U.S. infrastructure. The most recent report card that was published in 2017 gave an overall grade of D+ (poor) for the nations infrastructure, C+ (mediocre) for bridges [1, 2]. Catastrophic events are rare, but the federal National Bridge Inventory classified 56,007 bridges out of 614,387 as structurally deficient. In May 2013, the I-5 Skagit bridge, which was a through truss bridge built in 1955, near Seattle, WA collapsed into the river below when an oversized truck scraped several overhead girders of the bridge. The sudden collapse of I-35W Mississippi River bridge during evening rush hour in 2007, killed 13 people and injured 145. In 1990, federal government had rated this bridge as structurally deficient due to the significant corrosion in its bearings. In 2007, approximately 75,000 other US bridges had this rating. These numbers emphasize the urgent need for more frequent and comprehensive bridge inspections to prevent further catastrophic events. However, the budget available for infrastructure is limited. Therefore, there is a need for finding cheaper and faster ways to maintain and operate our infrastructure.

National Bridge Inspection Standards (NBIS) require routine inspections to assess the condition of bridges on the National Highway System. These inspections, conducted using printed checklists, are typically performed by trained inspectors using visual inspection techniques that are heavily subjective [3, 4]. An inspector must correctly identify the type and location of each element being inspected, document its distress, manually record this information in the field, and transcribe it to the bridge evaluation database after arriving back at his/her office. This is a complex and time-consuming set of responsibilities that are prone to error.

To overcome the weaknesses inherent in visual inspection techniques, several studies proposed methodologies implementing new technologies such as terrestrial laser scanning (TLS) [5, 6, 7], ground penetrating radar (GPR) [8, 9, 10], unmanned aerial vehicles (UAVs) [11, 12, 13, 14, 15, 16, 17, 18] and 3D Bridge Information Models (BrIM) [19, 20, 21, 22, 23] to improve the visual inspection process.

TLS technology, an advanced three-dimensional (3D) imaging technology is employed to gather the data used in this study. TLS rapidly measures the 3D coordinates of densely scanned points within a scene. The data gathered by a TLS is provided in the form of 3D point clouds with color and intensity data associated with each point within the cloud. Point cloud data can be analyzed using various computer vision algorithms and methods to detect structural conditions [24], e.g. concrete cracks [25, 26, 27, 28, 29, 30] and spalling [31, 32].

However, there is limited research conducted on employing TLS to detect and classify cracks automatically for infrastructure condition assessment. Previous research in this area mainly focused on manual detection and measurements of cracks, displacements or shape deflections from TLS point clouds [33, 34, 35]. In its raw format, TLS point cloud data contains significant number of data points that is unstructured, densely and non-uniformly distributed [36]. To overcome the difficulties of manual data processing, in machine learning community, substantial effort has been put in automatically reconstructing 3D shapes from point clouds. The most popular reconstruction methods include the utilization of Splines [37] and partial differential equations (PDE) [38], which was seen as an improvement over Splines in terms of numbers of parameters. Neural networks have also been proposed and demonstrated as superior to PDE-based methods in [39] as they provide robust and compact representations of the data. In particular, Radial Basis Functions (RBF) neural networks have been applied to the problem of shape reconstruction [40]. Compared to traditional types of neural networks, they provide a better approximation, convergence speed, optimality in solution and excellent localization [41]. Furthermore, they can be trained faster when modeling nonlinear representations in the function space [42]. Recent work has been published in utilizing sequential RBF networks for reconstructing surfaces from point clouds [36]. A self-organizing mapping (SOM) [43] architecture was used to optimize node placement, and the algorithm provided good accuracy with minimum number of nodes. Laflamme and Connor have developed a sequential adaptive RBF neural network for real-time learning of nonlinear dynamics and returned similar conclusions where the network showed better performance with respect to traditional neural networks [44]. They also designed wavelet neural networks (WNN) for similar applications [45]. WNN

are also capable of universal approximation [46, 47, 48]. This particular neural network has also been demonstrated as capable of learning dynamics on-the-spot, without prior knowledge of the underlying dynamics and architecture of the input space.

This paper proposes a novel adaptive wavelet neural network (WNN)-based approach to construct compact 3D representations and automatically detect features, here concrete cracks, from TLS point clouds for infrastructure condition assessment. The adaptive WNN is designed to self-organize, self-adapt, and sequentially learn a compact reconstruction of the 3D point cloud. The strategy is to first construct a low-resolution representation of the point cloud, then detect and localize anomalies, and finally construct a high-resolution representation around these anomalies to enhance their characterization. In future studies, such strategy could be used to guide the TLS, in real-time, for constructing accurate representation containing features of interest.

The proposed approach was verified on four cylindrical cracked concrete specimens. The method successfully reconstructed the 3D laser scan data points as wavelet functions in a more compact format for all four specimens. Features were extracted from the compact representation to detect the crack location and quantify the accuracy of the reconstructed cracks in terms of Root Mean Square (RMS) error, where the error is defined as the difference between the wavelet representation and the TLS data. This is a significant improvement over previous TLS based crack detection methods as it does not require prior knowledge about the crack or the 3D shape of the object being scanned. It also enables to process 3D point cloud data faster, which is very important, especially when working with large data sets.

4.2 Background

In this section, comprehensive background information is provided on the state of the art in crack detection on concrete structures, TLS technology as well as its implementation in the AEC-FM industry and details of the WNN algorithm used in this study.

4.2.1 Defect Detection in Concrete Structures

Over the past years, several research efforts have been directed towards automatically detecting defects in concrete structures. Majority of the methods that are proposed thus far rely on collecting images of the concrete structures for inspection purposes.

High resolution cameras mounted on Unmanned Aerial Vehicle (UAV) systems have been proposed to collect images for detecting cracks. A critical advantage of UAVs is that they are not bounded by terrain motion constraints and vision range limitations [49]. A Micro Air Vehicle (MAV) mounted with a high-resolution digital camera was used to acquire images for building inspection [50]. In this study, edge detection method was used to detect structural cracks. The edge detection method is based on applying a Gaussian Blur, the result of blurring an image by a Gaussian function, to the original image and subtracting the blurred image from the original image. Similarly, Sankarasrinivasan et al. [51] applied hue, saturation, and value (HSV) thresholding technique to detect structural cracks in images collected using a Multi Rotor UAV (MUAV) system.

Machine learning and image processing methods have been used in [52] to automatically detect, classify and estimate crack parameters. In this study, the authors used Support Vector Machines (SVM) to classify the cracks into transverse, longitudinal, block, and alligator cracking patterns. The crack length and width parameters were calculated using random sample consensus (RANSAC) algorithm. The approach described in [53] exploits the synergy between photogrammetry and image processing techniques to detect cracks in concrete specimens. It uses the strain field obtained from finite element analysis to map critical crack regions, thus constraining the image processing to critical areas of interest. Photogrammetry technique was used to measure crack thickness in [54]. A comprehensive review on computer vision based defect detection and condition assessment of concrete structures can be found in [24].

The development and application of intelligent robotic systems for defect detection in civil infrastructure is advancing rapidly. Several robotic tunnel inspection systems have been developed with the objective of improving safety in hazardous data collection environments and efficiently carrying out tunnel inspection processes [55]. As a part of the ROBO-SPECT project, a tunnel

assessment approach was developed and tested on the Metsovo Motorway tunnel [56, 57]. The approach used a convolutional neural network (CNN) to extract features describing defects from RGB images and a Multi-Layer Perceptron was used to categorize image pixels into defect and non-defect categories. A robotic platform, developed under the ROBO-SPECT project, was used to detect cracks in the Egnatia Motorway tunnel [58, 59]. This platform uses RGB cameras, a laser scanner and an ultrasonic sensor to detect and collect data from regions containing cracks. The crack detection algorithm is based on a CNN.

4.2.1.1 Terrestrial Laser Scanning (TLS) Technology

TLS is an advanced 3D imaging technology that is used to rapidly measure the 3D coordinates of densely scanned points within a scene. The data gathered by a TLS is provided in the form of 3D point clouds with color and intensity data often associated with each point within the cloud. TLS technology enables direct acquisition of 3D coordinates from the surface of a target object or scene that are visible from the laser scanners viewpoint [60, 61, 62]. There are two types of TLS based on the technology they use to acquire range (x, y, z) and intensity data of objects in a scene; namely time-of-flight (TOF) TLS and phase-based TLS. The two technologies differ in calculating the range, while both acquire each range point in the equipments spherical coordinate frame by mounting a laser on a pan-and-tilt unit that provides the spherical angular coordinates of the point. TOF scanners emit a pulse of laser light to the surface of the target object or scene and calculate the distance to the surface by recording the round-trip time of the laser light pulse. Phase based scanners measure phase shift in a continuously emitted and returned sinusoidal wave. Both types of TLS achieve similar point measurement accuracies. They differ in scanning speed and maximum scanning range. Typically, phase-based TLS achieve faster data acquisition (up to one million points per second) and has an accuracy of 0.4 mm at a range of 11 m. TOF-based TLS enables collecting data from longer ranges (up to a kilometer) and has an accuracy of 6 mm at a range of 100 m.

4.2.1.2 TLS implementation in the AEC-FM Industry

TLS technology enables capturing comprehensive and very accurate 3D data for an entire construction scene using only a few scans [63]. Among other 3D sensing technologies, TLS is the best adapted technology for capturing the 3D status of construction projects and condition of infrastructure accurately and efficiently. In a study by [64], it is shown that the 3D laser scanning hardware, software, and services market has grown exponentially in the last decade, and the Architecture, Engineering, Construction and Facilities Management (AEC-FM) industry is one of its major customers. This shows that owners, decision makers and contractors are aware of the potential of using this technology for capturing the 3D as-built status of construction projects and condition of infrastructure. Despite the remarkable accuracy and benefits, current adoption rate of laser scanners in the AEC-FM industry is relatively low, mainly because of the data acquisition and processing time and data storage issues. Laser scanners are capable of producing high-resolution models of construction sites, but at the cost of large file sizes and increased data processing time [65]. Thus, there is a need for advanced algorithms to represent the large data files in a compact form while enabling automated 3D shape detection from the compact representation. This would improve project productivity as well as safety by reducing the amount of time spent on-site. TLS is a promising technology for documenting as-built condition of infrastructure [66, 67, 68, 69, 70, 71, 72], and it has already been utilized by a number of state DOTs for this purpose at the project planning phase. Furthermore, TLS technology has been shown to be effective in identifying structural condition indicators, such as cracks, displacements and deflected shapes [73, 74, 75, 76, 77, 78, 79, 80, 81], as they are able to provide large areas of coverage while being accurate at long ranges. Xu, et al. analyzed 3D point clouds of concrete beams to automatically detect and characterize cracks using image filtering and noise removal functions of MATLAB [82]. Zeibak-Shini, et al. developed an approach to locate structural members damaged by an earthquake by reconstructing semantically rich BIM models of damaged building facades using TLS data [83]. They demonstrated this approach using two case studies, and the results showed that the approach successfully located moderate to

heavy damage cases. A crack assessment method developed in [84] utilized both TLS data and images to accurately measure the width, length and orientation of cracks on concrete surfaces.

4.2.2 Wavelet Neural Network (WNN)

The representation of the 3D object is constructed using a single-layer Wavelet Neural Network (WNN). This particular architecture was selected due to its known universal approximation capability and demonstrated fast convergence, as discussed in the introduction. The network comprises h nodes or activation functions ϕ consisting of Mexican Hat wavelets

$$\phi_i(\boldsymbol{\zeta}) = e^{-\frac{\|\boldsymbol{\zeta}-\boldsymbol{\mu}\|_2}{\sigma^2}} \quad \text{for } i = 1, 2, \dots h \tag{4.1}$$

centered at μ_i, with a bandwidth σ_i, and where $\boldsymbol{\zeta}$ is the input vector. The wavelet network maps the z_j coordinate of point $\boldsymbol{\zeta_j} = [x_j, y_j]$ using the function

$$\hat{z}_j = \sum_{i=1}^{h} \gamma_i \phi_i(\boldsymbol{\zeta}) \tag{4.2}$$

where γ_i are weights, and the hat denotes an estimation. The normalizing factor of the wavelet in (4.1) is intentionally omitted as the weights, γ_i in (4.2) account for them. A representation of the WNN with 2D Mexican hat wavelets is illustrated in Fig. 4.1.

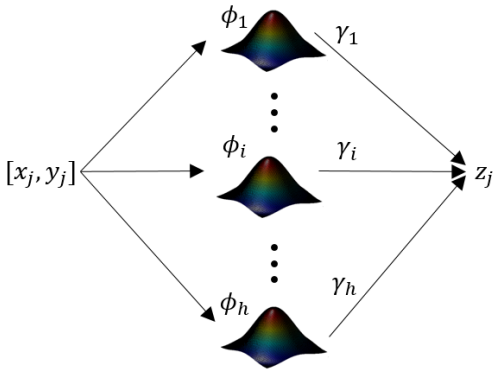

Figure 4.1: Representation of the wavelet neural network architecture.

The network is designed to be self-organizing, self-adaptive, and sequential. The self-organizing feature consists of the capability to add functions at sparse locations. This is done following Kohonens Self-Organizing Mapping (SOM) Theory [43, 85]. The self-adaptive feature consists of adapting the network parameters σ and γ to learn the compact representation. The sequential feature refers to the capability of the network to learn in a sequential manner, as opposed to batch processing. We built this sequential feature for real-time applications in combination with a controllable TLS. Such real-time interaction with a TLS is left to future work.

4.2.2.1 Self-Organization

SOM theory is used to optimize the node placement. A coordinate ζ_j is queried from the scanner, along with its associated z_j. The shortest Euclidean distance is computed between ζ_j and the center of the existing nodes $\boldsymbol{\mu}_i$ for i=1,2,,h. If the shortest distance is greater than a user-defined threshold λ, a new node is added at $\boldsymbol{\mu}_{h+1} = \boldsymbol{\mu}_j = [x_j, y_j]$ with a predefined bandwidth σ_0. The selection of λ defines the resolution of the network, where a small value for λ will yield a larger number of nodes at a higher resolution by larger overlaps of wavelets. Other factors which govern the resolution of the network include the initial bandwidth, σ_0 and the selected learning rates used to adapt the wavelet parameters. The initial weight of the new function is set such that $\gamma_i = z_j$. Remark that the network is initialized with h = 0, and the very first scan will give rise to the first node of the network.

2.2.2 Sequential Self-Adaptability At each scan step k, the WNN error $\tilde{z}_j = \hat{z}_j - z_j$ is computed and parameters $\boldsymbol{\sigma}_i^2$ and γ_i are adapted using the back-propagation method [45]:

$$\dot{\xi} = -\Gamma_\xi \left(\frac{\partial \phi}{\partial \xi} \right) \tilde{z} \tag{4.3}$$

where $\boldsymbol{\xi} = [\boldsymbol{\sigma}^2, \boldsymbol{\gamma}]$, and $\boldsymbol{\Gamma}\xi$ are positive constants representing the learning rates. In discrete notation, the back-propagation rule for $\boldsymbol{\sigma}^2$ and $\boldsymbol{\gamma}$ can be written as below:

$$\sigma_{i,k+1}^2 = \sigma_{i,k}^2 - \Gamma_{\sigma^2}\gamma_{i,k}\left(\frac{||\boldsymbol{\zeta}-\boldsymbol{\mu}||_2}{\boldsymbol{\sigma}_{\boldsymbol{i,k}}^{\boldsymbol{4}}}e^{-\frac{||\boldsymbol{\zeta}-\boldsymbol{\mu}||_2}{\boldsymbol{\sigma}_{\boldsymbol{i,k}}^{\boldsymbol{2}}}}\right)\tilde{z}_j \tag{4.4}$$

$$\gamma_{i,k+1} = \gamma_{i,k} - \Gamma_{\gamma}\left(e^{-\frac{||\boldsymbol{\zeta}-\boldsymbol{\mu}||_2}{\boldsymbol{\sigma}_{i,k+1}^{\boldsymbol{2}}}}\right)\tilde{z}_j \tag{4.5}$$

for i=1,2,,h, where h is the number of nodes at step k and $\boldsymbol{\sigma}_0^2$ and γ_0 are initial values selected by the user. The simulation ends for a user-defined value of k, which could correspond, for example, to the number of points generated by the TLS or more if additional iterations within the point cloud are desired.

4.2.2.2 Reconstruction Strategy

The resolution of the representation of the 3D object impacts memory usage and computational time. A higher resolution representation will require a larger number of wavelets (more memory) and consequently more CPU power for larger vector and matrix operations. For practical real-time usage of a controllable TLS, we propose using a low-resolution fit of the 3D point cloud data for creating a quick and compact representation of an object or structure, run analysis on the low-resolution fit to determine damage areas, then re-run algorithm only on problem areas for a detailed high-resolution examination. The algorithm automatically detects the region of crack based on the low-resolution fit. The 3D point cloud data of the region of crack is used to create a high-resolution fit. A block diagram illustrating our reconstruction strategy is showed in Fig. 4.2. When a damage is detected, two sets of data are recorded: the low-resolution data and the high-resolution data. Such strategy results in shorter computational time and smaller data sets to be preserved.

4.3 Experimental Validation

The developed adaptive WNN algorithm-based approach was validated on four cracked concrete specimens. Specimen 1 was scanned using a Trimble TX5 phase-based TLS, while specimens 2, 3 and 4 were scanned using a NextEngine 3D scanner, based on MultiStripe Laser Triangulation (MLT) technology. Specimens 1, 2, 3 and 4 were scanned on rectangular regions limited to 50

Figure 4.2: Block diagram of reconstruction strategy.

by 65 mm^2, 25 by 40 mm^2, 90 by 20 mm^2, and 60 by 30 mm^2, respectively, to focus the study on the algorithm itself. The specimens are shown in Fig. 4.3(a), 4.4(a), 4.5(a), and 4.6(a), along with a zoom on the limited region (Fig. 4.3(b), 4.4(b), 4.5(b), and 4.6(b)). Fig. 4.3(a) shows the crack that runs through the specimen with a larger damage area (along the first 35.1 mm from the bottom), and a smaller damage geometry along 9.8 mm and after. Fig. 4.4(b) shows specimen 2 with cracks on the left (wide) and the right (narrow), each measuring 25 mm in length from the bottom. Fig. 4.5(b) shows specimen 3 with a long and narrow crack that runs throughout the length of the specimen (90 mm in length). A shallow hairline crack of 60 mm in length was observed in specimen 4, as shown in Fig. 4.6(b).

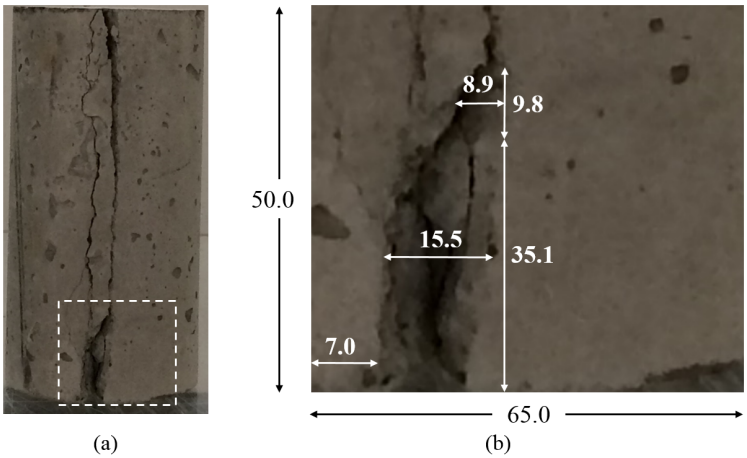

Figure 4.3: (a) Specimen 1 (scanned region shown by the dashed rectangle); and (b) zoom on the scanned region (dimensions in mm).

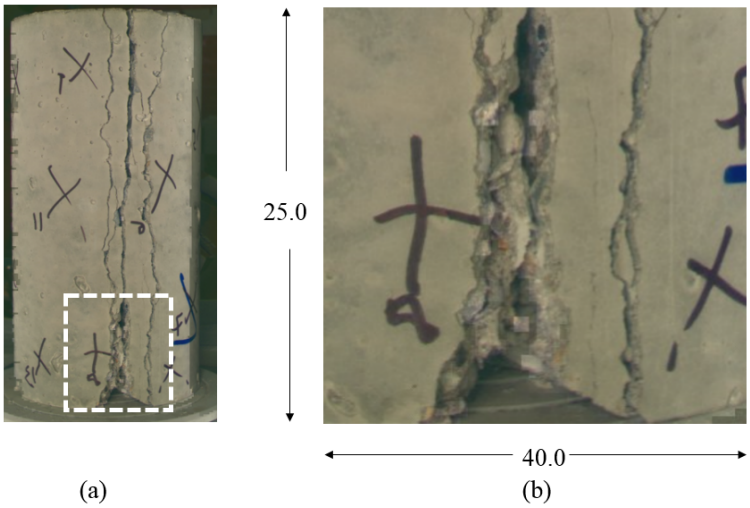

Figure 4.4: (a) Specimen 2 (scanned region shown by the dashed rectangle); and (b) zoom on the scanned region showing two cracks (dimensions in mm).

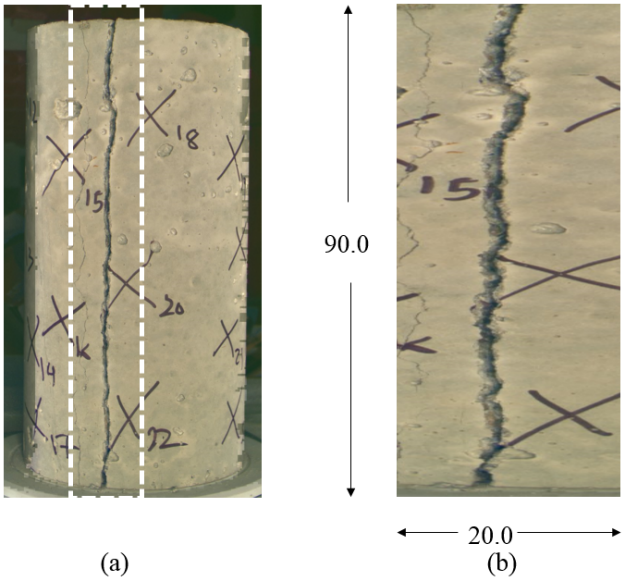

Figure 4.5: (a) Specimen 3 (scanned region shown by the dashed rectangle); and (b) zoom on the scanned region showing a long and narrow crack (dimensions in mm).

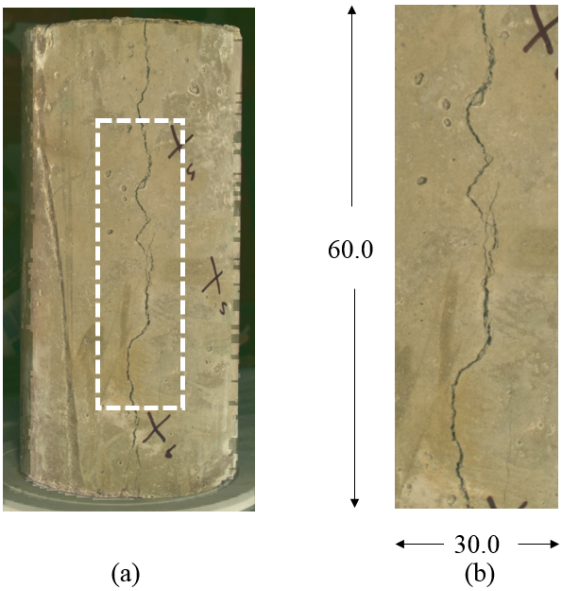

Figure 4.6: (a) Specimen 4 (scanned region shown by the dashed rectangle); and (b) zoom on the scanned region showing a shallow hairline crack (dimensions in mm).

4.3.1 Low-resolution fit

A total of 7954 data points was generated for specimen 1, each defined in terms of x, y, and z. The 7954 data points obtained from the 3D scanner have been fitted with a low-resolution surface using 27 nodes. Fig. 4.7(a) shows the fitting result of a crack and curvature for specimen 1. The compact representation provides a good fit of the 3D point cloud and includes an observable damage feature. In this case, 7954 data points have been compacted in 27 nodes that yielded a continuous surface, resulting in a 99.4% compression of data. The data compression rate taken as the change in size of the data set (e.g., size of original data set minus size of new data set) relative to the size of the original data set, where the size of the original data set is the number of laser coordinates multiplied by three (i.e., one data per axis) and the size of the new data set is the number of nodes in the network multiplied by five (i.e., one node has a value assigned over $\sigma_x, \sigma_y, \mu_x, \mu_y, and \gamma$). For specimen 2, a low-resolution fit was obtained using 199 nodes and 72.2% compression of data for crack localization. The original number of data points in this case was 1192. Similarly, 204 and 342 nodes were used to achieve a low-resolution representation of the cracks in specimens 3 and

4, respectively. The number of points originally present were 4461 and 2706, respectively. This resulted in 92.4% and 78.9% compression of data for specimen 3 and 4 respectively. The RMS errors of the low-resolution fit for all specimens, compared with the TLS data, are shown in Table 4.1. However, because the fit is low resolution, key features of the crack are now represented smoothly and will necessitate a higher resolution fit at its localization. Similarly, Fig. 4.7(b), Fig. 4.7(c), and Fig. 4.7(d) show the low resolution fit results for specimens 2, 3 and 4, respectively and Table 4.1 shows the summary of the quantitative results for the low-resolution fit for all four specimens.

Table 4.1: Summary of the results of low-resolution fit for all four specimens.

Specimen number	Original number of data points	Low-resolution number of nodes	Data compression (%)	Low-resolution RMS error (mm)
1	7954	27	99.4	2.8
2	1192	199	72.2	3.3
3	4461	204	92.4	1.8
4	2706	342	78.9	1.5

The number of wavelet selected for the low-resolution fit was automatically obtained after a minimal pre-tuning of the networks parameters. Note that minimal pre-tuning was required to achieve desirable results due to the single hidden layer of our NN architecture. A study was conducted on the accuracy of the representation as a function of the number of nodes in the network for specimen 1, by changing parameter λ while keeping all other network parameters constant. The accuracy was measured in terms of the RMS error. Fig. 4.8 is a plot of the RMS error as a function of the number of nodes. It also shows the relative computing time versus the network size. Results show a region in which the algorithm provides an optimal representation in terms of RMS error. This optimal representation occurs with 27 nodes. The decrease in performance for a higher number of nodes can be attributed to the other network parameters becoming highly mistuned. In particular, when more nodes are allowed in the network and the initial bandwidth is large, one would expect a relatively higher training period to obtain an acceptable level of accuracy. The relative computing time changes linearly with the number of nodes in the network, as expected.

Note that the nodes in this study are automatically generated using the SOM theory and depend on parameter λ.

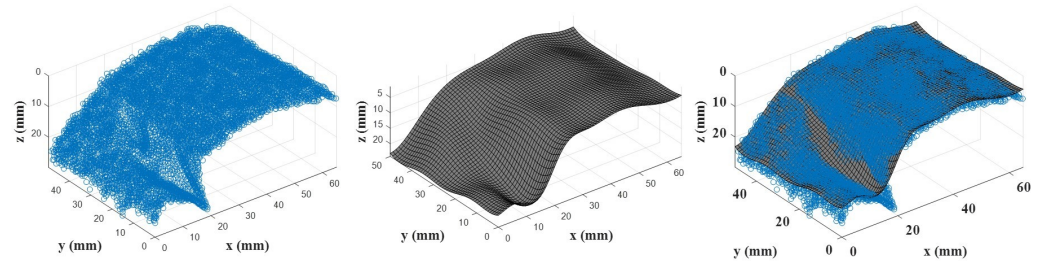

(a) Specimen 1

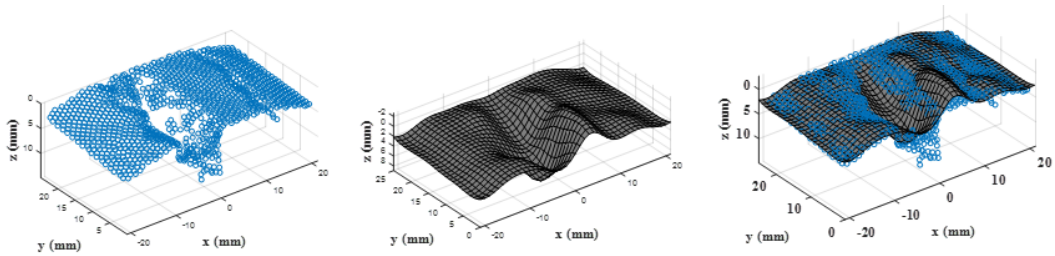

(b) Specimen 2

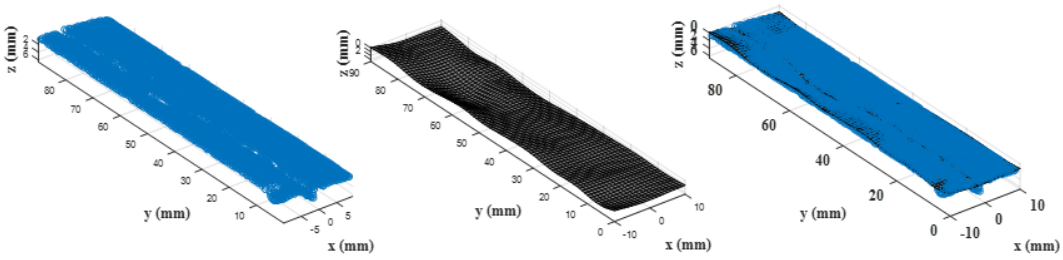

(c) Specimen 3

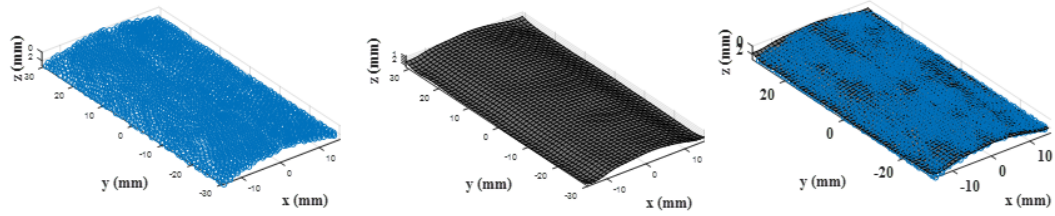

(d) Specimen 4

Figure 4.7: Point cloud (left); Compact low-resolution representation (middle); and Overlap of point cloud and representation (right) for the four specimens.

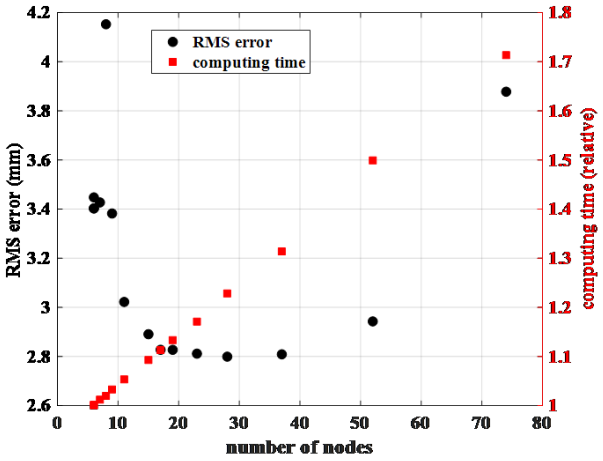

Figure 4.8: RMS error and relative computing time versus the wavelet network size.

4.3.2 Crack Localization

The spatial resolution of the low-resolution surface fit is used to detect cracks, based on the principle that a crack will provide a discontinuity in the surface, therefore necessitating higher resolution of nodes around the discontinuities. Using a grid search method, the 2-norm of the wavelet bandwidths $||\sigma||$ are computed, and a discontinuity is identified if the bandwidth falls below a threshold. This technique is illustrated in Fig. 4.9 (left), where the average nodal bandwidths are plotted over the x-y grid. Blue and dark blue areas indicate a higher concentration of wavelets, while green to red represent lower concentration of wavelets. For specimen 1, a crack region is localized at the x and y points for which the wavelet bandwidths fall under the average bandwidth value $||\sigma|| < 0.5(max(||\sigma||) + min(||\sigma||))$, as illustrated in Fig. 4.9(a) (right) by the black rectangular area. The black rectangular region is generated by averaging the four individual sides of the colored region. While this technique preserves information on salient damage, it results in filtering out some features that may be of interest. Other techniques enabling the automatic identification of damaged areas will be studied in future work. The figure also shows the true crack region (red trapezoidal and rectangular region), demonstrating that the algorithm can be successfully used to detect a crack and estimate its location. Remark that this detection and localization was achieved regardless of the curve in the concrete specimen, which could have been mistaken for damage if the algorithm

was based on nodal weights (value of z-axis). For specimen 2, the location of cracks is determined at the x and y points where the bandwidth values are under $||\sigma|| < 0.55(max(||\sigma||) + min(||\sigma||))$. A slightly larger value for the gain (0.55 instead of 0.50) was used for specimen 2 because the two difference cracks present in one data set, one was a thin hairline crack barely captured by the low-resolution fit. For implementing this method in the field, the automation of the gain selection would need to be addressed. Fig. 4.9(b) (right) shows the true crack location of the first crack (red trapezoidal region) and the second crack (red rectangle region) of specimen 2. Similarly, the values of the wavelet bandwidth associated with the localized region of the crack in specimen 3 fall under $||\sigma|| < 0.5(max(||\sigma||) + min(||\sigma||))$. Fig. 4.9(c) (right) shows the location of this crack. Negligible differences in the $||\sigma||$ values resulted in the failure of estimation of crack location for specimen 4, as shown in Fig. 4.9(d). An explanation for the failure to estimate the crack location of specimen 4 is that the depth of the hairline crack is very shallow (about 1 mm). The algorithm had no issues in determining the crack location for a deeper crack (about 4.5 mm) example seen in specimen 3. It is possible that the thin cracks in specimens 2 and 4 may not require any repair attention at the present condition.

4.3.3 High-resolution Fit

Once the location of a crack is localized, a higher resolution fit can be conducted around its region. For specimen 1, this region consists of 1644 data points, as plotted in Fig. 4.10(a). To provide a better surface fit, the data is rotated to optimize the uniqueness of the z values, in particular for 18 mm ¡ x ¡ 21 mm. The angle between the average values of z at x=9 mm and x=25 mm is automatically calculated as 45. Fig. 4.10(b) shows the rotated crack data. Fig. 4.10(c) shows the high-resolution compact representation of the crack obtained using 29 nodes. Fig. 4.10(d) displays the overlap between the crack point cloud and representation. The difference between the point cloud and the fit is defined as the error. For specimens 1, 2 and 3, the low-resolution fit had an RMS error of 2.8 mm, 3.3 mm, and 1.8 mm, respectively, compared with the TLS data. In specimen 1, a high-resolution representation of the crack is achieved using only 29

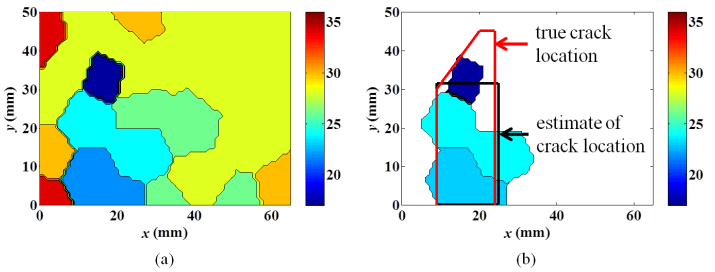

(a) Specimen 1

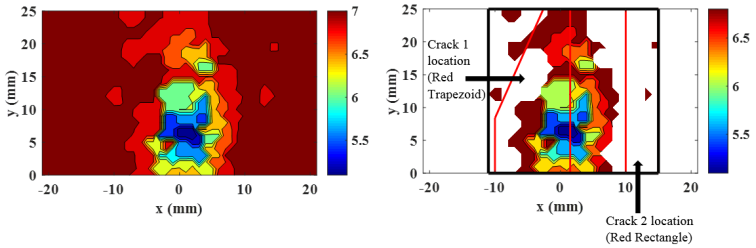

(b) Specimen 2

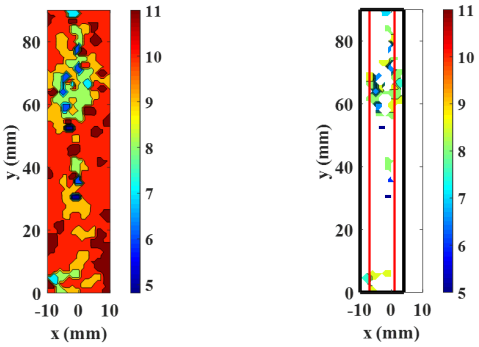

(c) Specimen 3

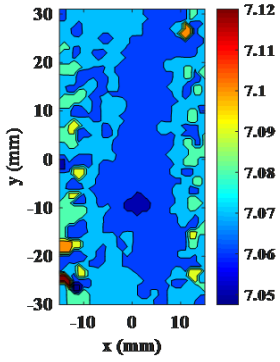

(d) Specimen 4

Figure 4.9: Contour plot of $||\sigma||$ (left); contour plot of only the estimate of crack location (right)

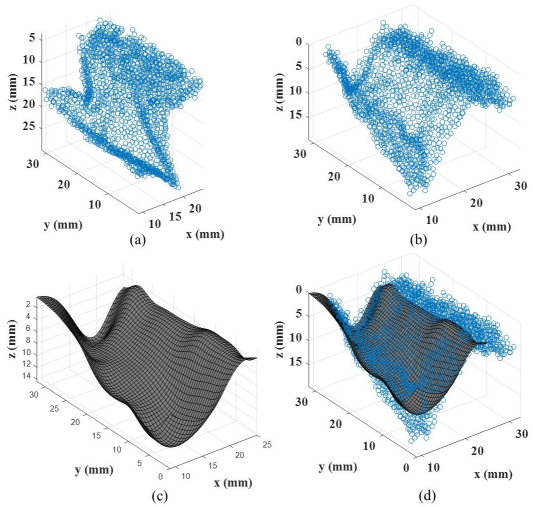

Figure 4.10: (a) Point cloud of crack data; (b) point cloud of rotated crack data; (c) compact high-resolution representation; and (d) overlap of point cloud and representation for specimen 1.

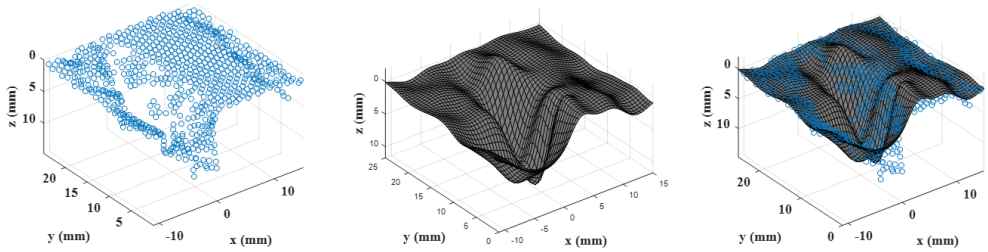

Figure 4.11: (a) Point cloud of crack data; (b) compact high-resolution representation; and (c) overlap of point cloud and representation for specimen 2 (rotation of crack data was not required for this specimen.

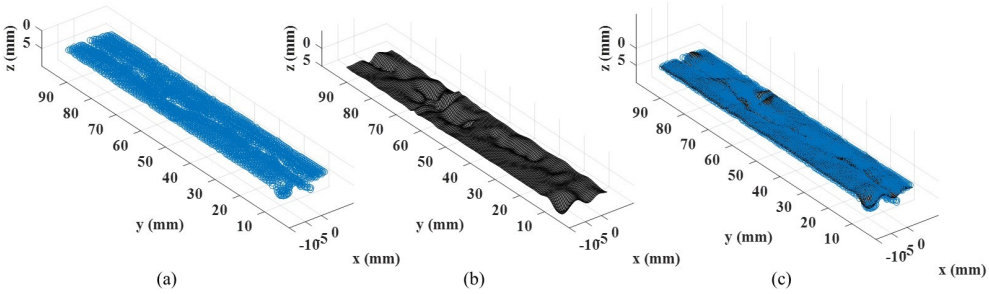

Figure 4.12: (a) Point cloud of crack data; (b) compact high-resolution representation; and (c) overlap of point cloud and representation for specimen 3.

nodes, resulting in a 97.1% data compression, plotted in Fig. 4.10(c). With the high-resolution fit, the RMS error dropped to 1.8 mm, showing a 35.7% improvement. Similarly, a high-resolution fit for data for specimens 2 and 3 were obtained using 254 and 653 nodes, respectively. This resulted in 42.5% and 63.9% compression of data in specimens 2 and 3, respectively. Furthermore, the RMS errors for the high-resolution fit were 2.6 mm and 1.4 mm, which improved by 21.2% and 22.2%, respectively. The resulting RMS errors are attributable to noise present in the TLS data. Note that the RMS errors for the high-resolution fit were computed using the localized data set after the extraction of the crack information. Figs. 4.11 and 4.12 show the point cloud of the cracked data, high-resolution representation and overlap of point cloud and representation for specimens 2 and 3. The quantitative results of the high-resolution fit for all specimens are summarized in Table 2.

Table 4.2: Summary of the results of high-resolution fit for all four specimens.

Specimen number	Original number of data points	Number of data points for crack	High-resolution number of nodes	Data compression (%)	High-resolution RMS error (mm)
1	7954	1644	29	97.1	1.8
2	1192	736	254	42.5	2.6
3	4461	3011	653	63.9	1.4
4	2706	N/A	N/A	N/A	N/A

4.4 Conclusions and Future Work

A strategy to sequentially construct a compact representation of a 3D point cloud has been presented. This adaptive wavelet neural network is capable of self-organization, self-adaptation, and sequential learning. It can be utilized to transform thousands of 3D point cloud data obtained from a TLS or any type of LiDAR into a small set of functions and identify problem areas. The proposed wavelet network has been applied on four cracked cylindrical specimens. It was shown that the algorithm was capable of replacing a set of 7954 3D coordinates with a set of 27 functions for the first specimen while preserving the key features of the scan data, which included a crack. Similarly, 1192, 4461 and 2706 points were compacted into 199, 204 and 342 wavelets, respectively, for specimens 2, 3 and 4. These four compact representations had RMS errors of 2.8 mm, 3.3 mm, 1.8 mm and 1.5 mm,

but compressed memory usage by 99.4%, 72.2%, 92.4% and 78.9%, respectively. By looking at local regions of wavelets with smaller bandwidths, it was demonstrated that an automatic crack detection strategy can be employed to make further high-resolution analysis only on regions with damage. The high-resolution fit of the crack region of 1644, 736 and 3011 points were represented with a set of 29, 254 and 653 functions, respectively, for specimens 1, 2 and 3. This resulted in data compression of 97.1%, 42.5% and 63.9%, respectively. RMS errors for specimens for 1, 2 and 3 were 1.8 mm, 2.6 mm, and 1.4 mm respectively, demonstrating 35.7%, 21.2% and 22.2% improvements in the low-resolution representation. This technique was not capable of detecting a crack in specimen 4 which had a hairline, shallow crack feature. However, such damage is typically minor in concrete structures and does not require attention. The proposed technique allows for smaller memory usage, faster computational times, and accurate representations of problem areas. It was also demonstrated that the proposed crack detection strategy is capable of detecting damages on curved surfaces. Future research will investigate applying the proposed technique to data collected from an actual bridge. The developed methodology will be tested to guide a TLS real-time to construct accurate representation containing features of interest. This is possible as the network we have developed in this study is self-organizing, self-adaptive and sequential. Lastly, the sequential feature refers to the capability of the network to learn in a sequential manner, as opposed to batch processing. We built this sequential feature for real-time applications in combination with a controllable TLS.

4.5 References

[1] "2017 infrastructure report card." https://www.infrastructurereportcard.org/, 2017.

[2] H. Petroski, *The Road Taken: The History and Future of Americas Infrastructure*. Bloomsbury Publishing USA, 2016.

[3] B. M. Phares, D. D. Rolander, B. A. Graybeal, and G. A. Washer, "Reliability of visual bridge inspection," *Public Roads*, vol. 64, pp. 22–29, 2001.

[4] B. M. Phares, G. A. Washer, D. D. Rolander, B. A. Graybeal, and M. Moore, "Routine highway bridge inspection condition documentation accuracy and reliability," *Journal of Bridge Engineering*, vol. 9, p. 403413, 2004.

[5] B. Conde-Carnero, B. Riveiro, P. Arias, and J. Caamaño, "Exploitation of geometric data provided by laser scanning to create fem structural models of bridges," *Journal of Performance of Constructed Facilities*, vol. 30, no. 3, p. 04015053, 2015.

[6] L. Truong-Hong, H. Falter, D. Lennon, and D. F. Laefer, "Framework for bridge inspection with laser scanning," *In: EASEC-14 Structural Engineering and Construction, Ho Chi Minh City, Vietnam*, pp. 1–9, 2016.

[7] Y. Turkan, S. Laflamme, and L. Tan, "Terrestrial laser scanning-based bridge structural condition assessment," *Tech Transfer Summaries*, pp. 1–38, 2016.

[8] R. Parrillo, R. Roberts, and A. Haggan, "Bridge deck condition assessment using ground penetrating radar," *Proceedings of the ECNDT, Berlin, German*, vol. 2526, p. 112, 2006.

[9] Z. W. Wang, M. Zhou, G. G. Slabaugh, J. Zhai, and T. Fang, "Automatic detection of bridge deck condition from ground penetrating radar images," *IEEE Transactions on Automation Science and Engineering*, vol. 8, pp. 633–640, 2011.

[10] J. Hugenschmidt, "Concrete bridge inspection with a mobile gpr system," *Construction and Building Materials*, 2002.

[11] A. Ellenberg, L. Branco, A. Krick, I. Bartoli, and A. Kontsos, "Use of unmanned aerial vehicle for quantitative infrastructure evaluation," *Journal of Infrastructure Systems*, vol. 21, no. 3, p. 04014054, 2014.

[12] B. Chan, H. Guan, J. Jo, and M. Blumenstein, "Towards uav-based bridge inspection systems: A review and an application perspective," *Structural Monitoring and Maintenance*, vol. 2, no. 3, pp. 283–300, 2015.

[13] M. Gheisari and J. Irizarry, "A user-centered approach to investigate unmanned aerial system (uas) requirements for a department of transportation applications," in *Conference on Autonomous and Robotic Construction of Infrastructure*, p. 85, 2015.

[14] J. Irizarry and D. B. Costa, "Exploratory study of potential applications of unmanned aerial systems for construction management tasks," *Journal of Management in Engineering*, vol. 32, no. 3, p. 05016001, 2016.

[15] D. Mader, R. Blaskow, P. Westfeld, and C. Weller, "Potential of uav-based laser scanner and multispectral camera data in building inspection," *ISPRS - International Archives of the Photogrammetry, Remote Sensing and Spatial Information Sciences*, p. 11351142, 2016.

[16] M. Skibniewski and M. Golparvar-Fard, "Toward a science of autonomy for physical systems: Construction," *A white paper prepared for the Computing Community Consortium committee of the Computing Research Association*, 2015.

[17] Y. Ham, K. K. Han, J. J. Lin, and M. Golparvar-Fard, "Visual monitoring of civil infrastructure systems via camera-equipped unmanned aerial vehicles (uavs): a review of related works," *Visualization in Engineering*, vol. 4, no. 1, p. 1, 2016.

[18] M. N. Gillins, "Unmanned aircraft systems for bridge inspection: Testing and developing end-to-end operational workflow," *Oregon State University*, 2016.

[19] V. Kasireddy, S. Ergan, B. Akinci, and N. S. Gulgec, "Visualization requirements of engineers for risk assessment of embankment dams," *Visualization in Engineering*, vol. 3, no. 1, p. 1, 2015.

[20] F. A. Al-Shalabi, Y. Turkan, and S. Laflamme, "Brim implementation for documentation of bridge condition for inspection," in *Proceedings of the Canadian Society for Civil Engineering*

5th International/11th Construction Specialty Conference, University of British Columbia, Vancouver, Canada. June, pp. 7–10, 2015.

[21] B. Mcguire, R. Atadero, C. Clevenger, and M. Ozbek, "Bridge information modeling for inspection and evaluation," *Journal of Bridge Engineering*, vol. 21, p. 04015076, 2016.

[22] A. Costin, *A new methodology for interoperability of heterogeneous bridge information models*. PhD thesis, Georgia Institute of Technology, 2016.

[23] T. Mckenna, M. Minehane, B. Okeeffe, G. Osullivan, and K. Ruane, "Bridge information modelling (brim) for a listed viaduct," *Proceedings of the Institution of Civil Engineers - Bridge Engineering*, vol. 170, pp. 192–203, 2017.

[24] C. Koch, K. Georgieva, V. Kasireddy, B. Akinci, and P. W. Fieguth, "A review on computer vision based defect detection and condition assessment of concrete and asphalt civil infrastructure.," *Advanced Engineering Informatics*, vol. 29, no. 2, pp. 196–210, 2015.

[25] I. Abdel-Qader, S. Pashaie-Rad, O. Abudayyeh, and S. Yehia, "Pca-based algorithm for unsupervised bridge crack detection," *Advances in Engineering Software*, vol. 37, pp. 771–778, 2006.

[26] T. Yamaguchi, S. Nakamura, R. Saegusa, and S. Hashimoto, "Image-based crack detection for real concrete surfaces," *IEEJ Transactions on Electrical and Electronic Engineering*, vol. 3, pp. 128–135, 2008.

[27] T. Yamaguchi and S. Hashimoto, "Fast crack detection method for large-size concrete surface images using percolation-based image processing," *Machine Vision and Applications*, vol. 21, pp. 797–809, 2010.

[28] P. Prasanna, K. Dana, N. Gucunski, and B. Basily, "Computer-vision based crack detection and analysis," *In: Sensors and Smart Structures Technologies for Civil, Mechanical, and Aerospace Systems*, p. 834542, 2012.

[29] I. Abdel-Qader, O. Abudayyeh, and M. Kelly, "Analysis of edge-detection techniques for crack identification in bridges," *Journal of Computing in Civil Engineering*, vol. 17, pp. 255–263, 2003.

[30] C. Koch, S. G. Paal, A. Rashidi, Z. Zhu, M. König, and I. Brilakis, "Achievements and challenges in machine vision-based inspection of large concrete structures," *Advances in Structural Engineering*, vol. 17, no. 3, pp. 303–318, 2014.

[31] R. Adhikari, O. Moselhi, and A. Bagchi, "A study of image-based element condition index for bridge inspection," *Proceedings of the 30th International Symposium on Automation and Robotics in Construction and Mining*, 2013.

[32] S. German, I. Brilakis, and R. DesRoches, "Rapid entropy-based detection and properties measurement of concrete spalling with machine vision for post-earthquake safety assessments," *Advanced Engineering Informatics*, vol. 26, no. 4, pp. 846–858, 2012.

[33] S. Chen, "Laser scanning technology for bridge monitoring," in *Laser Scanner Technology*, InTech, 2012.

[34] S.-E. Chen, W. Liu, H. Bian, and B. Smith, "3d lidar scans for bridge damage evaluations," in *Forensic Engineering 2012: Gateway to a Safer Tomorrow*, pp. 487–495, 2013.

[35] M. J. Olsen, Z. Chen, T. Hutchinson, and F. Kuester, "Optical techniques for multiscale damage assessment," *Geomatics, Natural Hazards and Risk*, vol. 4, pp. 49–70, 2013.

[36] Q. Meng, B. Li, H. Holstein, and Y. Liu, "Parameterization of point-cloud freeform surfaces using adaptive sequential learning rbf networks," *Pattern Recognition*, vol. 46, p. 23612375, 2013.

[37] A. Gálvez and A. Iglesias, "Particle swarm optimization for non-uniform rational b-spline surface reconstruction from clouds of 3d data points," *Information Sciences*, vol. 192, pp. 174–192, 2012.

[38] C. Wang, Z. Shi, L. Li, and X. Niu, "Adaptive parameterization and reconstruction of 3d face images using partial differential equations," *IJACT International Journal of Advancements in Computing Technology*, vol. 4, pp. 214–221, 2012.

[39] J. Barhak and A. Fischer, "Parameterization and reconstruction from 3d scattered points based on neural network and pde techniques," *IEEE Transactions on Visualization and Computer Graphics*, vol. 7, no. 1, pp. 1–16, 2001.

[40] F. Bellocchio, N. Borghese, S. Ferrari, and V. Piuri, "Hierarchical radial basis functions networks," *3D Surface Reconstruction*, pp. 77–110, 2013.

[41] S. Suresh, S. Narasimhan, and N. Sundararajan, "Adaptive control of nonlinear smart base-isolated buildings using gaussian kernel functions," *Structural Control and Health Monitoring*, vol. 15, p. 585603, 2008.

[42] R. J. Howlett and L. C. Jain, *Radial basis function networks 1: recent developments in theory and applications*, vol. 66. Springer Science & Business Media, 2001.

[43] T. Kohonen, "The self-organizing map," *Proceedings of the IEEE*, vol. 78, no. 9, pp. 1464–1480, 1990.

[44] J. J. C. S. Laflamme, "Application of self-tuning gaussian networks for control of civil structures equipped with magnetorheological dampers," *Active and Passive Smart Structures and Integrated Systems*, pp. 1–13, 2009.

[45] S. Laflamme, J. E. Slotine, and J. Connor, "Self-organizing input space for control of structures," *Smart Materials and Structures*, vol. 21, no. 11, p. 115015, 2012.

[46] Q. Zhang and A. Benveniste, "Wavelet networks," *IEEE Transactions on Neural Networks*, vol. 3, pp. 889–898, 1992.

[47] A. D. Doulamis, N. D. Doulamis, and S. D. Kollias, "On-line retrainable neural networks: improving the performance of neural networks in image analysis problems," *IEEE Transactions on Neural Networks*, vol. 11, no. 1, pp. 137–155, 2000.

[48] S. Haykin, *Nonlinear methods of spectral analysis*, vol. 34. Springer Science & Business Media, 2006.

[49] N. Metni and T. Hamel, "A uav for bridge inspection: Visual servoing control law with orientation limits," *Automation in Construction*, vol. 17, pp. 3–10, 2007.

[50] C. Eschmann, C.-M. Kuo, C.-H. Kuo, and C. Boller, "Unmanned aircraft systems for remote building inspection and monitoring," in *Proceedings of the 6th European Workshop on Structural Health Monitoring, Dresden, Germany*, vol. 36, 2012.

[51] S. Sankarasrinivasan, E. Balasubramanian, K. Karthik, U. Chandrasekar, and R. Gupta, "Health monitoring of civil structures with integrated uav and image processing system," *Procedia Computer Science*, vol. 54, p. 508515, 2015.

[52] G. Moussa and K. Hussain, "A new technique for automatic detection and parameters estimation of pavement crack," *In: 4th International Multi-Conference on Engineering Technology Innovation, IMETI*, pp. 1–6, 2011.

[53] J. Valena, D. D. Da-Costa, E. Jlio, H. Arajo, and H. Costa, "Automatic crack monitoring using photogrammetry and image processing, measurement," *Measurement*, vol. 46, pp. 433–441, 2013.

[54] M. R. Jahanshahi and S. F. Masri, "A new methodology for non-contact accurate crack width measurement through photogrammetry for automated structural safety evaluation," *Smart materials and structures*, vol. 22, no. 3, p. 035019, 2013.

[55] R. Montero, J. G. Victores, S. Martinez, A. Jardn, and C. Balaguer, "Past, present and future of robotic tunnel inspection," *Automation in Construction*, vol. 59, pp. 99–112, 2015.

[56] K. Makantasis, E. Protopapadakis, A. Doulamis, N. Doulamis, and C. Loupos, "Deep convolutional neural networks for efficient vision based tunnel inspection," *IEEE International Conference on Intelligent Computer Communication and Processing (ICCP)*, pp. 335–342, 2015.

[57] C. Stentoumis, E. Protopapadakis, A. Doulamis, and N. Doulamis, "A holistic approach for inspection of civil infrastructures based on computer vision techniques," *ISPRS - International Archives of the Photogrammetry, Remote Sensing and Spatial Information Sciences*, vol. 41, p. 131138, 2016.

[58] K. Loupos, A. D. Doulamis, C. Stentoumis, E. Protopapadakis, K. Makantasis, N. D. Doulamis, A. Amditis, P. Chrobocinski, J. Victores, R. Montero, *et al.*, "Autonomous robotic system for tunnel structural inspection and assessment," *International Journal of Intelligent Robotics and Applications*, p. 124, 2017.

[59] E. Protopapadakis, C. Stentoumis, N. Doulamis, A. Doulamis, K. Loupos, K. Makantasis, G. Kopsiaftis, and A. Amditis, "Autonomous robotic inspection in tunnels," *ISPRS Annals of the Photogrammetry, Remote Sensing and Spatial Information Sciences*, vol. 3, p. 167, 2016.

[60] M. I. Alba, L. Barazzetti, M. Scaioni, E. Rosina, and M. Previtali, "Mapping infrared data on terrestrial laser scanning 3d models of buildings," *Remote Sensing*, vol. 3, no. 9, pp. 1847–1870, 2011.

[61] G. Vosselman and H. G. Maas, *Airborne and Terrestrial Laser Scanning*. Whittles Publishing, Dunbeath, 2010.

[62] X. Xiong, A. Adan, B. Akinci, and D. Huber, "Automatic creation of semantically rich 3d building models from laser scanner data," *Automation in Construction*, vol. 31, pp. 325–337, 2013.

[63] G. S. Cheok, S. Leigh, and A. Rukhin, "Calibration experiments of a laser scanner," *NASA STI/Recon Technical Report N*, vol. 2, 2002.

[64] T. Greaves and B. Jenkins, "3d laser scanning market red hot: 2006 industry revenues $253 million, 43% growth," *Spar Point Res. 200*, p. 7, 2007.

[65] W. Boehler, M. B. Vicent, A. Marbs, *et al.*, "Investigating laser scanner accuracy," *The International Archives of Photogrammetry, Remote Sensing and Spatial Information Sciences*, vol. 34, no. Part 5, pp. 696–701, 2003.

[66] J. Teizer, C. Kim, C. Haas, K. Liapi, and C. Caldas, "Framework for real-time three-dimensional modeling of infrastructure," *Transportation Research Record: Journal of the Transportation Research Board*, p. 177186, 2005.

[67] C. Kim, C. T. Haas, and K. A. Liapi, "Rapid, on-site spatial information acquisition and its use for infrastructure operation and maintenance," *Automation in Construction*, vol. 14, no. 5, pp. 666–684, 2005.

[68] L. Klein, N. Li, and B. Becerik-Gerber, "Imaged-based verification of as-built documentation of operational buildings," *Automation in Construction*, vol. 21, pp. 161–171, 2012.

[69] H. Hajian and G. Brandow, "As-built documentation of structural components for reinforced concrete construction quality control with 3d laser scanning," in *Computing in Civil Engineering (2012)*, pp. 253–260, 2012.

[70] K. S. Yen, T. A. Lasky, and B. Ravani, "Cost-benefit analysis of mobile terrestrial laser scanning applications for highway infrastructure," *Journal of Infrastructure Systems*, vol. 20, p. 04014022, 2014.

[71] P. Oskouie, B. Becerik-Gerber, and L. Soibelman, "Automated measurement of highway retaining wall displacements using terrestrial laser scanners," *Automation in Construction*, vol. 65, p. 86101, 2016.

[72] C. Rausch, M. Nahangi, C. Haas, J. West, and M. Perreault, "Deviation analysis: A tool for quantifying dimensional quality and alignment in modular construction," *CSCE Annual Conference, London, ON*, pp. 360–369, 2016.

[73] H. S. Park, H. M. Lee, H. Adeli, and I. Lee, "A new approach for health monitoring of structures: Terrestrial laser scanning," *Computer Aided Civil and Infrastructure Engineering*, vol. 22, pp. 19–30, 2007.

[74] M. J. Olsen, F. Kuester, B. J. Chang, and T. C. Hutchinson, "Terrestrial laser scanning-based structural damage assessment," *Journal of Computing in Civil Engineering*, vol. 24, p. 264272, 2009.

[75] T. Werner and D. Morris, "3d laser scanning for masonry arch bridges," *In: Proceedings of FIG Congress, Facing the Challenges - Building the Capacity, Sydney, Aust.*, 2010.

[76] C. Meral, "Evaluation of laser scanning technology for bridge inspection," *Drexel University*, 2011.

[77] R. L. Wood, T. C. Hutchinson, C. E. Wittich, and F. Kuester, "Characterizing cracks in the frescoes of sala degli elementi within florences palazzo vecchio," *Progress in Cultural Heritage Preservation Lecture Notes in Computer Science*, p. 776783, 2012.

[78] E. B. Anil, B. Akinci, J. H. Garrett, and O. Kurc, "Characterization of laser scanners for detecting cracks for post-earthquake damage inspection," in *ISARC. Proceedings of the International Symposium on Automation and Robotics in Construction*, vol. 30, p. 1, Vilnius Gediminas Technical University, Department of Construction Economics , 2013.

[79] R. Adhikari, Z. Zhu, O. Moselhi, and A. Bagchi, "Automated bridge condition assessment with hybrid sensing," in *ISARC. Proceedings of the International Symposium on Automation and Robotics in Construction*, vol. 30, p. 1, Vilnius Gediminas Technical University, Department of Construction Economics , 2013.

[80] K. M. Mosalam, S. M. Takhirov, and S. Park, "Applications of laser scanning to structures in laboratory tests and field surveys," *Structural Control and Health Monitoring*, vol. 21, p. 115134, 2014.

[81] J.-H. Chen, M.-C. Su, R. Cao, S.-C. Hsu, and J.-C. Lu, "A self organizing map optimization based image recognition and processing model for bridge crack inspection," *Automation in Construction*, vol. 73, pp. 58–66, 2017.

[82] X. Xu, H. Yang, and I. Neumann, "Concrete crack measurement and analysis based on terrestrial laser scanning technology," *Sensors and Tranducers Journal*, vol. 186, pp. 168–172, 2015.

[83] R. Zeibak-Shini, R. Sacks, L. Ma, and S. Filin, "Towards generation of as-damaged bim models using laser-scanning and as-built bim: First estimate of as-damaged locations of reinforced concrete frame members in masonry infill structures," *Advanced Engineering Informatics*, vol. 30, pp. 312–326, 2016.

[84] J. Valena, I. Puente, E. Jlio, H. Gonzlez-Jorge, and P. Arias-Snchez, "Assessment of cracks on concrete bridges using image processing supported by laser scanning survey," *Construction and Building Materials*, vol. 146, pp. 668–678, 2017.

[85] T. Kohonen, "The self-organizing map," *Neurocomputing*, vol. 21, no. 1–3, pp. 1–6, 1998.

CHAPTER 5. VARIABLE INPUT OBSERVER FOR NONSTATIONARY HIGH-RATE DYNAMIC SYSTEMS

J. Hong, S. Laflamme, D. J. Cao, L., and B. Joyce

Abstract

Engineering systems experiencing events of amplitudes higher than 100 g_n for a duration under 100 ms, here termed high-rate dynamics, can undergo rapid damaging effects. If the structural health of such systems could be accurately estimated in a timely manner, preventative measures could be employed to minimize adverse effects. For complex high-rate problems, adaptive observers have shown promise due to their capability to deal with nonstationary, noisy, and uncertain systems. However, adaptive observers have slow convergence rates, which impedes their applicability to the high-rate problems. To improve on the convergence rate, we propose a variable input space concept for optimizing the use of data history of high-rate dynamics, with the objective to produce an optimal representation of the system of interest. Using the embedding theory, the algorithm sequentially selects and adapts a vector of inputs that preserves the essential dynamics of the high-rate system. In this paper, the variable input space is integrated in a wavelet neural network, which constitutes a variable input observer. The observer is simulated using experimental data from a high rate system. Different input space adaptation methods are studied and the performance is also compared against an optimized fixed input strategy. It is found that a smooth transition of the input space eliminates error spikes and yields faster convergence. The variable input observer is further studied in a hybrid model-/data-driven formulation, and results demonstrate significant improvement in performance gained from the added physical knowledge.

5.1 Introduction

High-rate dynamics, here defined as events of amplitudes higher than 100 g_n for a duration under 100 ms, can be highly detrimental to modern engineering systems. Examples of such systems include civil structures exposed to blast, passenger vehicles experiencing collisions, and aerial or spacecraft vehicles impacting foreign objects [1]. High-rate dynamics can cause rapid plastic deformation propagating through the structure and to electronics and sensors, which in turn can cause catastrophic failures and endanger human lives [2]. Precise and on-time state estimation is a necessary first step to prevent further damage and complete failure [3]. However, state estimation of high-rate dynamics is a challenging problem. A well-designed estimator must converge very fast (high-rate) and be capable of coping with the following unique complexities that characterize the high-rate problem:

- large uncertainties in the external loads;
- high levels of nonstationarities and heavy disturbances; and
- generations of unmodeled dynamics from changes in system configuration.

In particular, an estimator must be capable of operating through noise, uncertainty, time-varying parameters/states, and disturbances. Noise is a common issue that can arise from flexing of electronics. There is uncertainty in how a system may respond to very large excitations. In the case of a spontaneous blast or impact, little is known about the inputs. Plastic deformation or damage leads to time-varying parameters or states. Lastly, large excitations can resonate the system or components resulting in disturbances. Sophistication in the algorithm is required to overcome the negative effects of the combined complexities leading to slower convergence rates [4, 5, 6, 7, 8].

Classic observers are constructed to estimate one or more states from sensor inputs. Typically, inputs are pre-selected and rarely optimized, contributing to a sub-optimal observer design. Hong et al. [1] discussed promising properties of adaptive observers (AOs), in general, to perform well in

the presence of various system complexities (e.g. noise, uncertainty, time-varying parameters, and disturbance mentioned above). However, it was also discussed that these observers are characterized by slower convergence rates due to their adaptive architecture. Various methods have been developed to increase the convergence rate of AOs, see [9, 10, 11] for instance. While such research has yielded important contributions in ameliorating the convergence of AOs, all of the methods focused on altering the estimation and adaptation algorithm, while the input space selection and construction are vastly overlooked [12].

Typical observers employ representations that are tuned to fixed types of inputs to attain an appropriate level of performance [13, 14]. The choice of inputs influences computation time, adaptation speed, effects of the curse of dimensionality, understanding of the representation, and model complexity [15, 16]. Although in practice only limited states in a system can be observed, the essential dynamics may be preserved through a proper selection of the input space vector based on limited measurements [17, 18]. Bowden et al. [13] argued that proper input space selection can lead to superior estimators by bypassing modeling inaccuracies due to nonlinearities. The benefits of essential dynamics present in an input space has been studied in fields of structural health monitoring [19] [20] [21] and control [14, 22, 23, 24, 25].

It follows that a strategy is to employ a dynamic input space to provide stability of the adaptive algorithm. The change in the input types and numbers can help target inputs that would contain the essential dynamics of the system. A critical advantage of such methodology is that the essential dynamics can be extracted from nonstationary systems [12] using limited sensors [26]. The authors have studied varying input space strategies for structural control applications [12, 27, 18], and recently for high-rate state estimation [28].

The decision to take an adaptive algorithm approach was determined from an overview study of observers and their general applications [1]. Due to the difficulties in creating a representation of high-rate systems, adaptive data-driven observers were found to have an unique advantage of adapting to large levels of uncertainties and complexities through pattern recognition capabilities [29]. The downfall of adaptive methods, however, is their slow convergence rates. In order to

accelerate the convergence times, the input space of observers was studied [28]. It was determined that the input space of observers was critical to the quality of estimates observers can produce for high-rate systems.

The method of varying the input space produces a variable input observer (VIO) when used as an estimator. Here, the estimator is comprised of the variable input space coupled with a self-organizing single-layer wavelet neural network. The single-layer wavelet architecture is selected for its known universal approximation capabilities [30], ideal for mapping complex nonlinear dynamics [31] and real-time computations due to fewer number of calculations [32]. The input space of the estimator is varied sequentially in real-time, to adapt to complexities of high-rate dynamics, including nonlinearities and nonstationarities. Such variation allows the state estimation function to adapt to changing dynamics resulting in a minimum number of inputs that preserve the system's essential dynamics leading to faster convergence rates.

Systems that initially behave in a linear manner can respond nonlinearly when damaged [19]. Such nonstationarities are inherent attributes of high-rate systems. Liu et al. [21] verified that damage assessment using an embedding strategy provided superior results compared with the same strategy without embedding. Previous embedding techniques were only applicable to stationary systems, where offline processing was used to determine the embedding parameters [33, 34]. Through the VIO, we extend the embedding strategy to nonstationary systems through the online computation of the embedding over stationary segments of data.

In prior work presented in conference proceedings, a preliminary version of the VIO showed promise when compared with a typical fixed input space observer [35]. However, the rapid input space adaptation produced undesirable error spikes in the estimations, and the authors demonstrated that a slower transition of the input space reduced these error spikes [36].

In this paper, we introduce a smooth transition technique between input spaces by applying a c^{∞} type function to the time delay values with the objective to eliminate error spikes, and also further previous studies by examining the effects of added physical knowledge into the system by

creating a hybrid data-/model-driven VIO. Lastly, we explore the possibility of using this hybrid observer for system identification applications through pre-training.

The rest of the paper is organized as follows. Section 5.2 will present the methodology used in constructing the VIO, model, and hybrid VIO. Section 5.3 will describe the experimental setup used for acquiring data used in the numerical simulations, and discuss simulation results. Section 5.4 will conclude the paper with a summary of major findings.

5.2 Background

5.2.1 Variable Input Observer

The variable input space strategy is combined with a wavelet neural network (WNN) to perform state estimation, therefore constituting the VIO. Its architecture is illustrated in Fig. 5.1. A single layer of Mexican hat wavelet network is used to produce the estimate $\hat{y}_2(k)$

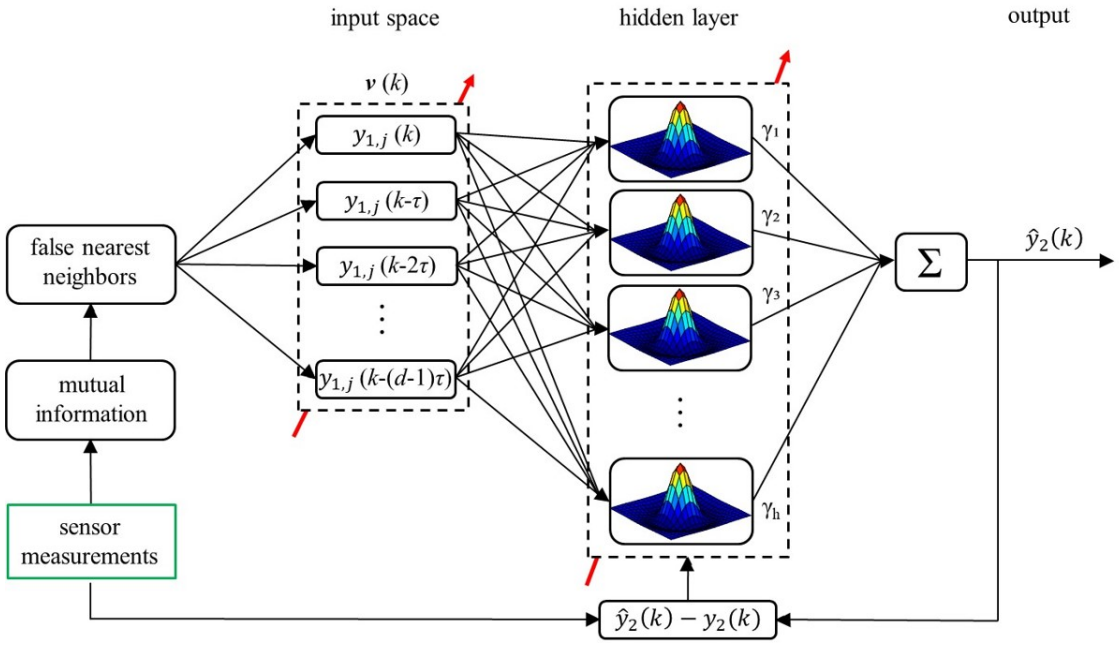

Figure 5.1: Variable input observer's architecture.

$$\hat{y}_2(k) = \sum_{j=1}^{h} \gamma_j \phi_j(\boldsymbol{\nu}(k)) \tag{5.1}$$

where $\boldsymbol{\nu}$ is the input vector also termed delay vector, τ the time delay, d the embedding dimension, h the number of nodes or activation functions, γ the nodal weights, and ϕ the Mexican hat wavelet activation function

$$\phi_j(\boldsymbol{\nu}(k)) = \left(1 - \frac{\|\boldsymbol{\nu}(k) - \boldsymbol{\mu_j}\|_2}{\boldsymbol{\sigma_j^2}}\right) e^{-\frac{\|\boldsymbol{\nu}(k)-\boldsymbol{\mu_j}\|_2}{\boldsymbol{\sigma_j^2}}} \tag{5.2}$$

where $\boldsymbol{\mu_j}$ and $\boldsymbol{\sigma_j}$ are the center and bandwidth of the j^{th} node, respectively, and $\|\cdot\|_2$ is the 2-norm. The VIO is specifically designed to self-organize based on Kohonen's self-organizing map (SOM) theory [37], and to perform self-adaptation. The SOM functionality consists of adding nodes when a new sample falls outside the region covered by the WNN. When a new node j is added, it is given a weight γ_j initially equal to zero, a center $\boldsymbol{\mu}_j$ at the location of the new observation, and a bandwidth $\boldsymbol{\sigma}_j$ set at the user-defined value $\sigma(0)$. Self-adaptation consists of sequentially adapting the WNN parameters $\boldsymbol{\gamma}$ and $\boldsymbol{\sigma}$ following a stable back-propagation rule [38]:

$$\begin{aligned} \dot{\boldsymbol{\gamma}}_j(k) &= -\Gamma_{\boldsymbol{\gamma}_j} \frac{\partial E(k)}{\partial \boldsymbol{\gamma}_j} \\ \dot{\boldsymbol{\sigma}}_j(k) &= -\Gamma_{\boldsymbol{\sigma}_j} \frac{\partial E(k)}{\partial \boldsymbol{\sigma}_j} \end{aligned} \tag{5.3}$$

where $\Gamma_{\boldsymbol{\gamma}_j}$ and $\Gamma_{\boldsymbol{\sigma}_j}$ are positive learning rates for $\boldsymbol{\gamma}_j$ and $\boldsymbol{\sigma}_j$ and E is the error function

$$E(k) = \frac{1}{2}(\tilde{y}_2(k))^2 = \frac{1}{2}\left(\sum_{j=1}^{h} \gamma_j \phi_j(\boldsymbol{\nu}(k)) - y_2(k)\right)^2 \tag{5.4}$$

where $\tilde{y}_2(k) = \hat{y}_2(k) - y_2(k)$ is the estimation error.

Substituting Eq. (5.4) into Eq. (5.3) gives

$$\begin{aligned}\dot{\boldsymbol{\gamma}}_j(k) &= -\Gamma_{\boldsymbol{\gamma}_j}\frac{\partial\left(\frac{1}{2}\left(\sum_{j=1}^{h}\gamma_j\phi_j(\boldsymbol{\nu}(k))-y_2(k)\right)^2\right)}{\partial\boldsymbol{\gamma}_j}\\ &= -\Gamma_{\boldsymbol{\gamma}_j}\left(\sum_{j=1}^{h}\phi_j(\boldsymbol{\nu}(k))\right)\left(\sum_{j=1}^{h}\gamma_j\phi_j(\boldsymbol{\nu}(k))-y_2(k)\right)\\ &= -\Gamma_{\boldsymbol{\gamma}_j}\left(\sum_{j=1}^{h}\phi_j(\boldsymbol{\nu}(k))\right)\tilde{y}_2(k)\end{aligned} \tag{5.5}$$

and

$$\begin{aligned}\dot{\boldsymbol{\sigma}}_j(k) &= -\Gamma_{\boldsymbol{\sigma}_j}\frac{\partial\left(\frac{1}{2}\left(\sum_{j=1}^{h}\gamma_j\phi_j(\boldsymbol{\nu}(k))-y_2(k)\right)^2\right)}{\partial\boldsymbol{\sigma}_j}\\ &= -\Gamma_{\boldsymbol{\sigma}_j}\frac{\partial\left(\frac{1}{2}\left(\sum_{j=1}^{h}\gamma_j\left(1-\frac{\|\boldsymbol{\nu}(k)-\boldsymbol{\mu}_j\|_2}{\boldsymbol{\sigma}_j^2}\right)e^{-\frac{\|\boldsymbol{\nu}(k)-\boldsymbol{\mu}_j\|_2}{\boldsymbol{\sigma}_j^2}}-y_2(k)\right)^2\right)}{\partial\boldsymbol{\sigma}_j}\\ &= -\Gamma_{\boldsymbol{\sigma}_j}\left(\sum_{j=1}^{h}\gamma_j\left(\frac{1}{\boldsymbol{\sigma}_j^5}e^{\frac{-\|\boldsymbol{\nu}(k)-\boldsymbol{\mu}_j\|_2}{\boldsymbol{\sigma}_j^2}}\left(4\boldsymbol{\sigma}_j^2\|\boldsymbol{\nu}(k)-\boldsymbol{\mu}_j\|_2-2\|\boldsymbol{\nu}(k)-\boldsymbol{\mu}_j\|_2^2\right)\right)\right)\tilde{y}_2(k)\end{aligned} \tag{5.6}$$

Using $\dot{x}(k) = (x(k+1)-x(k))/\Delta k$ with $\Delta k = 1$ yields a discrete formulation for the adaptation rules

$$\begin{aligned}\gamma_j(k+1) &= \gamma_j(k)-\Gamma_{\gamma_j}\left(\sum_{j=1}^{h}\phi_j(\boldsymbol{\nu}(k))\right)\tilde{y}_2(k)\\ \boldsymbol{\sigma}_j(k+1) &= \boldsymbol{\sigma}_j(k)-\Gamma_{\boldsymbol{\sigma}_j}\left(\sum_{j=1}^{h}\gamma_j\left(\frac{1}{\boldsymbol{\sigma}_j^5}e^{\frac{-\|\boldsymbol{\nu}(k)-\boldsymbol{\mu}_j\|_2}{\boldsymbol{\sigma}_j^2}}\left(4\boldsymbol{\sigma}_j^2\|\boldsymbol{\nu}(k)-\boldsymbol{\mu}_j\|_2-2\|\boldsymbol{\nu}(k)-\boldsymbol{\mu}_j\|_2^2\right)\right)\right)\tilde{y}_2(k)\end{aligned} \tag{5.7}$$

The delay vector $\boldsymbol{\nu}$ is variable, and its selection and adaptation is described in what follows.

5.2.1.1 Embedding of High-Rate Data

The embedding theorem [39, 40] is the fundamental principle underlying the variable input space formulation. The theorem, developed by Takens [39], states the phase-space of an unknown

autonomous system can be geometrically reconstructed using an observation y delayed by τ in an embedding dimension d forming a delay vector, ν

$$\boldsymbol{\nu}(k) = \left[\begin{array}{cccc} y_1(k), & y_1(k-\tau), & y_1(k-2\tau), & \cdots, \quad y_1(k-(d-1)\tau) \end{array} \right] \tag{5.8}$$

where $\boldsymbol{\nu} \in \Re^{dx1}$ and k is the discrete time step. From this formulation, there exists a one-to-one map between the phase-space produced by ν and the phase-space of the unknown system, provided $\boldsymbol{\nu}$ is constructed appropriately with the optimal parameters τ^* and d^*, yielding $\boldsymbol{\nu}^*$. Because such a map exists, the essential dynamics of the unknown system are preserved in $\boldsymbol{\nu}^*$. It is hypothesized that, because $\boldsymbol{\nu}*$ preserves the essential dynamics of the system, it can be used as a minimal input space to an estimator, producing more computationally efficient system representations. Originally developed for autonomous systems, the theorem has been extended to stationary systems with forcing [41], and applied to nonstationary high-rate systems through the calculation of the input spaces over stationary segments of data [12]. Here, the system of interest is nonstationary due to rapid changes in system configuration or from possible damage. Our solution is to vary $\boldsymbol{\nu}^*$ in real-time using $\tau^*(t)$ and $d^*(t)$. It follows that a challenge is in the selection of τ^* and d^*. It was demonstrated in literature that a combination of the mutual information (MI) test for τ^* and the false nearest neighbors (FNN) test for d^* yielded the most accurate results [42].

The MI test [43] is based on Shannon's information theory. The algorithm selects τ^* such that maximum level of information can be extracted between $y_1(k)$ and $y_1(k-\tau^*)$. Mathematically,

$$\mathrm{MI}(y_1(k), y_1(k-\tau)) = \sum_{y_1(k), y_1(k-\tau)} p(y_1(k), y_1(k-\tau)) \log \frac{p(y_1(k), y_1(k-\tau))}{p(y_1(k), p(y_1(k-\tau)))} \tag{5.9}$$

where $y_1(k)$ and $y_1(k-\tau)$ are discrete observations of the time series, $p(\cdot)$ denotes a probability, and $p(\cdot,\cdot)$ denotes a joint probability. The value τ^* is taken as the first local minimum of the mutual information function.

The false nearest neighbor (FNN) test [44] is used to calculate the optimal embedding dimension d^*. The FNN test calculates the Euclidean distances between the r^{th} neighboring points of a vector

for increasing dimensions. If the distance between neighboring points is greater than some threshold, the point is considered a false neighbor. Mathematically,

$$\left| \frac{R_{d+1}^2(k,r) - R_d^2(k,r)}{R_d^2(k,r)} \right| > R_{tol} \tag{5.10}$$

where R_{tol} is a user-defined threshold and $R_d^2(k,r)$ and $R_{d+1}^2(k,r)$ are the Euclidean distances between measurement $y(k)$ and its r^{th} nearest neighbor $y^{(r)}(k)$ for dimensions d and $d+1$. To increase accuracy, a second condition was added

$$\frac{R_{d+1}(k)}{R_A} > A_{tol} \tag{5.11}$$

with

$$R_A^2 = \frac{1}{n} \sum_{k=1}^{n} (y_1(k) - \bar{y}_1)^2 \tag{5.12}$$

where $\bar{y}_1$ is the mean of observations $\boldsymbol{y}_1$ and A_{tol} is a user-defined value. If both conditions are satisfied, the points are considered false neighbors. The value d^* is taken at the point when the percentage of FNN drops below an acceptable value.

5.2.1.2 Smooth Transition of the Input Space

The values for τ and d in constructing $\boldsymbol{\nu}$ are updated based on computed τ^* and d^*. In a previous study by the authors, it was demonstrated that rapid variation of the input space led to error spikes in the estimation [36]. To overcome this challenge, a slow transition of the input space was implemented. The slow transition allowed τ to vary by ± 10 and d to vary by ± 1 with the restrictions that τ remains positive and d does not drop below an embedding dimension of 2. For the smooth input space transition, we apply a sigmoid function $S(x)$ when adapting τ and allow d to vary by $d \pm 1$. New τ and d values are calculated every 10 iterations for a data history of 200 points. The 200 point data history is a sliding window of data used to calculate the input space for stationary segments of data. In real-time, τ would have units of seconds. In this study, we use

discrete time, which makes τ the corresponding number of past data points. A transition region of 10 points is selected to smooth the transition from the previous τ, τ_{old} to the new τ, τ_{new}, with

$$S(x) = \frac{1}{1 + e^{-x}} \tag{5.13}$$

where $x = -4 : 1 : 5$, and τ updated as follows:

$$\tau(k : k + 10) = S(x)(\tau_{\text{new}} - \tau_{\text{old}}) + \tau_{\text{old}} \tag{5.14}$$

where values for τ are rounded to the closest integer, and $\tau(k : k + 10)$ are the next ten τ values providing the smooth transition. Fig. 5.2 illustrates the smooth transitioning of τ. Since d has to be an integer, it varies by ± 1 with no further manipulation.

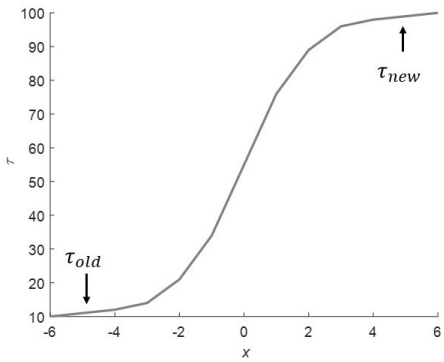

Figure 5.2: Smooth transition of τ.

5.2.2 Hybrid VIO

The VIO described above is a pure data-driven technique. While the system of interest is complex, it is possible that a certain level of physical knowledge be available. This gives raise to an opportunity to integrate such knowledge in the VIO, therefore creating a hybrid data-/model-driven observer. Here, this is done by using the data-driven VIO in parallel with a model-based observer constructed using the partial physical knowledge. It results that, in this configuration illustrated in Fig. 5.3, the VIO is used to estimate only the unmodeled dynamics, the difference between the

model and the system output measured by the sensor. The difference is further used to train the VIO. The estimates from the VIO and model are summed to produce the hybrid VIO's estimate.

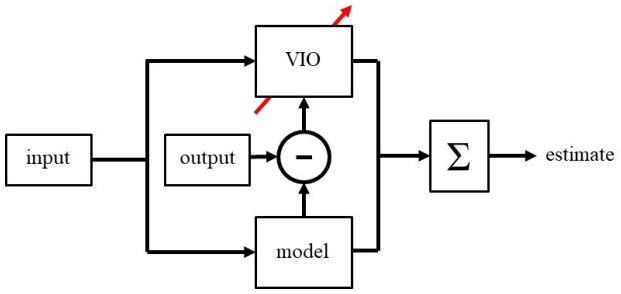

Figure 5.3: Block diagram of the hybrid data-/model-driven observer.

To study the effect of adding physical knowledge, the experimental data from the high-rate system of interest is modeled using a state-space representation

$$\begin{aligned} \dot{\mathbf{x}}(t) &= \mathbf{A}\mathbf{x}(t) + \mathbf{B}\mathbf{u}(t) + \mathbf{K}\mathbf{w}(t) \\ \mathbf{y}(t) &= \mathbf{C}\mathbf{x}(t) + \mathbf{D}\mathbf{u}(t) + \mathbf{w}(t) \end{aligned} \tag{5.15}$$

where $\mathbf{A}$, $\mathbf{B}$, $\mathbf{C}$, $\mathbf{D}$, and $\mathbf{K}$ are the state-space matrices and $\mathbf{u}(t)$, $\mathbf{y}(t)$, $\mathbf{w}(t)$, and $\mathbf{x}(t)$ are the input, output, disturbance, and state vectors. A six degrees-of-freedom (DOF) representation will be used to synthetically create partial physical knowledge from the system. The representation is constructed using the function `ssest` from the `MATLAB` system identification toolbox by feeding the time series of the input and output measurements and specifying the DOFs.

5.3 Numerical Simulations

Simulations were conducted on high-rate experimental data gathered from a mechanical shock test on an electronics unit. The various input space transition techniques of the VIO (fast, slow, and smooth transitions) are compared along with a traditional pre-optimized fixed input strategy as a base line. Simulations are also conducted on the hybrid data-/model-based observer.

5.3.1 Experimental Data

The experimental setup is shown in Fig. 5.4. An electronics unit (Fig. 5.4(c)) houses four circuit boards each equipped with a high-g Meggitt 72 accelerometers. These high-g accelerometers are capable of accurately measuring upward accelerations up to 120,000 g_n or 120 kg_n [45], where $1g_n = 9.81$ m/s^2 = 32.2 ft/s^2. The electronics in the unit are potted in high density polystyrene for shock survivability. The unit is securely held in a fixture (Fig. 5.4(b)) with a threaded lock ring. The fixture is bolted to an accelerated drop tower (Fig. 5.4(a)), which creates an impact condition. In this study, only the top (accel 2) and bottom (accel 1) accelerometer data sets are used.

Data was acquired using a Precision Filters signal conditioner coupled with a National Instruments data acquisition system. Precision Filter 28000 chassis with 28144A Quad-Channel Wide-band Transducer Conditioner is operated in constant voltage excitation mode with an anti-aliasing filter of 204.6 kHz. A National Instruments chassis with a PXI-6133 acquisition card sampling at 1 MSa/s is used for the acquisition of data.

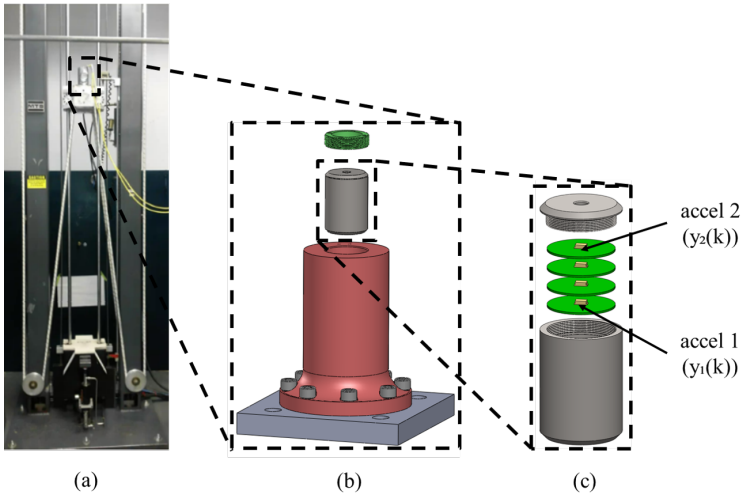

Figure 5.4: Experimental setup: a) MTS-66 drop tower; b) unit mounting fixture; and c) electronics unit.

This high-rate experiment contains many complexities. Noise is added to the data from the cable whip from the operation of the drop tower. The uncertainties are in the unknown high-rate

material response of the unit and boundary conditions. It is unsure whether or not the potting material stays bonded to the inner wall of the electronics unit. The precise input to the system from the drop tower impact is unknown. Only the response to the impact is measured. There are time-varying properties in the system response observed through back-to-back test results. Lastly, disturbances are created from sensor and system resonance from vibrations of threaded interfaces.

The experimental data is plotted in Figs. 5.5 and 5.6. The data is collected from five back-to-back tests of the same test condition. The entire high-rate dynamic event happens within 1 ms and produces deceleration responses ranging between -60 kg_n to above 50 kg_n. The overall response of the system is distinct from the similarities between the tests. However, from the zoomed in plots of both accel 1 (inputs) and accel 2 (outputs), there is evidence of time-varying properties. Fig. 5.5(c) and 5.6(d) shows the amplitudes increasing and the response delay varies as the test numbers increase.

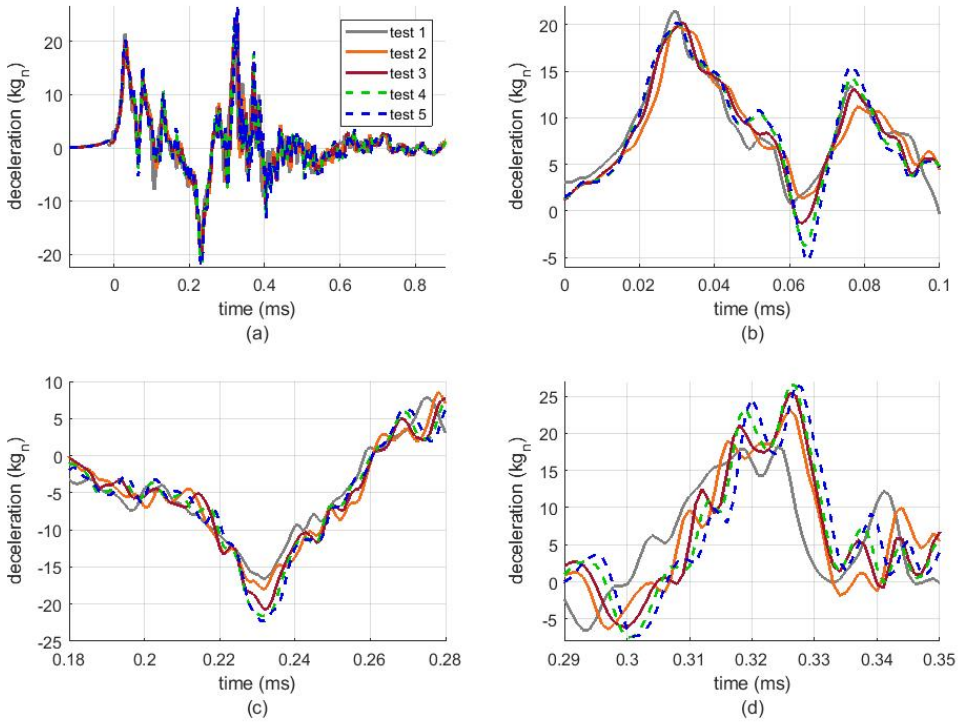

Figure 5.5: Time history of accel 1: a) over 1 ms; b) zoom on 0.11-0.21 ms; c) zoom on 0.3-0.4 ms; and d) zoom on 0.41-0.47 ms.

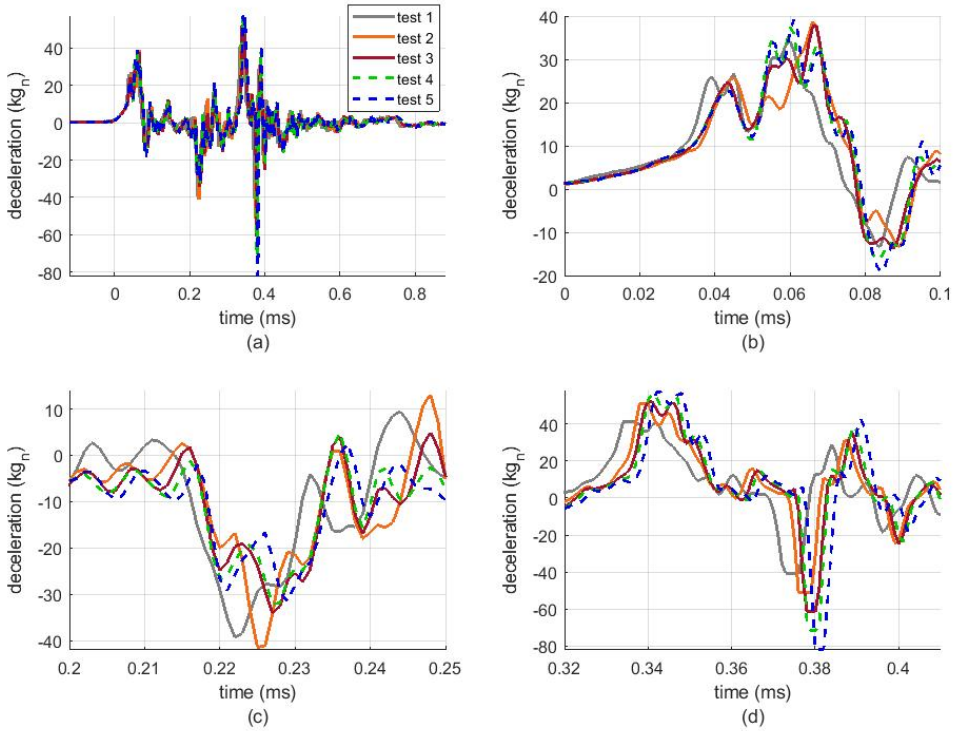

Figure 5.6: Time history of accel 2: a) over 1 ms; b) zoom on 0.14-0.22 ms; c) zoom on 0.32-0.37 ms; and d) zoom on 0.44-0.53 ms.

5.3.2 Simulation Results

5.3.2.1 Comparison of the VIO input space transition strategies

First, the performance of the different input space transitioning techniques is studied. Their performance is investigated relative to a traditional fixed input strategy. The fixed input space observer used the same WNN architecture as that of the VIO, but $\boldsymbol{\nu}$ is pre-optimized over the range $\tau = [1, 500]$ and $d = [2, 5]$ to obtained the smallest root mean square error (RMSE). The optimal fixed input observer used $\tau = 46$ and $d = 3$. Data from accel 1 (Fig. 2.1) is used as the input and accel 2 as the output to construct a representation.

The same parameters were used to simulate all observers for a direct comparison to determine which input space adaptation performs best. The parameter values are tabulated in Table 5.1.

Values Γ_γ and Γ_σ are respectively the learning rates for γ and σ, $\sigma(0)$ is the initial σ assigned to newly added nodes, R_{tol} and A_{tol} are threshold values suggested by Kennel [44] to determine if a neighbor is a false nearest neighbor, the FNN percentage is the upper percentage threshold in which to determine the proper embedding dimension, and the sliding window size is the history data size used to calculate the input space.

Table 5.1: Parameter values for all observer variations.

Parameter	Value
Γ_γ	0.02
Γ_σ	2.4
$\sigma(0)$	8
R_{tol}	15
A_{tol}	2
FNN percentage	10
Sliding window size	200

Fig. 5.7 is a plot of typical estimation time histories. The experimental data of accel 2 is represented by the gray solid line, the fixed input observer by the solid orange line, the fast transitioning VIO by the red solid line, the slow transitioning VIO by the green dashed line, and the smooth transitioning VIO by the blue dashed line. The overall estimations for the observers are plotted in Fig. 5.7(a), with zoomed portions in Fig. 5.7(b)-(d). Visual inspections of results show error spikes detected in the fixed observer, and in the fast and slow transitioning observers. The nonstationary nature of the high-rate experiment requires the input space to adapt to the dynamics. The proposed technique of using the sigmoid function to provide a smooth transition between input spaces shows superior to the previous versions based on the elimination of the error spikes. Another observable feature is that the data-driven methods did poorly in capturing the rise time of the initial pulse, but later was able to converge and produce good results.

Three more simulations were conducted to evaluate the robustness in the smooth transitioning VIO's choice of parameters. The second simulation used the same parameters as listed in Table 5.1, but with changing $\sigma(0)$ to 105% (5% increase) of the value listed in Table 5.1. Likewise, the third and forth simulations changed Γ_γ and Γ_σ to 105% of the value listed in Table 5.1, respectively.

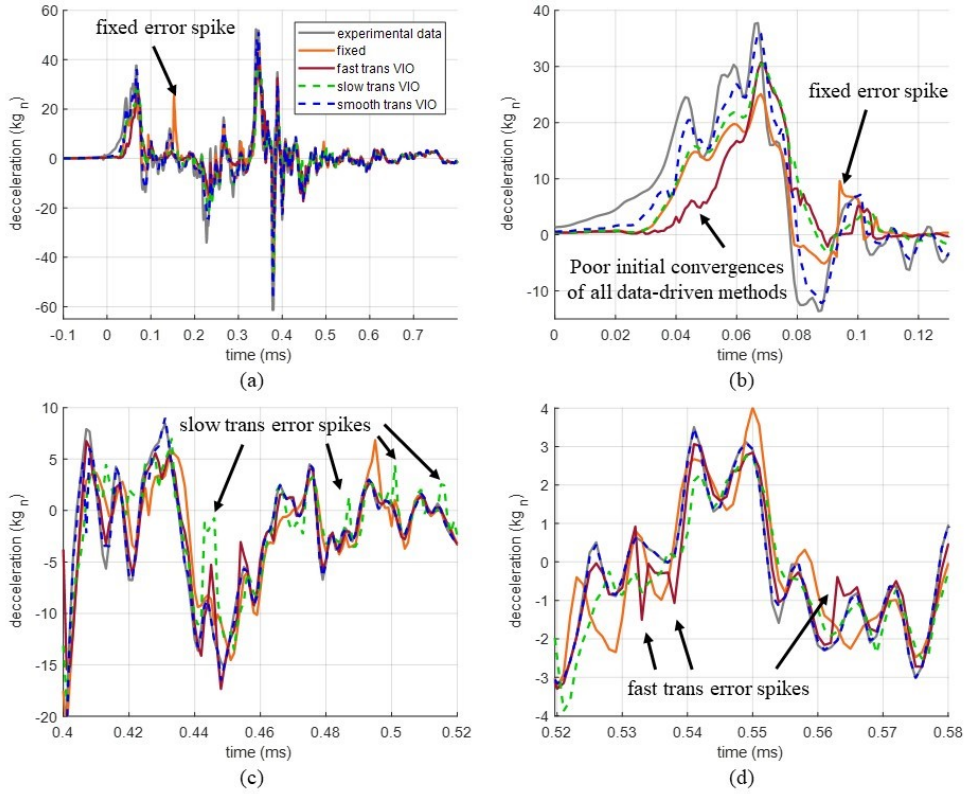

Figure 5.7: Estimation time histories: a) over 0.9 ms; b) zoom on 0-0.13 ms; c) zoom on 0.4-0.52 ms; d) zoom on 0.52-0.58 ms.

Performance of the observers are assessed through performance metrics listed in Table 5.2. A smaller number of nodes (J1) represents a more compact representation of the essential dynamics of the high-rate system, and thus a faster computation time. Note that the computation time itself is not part of this study. The RMSE of the entire trace (J2) gives an indication of overall fitting error. The RMSE of the first 0.13 ms (J3) is selected to compare the initial pulses of the estimations. The convergence time (J4) is determined from the start of the event (time = 0 ms) to when the absolute error falls and remains under 10% of the initial pulse value (3.7 kg_n). The error (J5-J6) is defined as the difference between the experimental data and the estimations produced by the different observers.

Fig. 5.8 compares the performance metrics (J1-J6) of the observers for the different simulations on radar plots. All the performance metrics are defined such that a smaller number exhibits a

Table 5.2: Performance metrics.

Metric	Description
J1	Number of nodes
J2	RMSE of entire trace (kg_n)
J3	RMSE of first 0.13 ms (kg_n)
J4	Convergence time (ms)
J5	Maximum absolute error (kg_n)
J6	Average absolute error (kg_n)

better performance. Results show that the smooth transitioning input space VIO outperforms all other observers over all performance metrics for every simulations, except for metric J4 under 105% of Γ_γ. A cross-comparison between simulations show that the wavelet neural network-based representation is relatively robust to the studied changes in parameters.

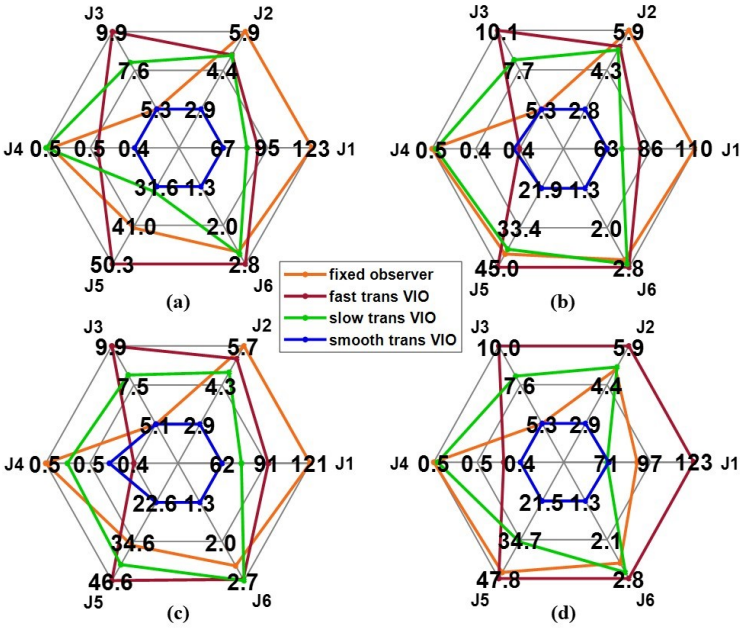

Figure 5.8: Radar plots of performance metrics J1-J6: a) simulation using parameters in Table 5.1; b) 105% of $\sigma(0)$; c) 105% of Γ_γ; d) 105% of Γ_σ.

Fig. 5.9 plots the evolution of τ and d for the smooth transitioning input space technique. The input space is constantly fluctuating throughout the simulation due to the nonstationary dynamics of the high-rate system. Remark that prior studies have shown the stabilization of these parameters

over stationary excitations (see [18], for instance). Early in the simulation at approximately 0.1 ms, there is a spike in τ attributable to a noisy low-amplitude excitation, after which τ drops and fluctuates at values under 50 points, later converging around 10 when the excitation becomes more stationary between 0.75-0.9 ms. The value for d increases from 2 when the excitation becomes more chaotic, oscillating between 2 and 3 for the majority of the excitation. It oscillates between 2 and 4 at the end of the simulation due to the higher level of chaos in the signal.

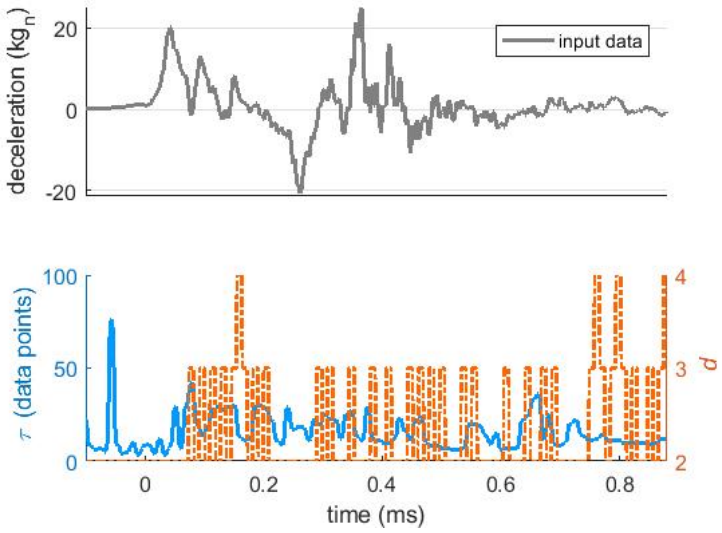

Figure 5.9: The evolution of τ and d.

The performance of the smooth transitioning VIO is further validated on a high impact velocity test using the same electronics unit (see Fig. 2.1). The unit was shot out of a smooth bore Howitzer impacting a concrete specimen. The estimation is compared with the same fixed input observer with $\tau = 46$ and $d = 3$. The same observer parameters listed in Table 1 were used. Fig. 5.10 plots the time histories.

The smooth transitioning VIO outperformed the fixed input observer in the initial convergence (Fig. 5.10 (b)), eliminated the error spikes (Fig. 5.10 (c)), and yielded a smaller overall RMSE of 1.38 kg_n compared with the fixed observers RMSE of 1.93 kg_n (a 29% improvement). The smooth transitioning VIO was capable of achieving better results, while using a more compact representation of 33 nodes compared with 38 nodes for the fixed observer.

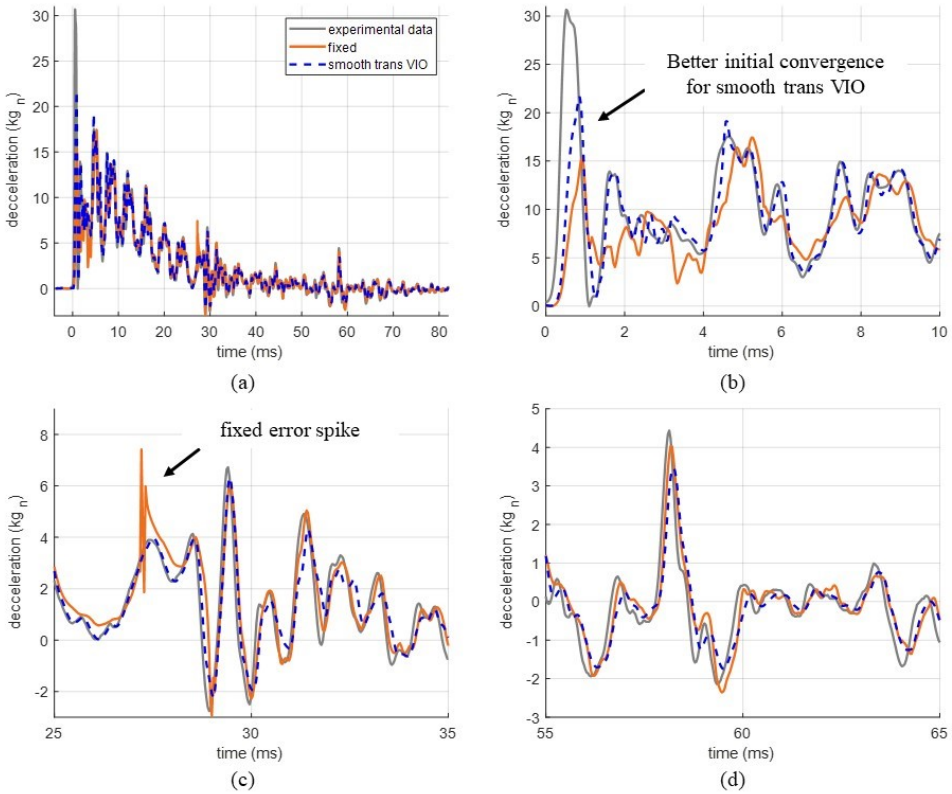

Figure 5.10: Estimation time histories: a) over 80 ms; b) zoom on 0-10 ms; c) zoom on 25-35 ms; d) zoom on 55-65 ms.

5.3.2.2 Model estimate of high-rate dynamics

The result for modeling high-rate dynamics with a six degrees-of-freedom representation is shown in Fig. 5.11. Fig. 5.11 shows that the modeling approach produces an acceptable fit with a better estimate than the pure data-driven observer early on, but that the high-rate complexities are not captured by the model.

5.3.2.3 Hybrid VIO study

Now, we study the exploitation of physical knowledge to create a hybrid VIO. Fig. 5.12 shows the comparison between the hybrid VIO estimate versus the smooth transitioning VIO (pure data-driven). It can be observed in Fig. 5.12(b) that better initial convergence is achieved through the addition of the physical knowledge. The hybrid VIO outperformed the smooth transitioning VIO

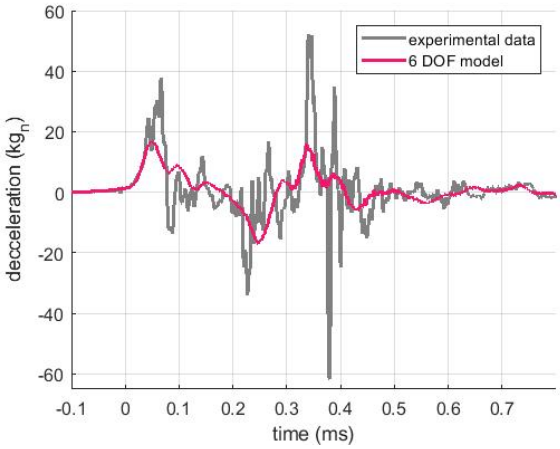

Figure 5.11: Modeled estimate of the high-rate experimental data.

using a fewer number of nodes and smaller overall RMSE, RMSE of the initial pulse, maximum absolute error, and average absolute error, and a similar convergence time as illustrated in the radar plot on Fig. 5.13.

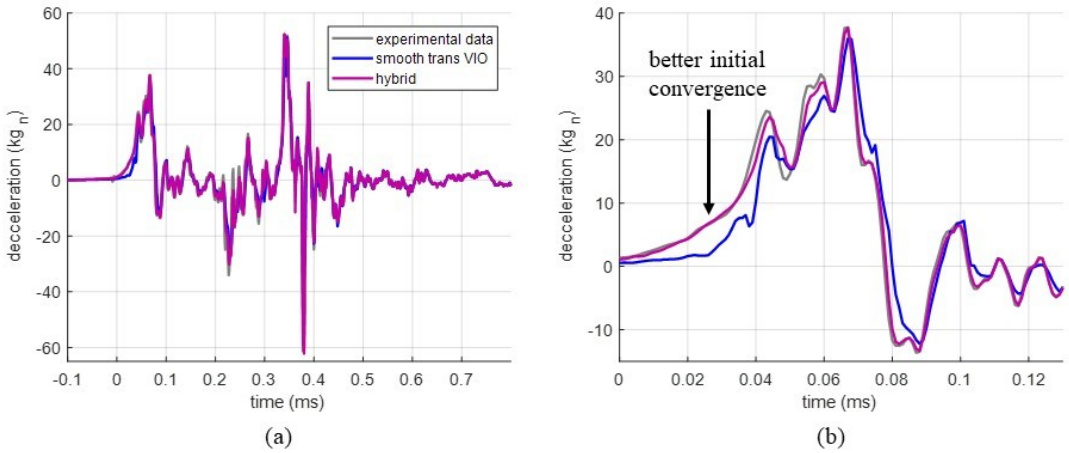

Figure 5.12: Hybrid observer vs. smooth transitioning VIO: a) over 0.9 ms; b) zoom on 0-0.13 ms.

The combination of the model and VIO is capable of producing a representation between accel1 (the input) and accel2 (the output) for test 3. Test 3 was chosen as the training data set to be consistent with previous VIO studies. Using the different tests shown in Figs 5.5 and 5.6, we verify the robustness of the representation. The inputs of tests 1, 2, 4, and 5 were used to estimate the outputs of the corresponding tests through a pre-trained hybrid VIO, using the data from test 3.

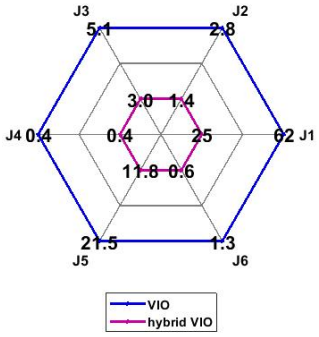

Figure 5.13: Radar plot of performance metrics J1-J6 comparing the hybrid VIO with the smooth transitioning VIO.

The absolute errors are plotted in Fig. 5.14. The majority of the errors fall below 20% of the initial pulse value with some peak errors occurring just under 15 kg_n. These maximum absolute errors are much smaller than those displayed in Fig. 5.8's J5 metric.

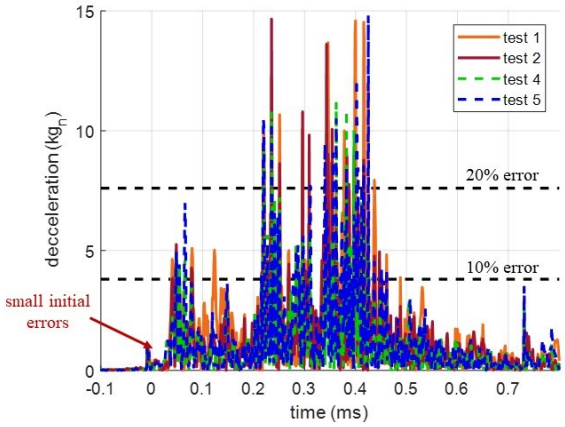

Figure 5.14: Absolute errors of estimates of tests 1, 2, 4, 5 using the learned representation from the hybrid observer.

5.4 Conclusion

State estimation of high-rate dynamic systems is challenging due to multiple system complexities such as noise, uncertainties, time-varying parameters/states, and disturbances. Examples of these systems include civil structures exposed to blast and aerial vehicles exposed to in-flight anomalies

such as contact with foreign objects. Adaptive observers showed to be an important tool for estimating complex systems. However due to the high-rate nature, adaptive observers would require faster convergence rates to be applicable.

As a potential solution, we presented a variable input observer (VIO), which optimized the use of past data. By doing so, we optimize the inputs to an estimator with the objective to enable faster convergence through an optimized representation. The variable input concept was based on the embedding theorem, whereas the input space is designed through a delay vector that preserves the essential dynamics of the system of interest. By allowing the delay vector to vary as sensor measurements become available, the embedding theorem is applied to complex nonstationary high-rate problems.

Three different input space transitioning strategies were studied. Those included fast, slow, and smooth transitioning input spaces. The fast transition applied no restriction on the input space adaptation allowing the time delay τ and embedding dimension d to vary as the calculations were made. The slow transitioning input space limited τ to vary by ± 10 and d by ± 1. The smooth transitioning input space applied a sigmoid function to τ to allow a smooth transition between input spaces.

Demonstrated in the simulations of high-rate experimental data, the smooth transitioning VIO outperformed all other methods, including a typical pre-optimzied fixed input space observer in terms of number of nodes, RMSE of the entire trace, RMSE of the first 0.13 ms, convergence time, maximum absolute error, and average absolute error. The error spikes are eliminated through the smooth transition and through a more accurate representation of the nonstationary high-rate system.

The training speed of the a neural network depends on many parameters such as the number of nodes used to build the representation, CPU speed, quality of the coding, etc. Through the smooth transitioning VIO, the number of nodes were minimized and provided more efficient training as observed through the faster convergence times. The real-time application of the VIO is currently under investigation.

A six degrees-of-freedom model of the high-rate data, representing a level of physical knowledge about the system, was added to the VIO to create a hybrid VIO. Results showed that the hybrid observer was capable of producing superior representations of the system compared with either a pure data- or model-driven observer. To validate the representation, inputs from consecutive tests were used to estimate the corresponding outputs. The study showed the majority of absolute errors were below the 20% of the initial pulse value. Furthermore, the peak absolute errors were much smaller than those seen using other observers.

Based on this study, the VIO has shown great promise for the use in nonstationary high-rate applications. The VIO, through the adaptive input space, is capable of sequentially learning chaotic representations improving the performance of an adaptive observer including its convergence time.

5.5 References

[1] J. Hong, S. Laflamme, J. Dodson, and B. Joyce, "Introduction to state estimation of high-rate system dynamics," *Sensors*, vol. 18, no. 217, pp. 1–16, 2018.

[2] R. Lowe, J. Dodson, and J. Foley, "Microsecond prognostics and health management," *IEEE Reliability Society Newsletter*, vol. 60, pp. 1–5, 2014.

[3] J. Connor and S. Laflamme, *Structural Motion Engineering*. Springer International, 2014.

[4] R. M. F. Oliveira, E. Ferreira, F. Oliveira, and S. Azevedo, "A study on the convergence of observer-based kinetics estimators in stirred tank bioreactors," *Korean Institute of Chemical Engineers*, vol. 6, no. 6, pp. 367–371, 1994.

[5] S. Mondal, G. Chakraborty, and K. Bhattacharyya, "Robust unknown input observer for nonlinear systems and its application to fault detection and isolation," *Journal of Dynamic Systems, Measurement, and Control*, vol. 130, no. 4, pp. 1–5, 2008.

[6] K. Stricker, L. Kocher, D. Van Alstine, and G. M. Shaver, "Input observer convergence and robustness: Application to compression ratio estimation," *Control Engineering Practice*, vol. 21, no. 4, pp. 565–582, 2013.

[7] Y. Wang, R. Rajamani, and D. M. Bevly, "Observer design for differentiable lipschitz nonlinear systems with time-varying parameters," in *53rd Annual Conference on Decision and Control (CDC)*, pp. 145–152, IEEE, 2014.

[8] B. K. Kim, W. K. Chung, and K. Ohba, "Design and performance tuning of sliding-mode controller for high-speed and high-accuracy positioning systems in disturbance observer framework," *IEEE Transactions on Industrial Electronics*, vol. 56, no. 10, pp. 3798–3809, 2009.

[9] M. Shahrokhi and M. Morari, "A discrete adaptive observer and identifier with arbitrarily fast rate of convergence," *IEEE Transactions on Automatic Control*, vol. 27, no. 2, pp. 506–509, 1982.

[10] K. Khayati and J. Zhu, "Adaptive observer for a large class of nonlinear systems with exponential convergence of parameter estimation," in *International Conference on Control, Decision and Information Technologies (CoDIT)*, pp. 100–105, IEEE, 2013.

[11] W. Byrski and J. Byrski, "On-line fast identification method and exact state observer for adaptive control of continuous system," in *11th World Congress on Intelligent Control and Automation (WCICA)*, pp. 4491–4497, IEEE, 2014.

[12] S. Laflamme, J. E. Slotine, and J. Connor, "Self-organizing input space for control of structures," *Smart Materials and Structures*, vol. 21, no. 11, p. 115015, 2012.

[13] G. Bowden, G. Dandy, and H. Maier, "Input determination for neural network models in water resources applications. Part 1–background and methodology," *Journal of Hydrology*, vol. 301, no. 1-4, pp. 75–92, 2005.

[14] A. da Silva, A. P., F. V., and R. Velasquez, "Input space to neural network based load forecasters," *Int. J. Forecast*, vol. 24, pp. 616–629, 2008.

[15] R. Sindelar and R. Babuska, "Input selection for nonlinear regression models," *Fuzzy Systems, IEEE Transactions on*, vol. 12, no. 5, pp. 688–696, 2004.

[16] X. Hong, R. Mitchell, S. Chen, C. Harris, K. Li, and G. Irwin, "Model selection approaches for non-linear system identification: a review," *International journal of systems science*, vol. 39, no. 10, pp. 925–946, 2008.

[17] L. Moniz, J. Nichols, C. Nichols, M. Seaver, S. Trickey, M. Todd, L. Pecora, and L. Virgin, "A multivariate, attractor-based approach to structural health monitoring," *Journal of Sound and Vibration*, vol. 283, no. 1-2, pp. 295–310, 2005.

[18] L. Cao, S. Laflamme, J. Hong, and J. Dodson, "Input space dependent controller for civil structures exposed to multi-hazard excitations," *Engineering Structures*, vol. 166, pp. 286–301, jul 2018.

[19] K. Worden, C. Farrar, J. Haywood, and T. M., "A review of nonlinear dynamics applications to structural health monitoring," *Structural Control Health Monitoring*, vol. 15, no. 4, pp. 540–567, 2008.

[20] V. Chinde, L. Cao, U. Vaidya, and S. Laflamme, "Damage detection on mesosurfaces using distributed sensor network and spectral diffusion maps," *Measurement Science and Technology*, vol. 27, no. 4, p. 045110, 2016.

[21] G. Liu, Z. Mao, M. Todd, and Z. Huang, "Damage assessment with state-space embedding strategy and singular value decomposition under stochastic excitation," *Structural Health Monitoring*, vol. 13, no. 2, pp. 131–142, 2014.

[22] D. Yu, J. Gomm, and D. Williams, "Neural model input selection for a mimo chemical process," *Eng. Appl. Artif. Intell.*, vol. 13, pp. 15–23, 2000.

[23] K. Li and J. Peng, "Neural input selectiona fast model-based approach," *Neurocomputing*, vol. 70, pp. 762–769, 2007.

[24] J. Tikka, "Simultaneous input variable and basis function selection for rbf networks," *Neurocomputing*, vol. 72, pp. 2649–2658, 2009.

[25] N. Kourentzes and S. Crone, "Frequency independent automatic input variable selection for neural networks for forecasting," *The 2010 Int. Joint Conf. on Neural Networks*, pp. 1–8, 2010.

[26] E. Monroig, K. Aihara, and Y. Fujino, "Modeling dynamics from only output data," *Physical Review E*, vol. 79, no. 5, p. 56208, 2009.

[27] L. Cao and S. Laflamme, "Real-time variable multidelay controller for multihazard mitigation," *Journal of Engineering Mechanics*, vol. 144, p. 04017174, feb 2018.

[28] J. Hong, S. Laflamme, and J. Dodson, "Study of input space for state estimation of high-rate dynamics," *Structural Control and Health Monitoring*, vol. 25, no. 6, p. e2159, 2018.

[29] L. Tarassento, *Guide to neural computing applications*. Butterworth-Heinemann, 1998.

[30] Q. Zhang and A. Benveniste, "Wavelet networks," *IEEE Transactions on Neural Networks*, vol. 3, pp. 889–898, 1992.

[31] B. Martin-del Brio and C. Serrano-Cinca, "Self-organizing neural networks for the analysis and representation of data: Some financial cases," *Neural Computing and Applications*, vol. 1, no. 3, pp. 193–206, 1993.

[32] M. Cannon and J. Slotine, "Space-frequency localized basis function networks for nonlinear system estimation and control," *Neurocomputing*, vol. 9, no. 3, pp. 293–342, 1995.

[33] J. Zhang and X. Xiao, "Predicting chaotic time series using recurrent neural network," *Chinese Physics Letters*, vol. 17, no. 2, p. 88, 2000.

[34] R. Frank, N. Ray, and S. Hunt, "Time series prediction and neural networks," *Journal of intelligent and robotic systems*, vol. 31, no. 1-3, pp. 91–103, 2001.

[35] J. Hong, S. Laflamme, and J. Dodson, "Variable input observer for structural health monitoring of high-rate systems," *Quantitative Nondestructive Evaluation*, vol. 43, p. 070003, 2016.

[36] J. Hong, L. Cao, S. Laflamme, and J. Dodson, "Robust variable input observer for structural health monitoring of systems experiencing harsh extreme environments," *11th International Workshop on Structural Health Monitoring*, vol. 11, pp. 1–8, 2017.

[37] T. Kohonen, "The self-organizing map," *Neurocomputing*, vol. 21, no. 1–3, pp. 1–6, 1998.

[38] S. Laflamme, J.-J. E. Slotine, and J. J. Connor, "Wavelet network for semi-active control," *Journal of Engineering Mechanics*, vol. 137, no. 7, pp. 462–474, 2011.

[39] F. Takens, "Detecting strange attractors in turbulence," *Dynamical systems and turbulence, Warwick 1980*, pp. 366–381, 1980.

[40] T. Sauer, J. Yorke, and M. Casdagli, "Embeddology," *J. Stat. Phys*, vol. 65, pp. 579–616, 1991.

[41] J. Stark, "Recursive prediction of chaotic time series," *Journal of Nonlinear Science*, vol. 3, no. 1, pp. 197–223, 1993.

[42] C. J. Cellucci, A. M. Albano, and P. E. Rapp, "Comparative study of embedding methods," *Phys. Rev. E*, vol. 67, no. 46, p. 066210, 2003.

[43] A. Fraser and H. Swinney, "Independent coordinates for strange attractors from mutual information," *Physical Review A*, vol. 33, no. 2, pp. 1134–1140, 1986.

[44] M. Kennel, R. Brown, and H. Abarbanel, "Determining embedding dimension for phase-space reconstruction using a geometrical construction," *Physical Review A*, vol. 45, no. 6, pp. 3403–3411, 1992.

[45] A. Beliveau, J. Hong, J. Coker, and N. Glikin, "COTS piezoresistive shock accelerometers performance evaluation," *Shock and Vibration Exchange*, vol. 83, pp. 1–10, 2012.

CHAPTER 6. TRANSVERSE VIBRATION OF CLAMPED-PINNED-FREE BEAM WITH MASS AT FREE END

J. Hong, J. Dodson, S. Laflamme, and A. Downey

Abstract

Engineering systems undergoing extreme and harsh environments can often times experience rapid damaging effects. In order to minimize loss of economic investment and human lives, structural health monitoring (SHM) of these high-rate systems is being researched. An experimental test bed has been developed to validate SHM methods in a controllable and repeatable laboratory environment. This study applies the Euler-Bernoulli beam theory to this test bed to develop analytical solutions of the system. The transverse vibration of a clamped-pinned-free beam with a point mass at the free end is discussed in detail. Results are derived for varying pin locations and mass values. Eigenvalue plots of the first five modes are presented along with their respective mode shapes. The theoretical calculations are experimentally validated and discussed.

6.1 Introduction

High-rate dynamics are defined as events having amplitudes greater than 100 g over durations less than 100 ms [1]. Some examples of high-rate systems may include civil structures exposed to blast, passenger vehicles experiencing collisions, and aerial or spacecraft vehicles subjected to ballistic impacts. Such systems have the potential to experience rapid changes in mechanical configuration through damage. Economic investments and lives could be saved if fast detection of parameter changes can be accurately quantified [2]. A variable input observer has been studied by the authors as a potential solution to increasing convergence times through richer inputs [3]. However, there is a need to validate high-rate structural health monitoring (SHM) methods [4].

An experimental test bed has been designed and built to test and validate SHM methods for systems experiencing high-rate dynamics. The development of an experimental test bed is critical, because the experimentation on real-life high-rate systems would be complex, difficulty to verify, and potentially very costly. This test bed design incorporates a cantilever beam with a roller that restrains the displacement in the vertical direction and is allowed to move freely along the length of the beam. Additionally, the mass at the free end of the beam can be dropped through the de-energizing of the electromagnet that detaches the mass from the beam. The roller is a moving cart that provides a changing boundary condition, while the mass drop provides a sudden change in mechanical configuration. This system is easily controllable and repeatable in a laboratory setting.

To develop analytical solutions for this beam structure, the Euler-Bernoulli beam theory is applied. The system is modeled as clamped-pinned-free with a point mass at free end. There is no mention of this beam configuration in the book authored by Blevins [5]. Previously and to the best knowledge of the authors, only the clamped-pinned-free [6] (no mass) and the clamped-free with mass at free end [7] (no pin) have been studied.

Using beam theory, section 6.2 derives the transcendental equation. A generalized form is presented that is applicable to any pin location and any mass value. Derived results are verified through comparison between well-known cases in literature. Section 6.3 calculates the eigenvalues for normalized pinned location for various mass ratios. Section 6.4 calculates the mode shapes

for several different pinned locations, while section 6.5 compares the results from the theoretical calculations to experimental data.

6.2 Frequency Calculations

The transverse vibrations of a slender clamped-pinned-free beam with a mass at free end of interest is shown in Fig. 6.1. The governing equation for the beam using Euler-Bernoulli's beam theory [8] can be written

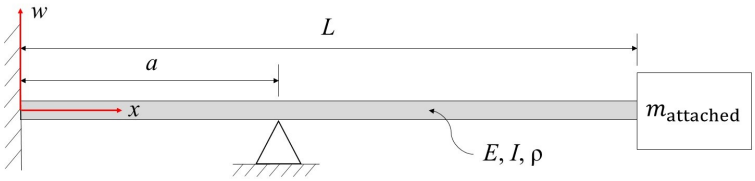

Figure 6.1: Schematic of a clamped-pinned-free beam with mass at free end.

$$\rho A \frac{\partial^2 w}{\partial t^2} + EI \frac{\partial^4 w}{\partial x^4} = 0 \tag{6.1}$$

where E is the Young's modulus, I the cross-sectional moment of inertia, w the vertical deflection, x the axial coordinate, ρ the density of the beam, A the cross-sectional area, and t time. Eq. (6.1) can be solved assuming a separation-of-variables solution in the standard form

$$w(x,t) = X(x)T(t) \tag{6.2}$$

where X is the spatial solution and T is the temporal solution. The spatial solution for a two-span beam then is expressed

$$X(x) = \begin{cases} X_1(x), & 0 \le x \le a \\ X_2(x), & a \le x \le L \end{cases} \tag{6.3}$$

The sub-functions in eq 6.3 can be written as the following general solutions

$$X_1(x) = a_1 \sin(\beta x) + a_2 \cos(\beta x) + a_3 \sinh(\beta x) + a_4 \cosh(\beta x) \tag{6.4}$$

$$X_2(x) = b_1 \sin(\beta x) + b_2 \cos(\beta x) + b_3 \sinh(\beta x) + b_4 \cosh(\beta x) \tag{6.5}$$

where β is the beam vibration eigenvalue. Parameter β and seven of the eight coefficients can be solved by applying the boundary conditions of the system. For the clamped-pinned-free, the displacement and slope at the clamped end are zero [7]

$$X_1(0) = 0 \tag{6.6}$$

$$\frac{dX_1(0)}{dx} = 0 \tag{6.7}$$

while at the free end, the bending moment and the shear vanish such that

$$\frac{d^2X_2(L)}{dx^2} = 0 \tag{6.8}$$

$$\frac{d^3X_2(L)}{dx^3} = m_{\text{attached}} \frac{d^2T_2(L)}{dt^2} \tag{6.9}$$

where m_{attached} is the mass attached to the beam at the free end. In addition to these four boundary conditions, four more boundary conditions (displacement and rotation) are found at the pin location a:

$$X_1(a) = 0 \tag{6.10}$$

$$X_2(a) = 0 \tag{6.11}$$

$$\frac{dX_1(a)}{dx} = \frac{dX_2(a)}{dx} \tag{6.12}$$

$$\frac{d^2X_1(a)}{dx^2} = \frac{d^2X_2(a)}{dx^2} \tag{6.13}$$

Substituting the first transverse displacement (Eq. (6.4)) into the clamped boundary condition (Eqs. (6.6) and (6.7)) gives

$$a_2 + a_4 = 0 \tag{6.14}$$

$$a_1 + a_3 = 0 \tag{6.15}$$

Substituting the second transverse displacement (Eq. (6.5)) into the free end boundary condition (Eq. (6.8)) yields:

$$-b_1 \sin(\beta L) - b_2 \cos(\beta L) + b_3 \sinh(\beta L) + b_4 \cosh(\beta L) = 0 \tag{6.16}$$

Additionally, inserting the second transverse displacement (Eq. (6.5)) into Eq. 6.1 and applying the boundary condition at the free end (Eq. (6.9)) results in:

$$\begin{aligned} &b_1(-\cos(\beta L) + \beta L \frac{m_{\text{attached}}}{m_{\text{beam}}} \sin(\beta L)) + b_2(\sin(\beta L) + \beta L \frac{m_{\text{attached}}}{m_{\text{beam}}} \cos(\beta L)) \\ &+b_3(\cosh(\beta L) + \beta L \frac{m_{\text{attached}}}{m_{\text{beam}}} \sinh(\beta L)) + b_4(\sinh(\beta L) + \beta L \frac{m_{\text{attached}}}{m_{\text{beam}}} \cosh(\beta L)) = 0 \end{aligned} \tag{6.17}$$

where m_{beam} is the mass of the beam.

Substituting the first transverse displacement (Eq. (6.4)) into the pinned boundary condition (Eqs. (6.10) and (6.11)) results in:

$$a_1 \sin(\beta L \frac{a}{L}) + a_2 \cos(\beta L \frac{a}{L}) + a_3 \sinh(\beta L \frac{a}{L}) + a_4 \cosh(\beta L \frac{a}{L}) = 0 \tag{6.18}$$

and

$$b_1 \sin(\beta L \frac{a}{L}) + b_2 \cos(\beta L \frac{a}{L}) + b_3 \sinh(\beta L \frac{a}{L}) + b_4 \cosh(\beta L \frac{a}{L}) = 0 \tag{6.19}$$

After, substituting the second transverse displacement (Eq. (6.5)) into the boundary conditions defined by Eqs. (6.12) and (6.13) provides the following expressions:

$$\begin{aligned} &a_1 \cos(\beta L \frac{a}{L}) - a_2 \sin(\beta L \frac{a}{L}) + a_3 \cosh(\beta L \frac{a}{L}) + a_4 \sinh(\beta L \frac{a}{L}) \\ &-b_1 \cos(\beta L \frac{a}{L}) + b_2 \sin(\beta L \frac{a}{L}) - b_3 \cosh(\beta L \frac{a}{L}) - b_4 \sinh(\beta L \frac{a}{L}) = 0 \end{aligned} \tag{6.20}$$

$$-a_1\sin(\beta L\frac{a}{L})-a_2\cos(\beta L\frac{a}{L})+a_3\sinh(\beta L\frac{a}{L})+a_4\cosh(\beta L\frac{a}{L})$$
$$+b_1\sin(\beta L\frac{a}{L})+b_2\cos(\beta L\frac{a}{L})-b_3\sinh(\beta L\frac{a}{L})-b_4\cosh(\beta L\frac{a}{L})=0 \tag{6.21}$$

Aggregating Eqs. (6.14)-(6.21) into an $8x8$ matrix and solving for the determinant leads to the transcendental equation expressed

$$4\cos(\beta L(\frac{a}{L}-1))\sinh(\beta L(\frac{a}{L}-1))-4\cosh(\beta L(\frac{a}{L}-1))\sin(\beta L(\frac{a}{L}-1))$$
$$+2\cos(\beta L(2\frac{a}{L}-1))\sinh(\beta L)-2\cosh(\beta L(2\frac{a}{L}-1))\sin(\beta L)$$
$$+4\cos(\frac{a}{L}\beta L)\sinh(\frac{a}{L}\beta L)-4\cosh(\frac{a}{L}\beta L)\sin(\frac{a}{L}\beta L)$$
$$+2\cos(\beta L)\sinh(\beta L)-2\cosh(\beta L)\sin(\beta L)+8\beta L\frac{m_{\text{attached}}}{m_{\text{beam}}}\sin(\beta L(\frac{a}{L}-1))\sinh(\beta L(\frac{a}{L}-1))$$
$$+2\beta L\frac{m_{\text{attached}}}{m_{\text{beam}}}\cos(\beta L(2\frac{a}{L}-1))\cosh(\beta L)-2\beta L\frac{m_{\text{attached}}}{m_{\text{beam}}}\cosh(\beta L(2\frac{a}{L}-1))\cos(\beta L)$$
$$+2\beta L\frac{m_{\text{attached}}}{m_{\text{beam}}}\sin(\beta L(2\frac{a}{L}-1))\sinh(\beta L)+2\beta L\frac{m_{\text{attached}}}{m_{\text{beam}}}\sinh(\beta L(2\frac{a}{L}-1))\sin(\beta L)$$
$$-4\beta L\frac{m_{\text{attached}}}{m_{\text{beam}}}\sin(\beta L)\sinh(\beta L)=0 \tag{6.22}$$

where the natural frequencies (in Hz) are given by

$$f_n=\frac{(\beta_n L)^2}{2\pi L^2}\sqrt{\frac{EI}{\rho A}} \tag{6.23}$$

To verify Eq. (6.22), the first five natural frequencies were calculated for three well-known cases:

- Case 1: Clamped-free [9]: $\frac{a}{L}=\frac{m_{\text{attached}}}{m_{\text{beam}}}=0$
- Case 2: Clamped-free with mass at free end [7]: $\frac{a}{L}=0$
- Case 3: Clamped-pinned-free [6]: $\frac{m_{\text{attached}}}{m_{\text{beam}}}=0$

The results are tabulated in Tables 6.1-6.3. The frequencies of the first five modes (β_1-β_5) are compared between what is found in literature against the results from Eq. (6.22) (proposed model). The small differences are due to rounding errors of the beam vibration eigenvalues β, which cause large changes in the calculated frequency ($f_n \propto \beta_n^2$). The precision for β in this paper is ± 0.0002.

Table 6.1: Comparison of analytical results: Clamped-free (Case 1)

Mode	Literature [9] (Hz)	Proposed model (Hz)	Difference (%)
1	19.64	19.63	0.051
2	123.07	123.02	0.041
3	344.64	344.45	0.055
4	675.31	674.97	0.050
5	1116.33	1115.79	0.048

Table 6.2: Comparison of analytical results: Clamped-free with mass ($\frac{m_{\text{attached}}}{m_{\text{beam}}} = 0.2$) (Case 2)

Mode	Literature [7] (Hz)	Proposed model (Hz)	Difference (%)
1	14.56	14.58	0.14
2	101.47	101.64	0.17
3	298.59	299.00	0.14
4	603.06	604.02	0.16
5	1017.07	1018.48	0.14

Table 6.3: Comparison of analytical results: Clamped-pinned-free (Pin at $a = 200$ mm) (Case 3)

Mode	Literature [6] (Hz)	Proposed model (Hz)	Difference (%)
1	41.70	41.59	0.26
2	279.25	278.46	0.28
3	635.80	635.19	0.10
4	899.94	897.69	0.25
5	1650.85	1646.48	0.26

6.3 Calculations of Eigenvalues

The beam vibration eigenvalues are calculated in terms of βL for different mass ratios, $\frac{m_{\text{attached}}}{m_{\text{beam}}}$. The eigenvalues are plotted as a function of the normalized pinned location, $\frac{a}{L}$ in Figs. 6.2-6.6. Note, the βL values corresponding to $\frac{a}{L} = 0$ is equivalent to the clamped-free system with a mass at the free.

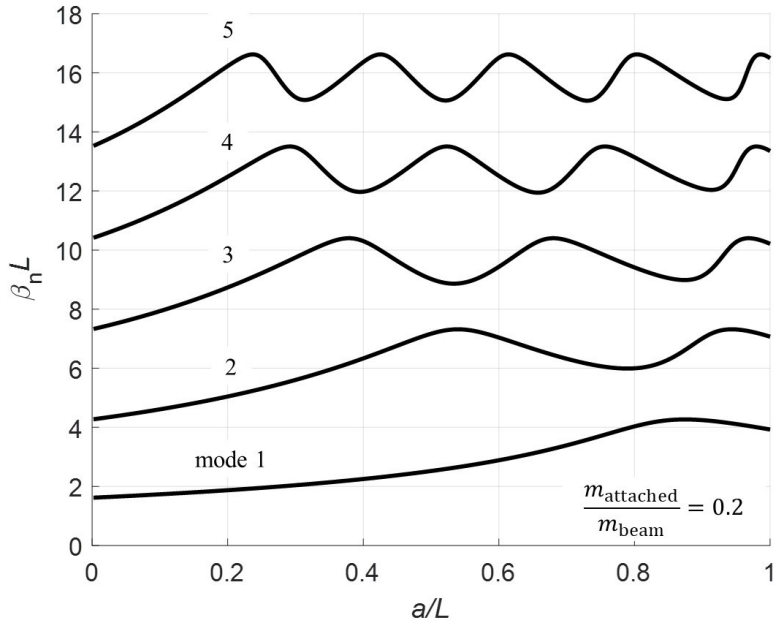

Figure 6.2: Eigenvalues of first 5 modes, $\frac{m_{\text{attached}}}{m_{\text{beam}}} = 0.2$

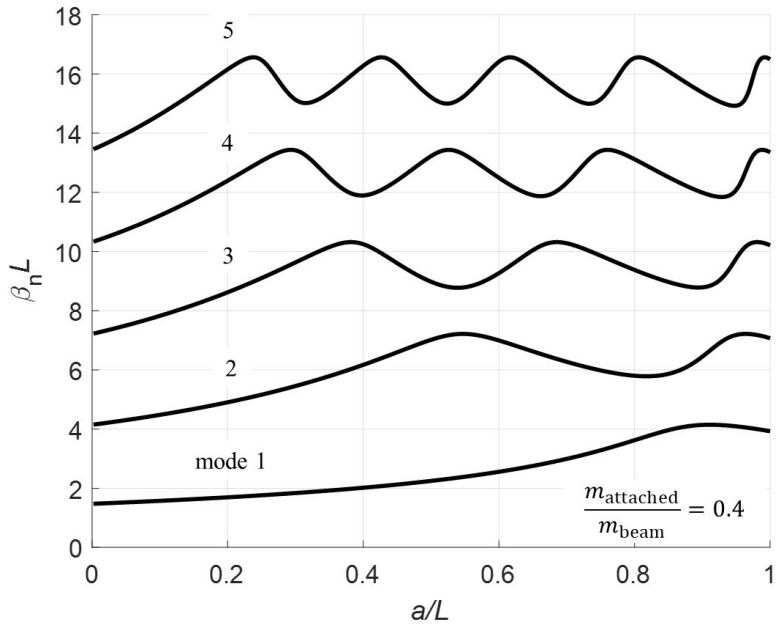

Figure 6.3: Eigenvalues of first 5 modes, $\frac{m_{\text{attached}}}{m_{\text{beam}}} = 0.4$

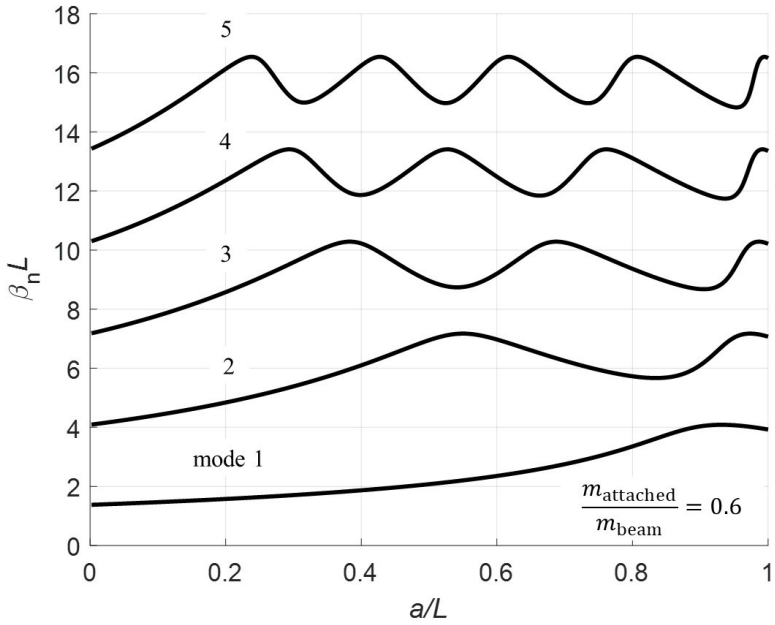

Figure 6.4: Eigenvalues of first 5 modes, $\frac{m_{\text{attached}}}{m_{\text{beam}}} = 0.6$

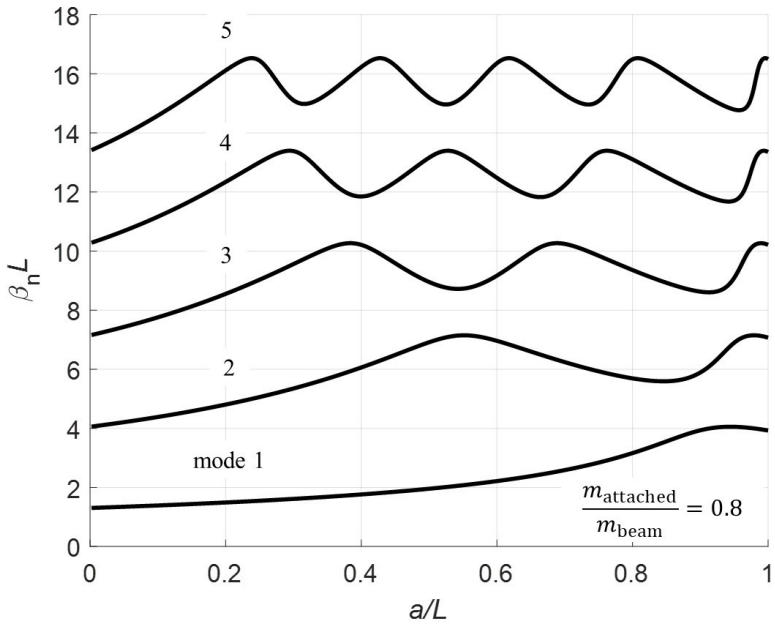

Figure 6.5: Eigenvalues of first 5 modes, $\frac{m_{\text{attached}}}{m_{\text{beam}}} = 0.8$

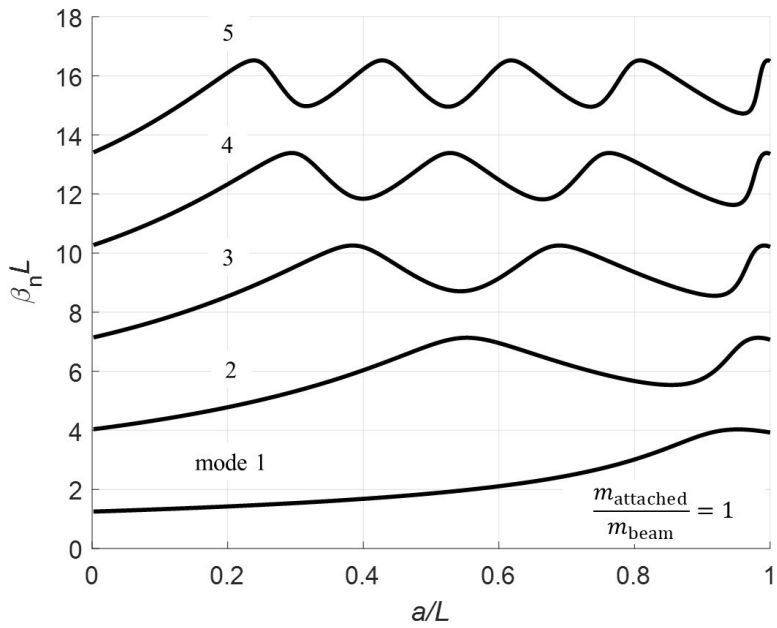

Figure 6.6: Eigenvalues of first 5 modes, $\frac{m_{\text{attached}}}{m_{\text{beam}}} = 1$

6.4 Mode Shapes

The mode shapes are calculated for the two different sections of the beam corresponding to the clamped-pinned and pinned-free sections. To calculate the mode shapes, the boundary condition (Eqs. (6.6)-(6.13)) are used to find a relationship between the coefficients. The method used here consists of solving all coefficients in terms of a_4. Note, there are not enough equations to determine a unique solution for each coefficient. The solutions for the a coefficients are

$$a_1 = -a_3 \tag{6.24}$$

$$a_2 = -a_4 \tag{6.25}$$

$$a_3 = \frac{\cos(\beta L\frac{a}{L}) - \cosh(\beta L\frac{a}{L})}{(\sinh(\beta L\frac{a}{L}) - \sin(\beta L\frac{a}{L})} a_4 \tag{6.26}$$

and for the b coefficients

$$b_1 = -b_2 \cot(\beta L) + b_3 \frac{\sinh(\beta L)}{\sin(\beta L)} + b_4 \frac{\cosh(\beta L)}{\sin(\beta L)} \tag{6.27}$$

$$b_2 = b_3 \frac{z_1}{z_3} + b_4 \frac{z_2}{z_3} \tag{6.28}$$

$$b_3 = \frac{\frac{z_2 z_4}{z_3} + z_6}{\frac{z_1 z_4}{z_3} + z_5} \tag{6.29}$$

where

$$z_1 = \frac{\sinh(\beta L)}{\sin(\beta L)}(\cos(\beta L) + \beta L \frac{m_{\text{attached}}}{m_{\text{beam}}} \sin(\beta L)) - (\cosh(\beta L) + \beta L \frac{m_{\text{attached}}}{m_{\text{beam}}} \sinh(\beta L)) \tag{6.30}$$

$$z_2 = \frac{\cosh(\beta L)}{\sin(\beta L)}(\cos(\beta L) + \beta L \frac{m_{\text{attached}}}{m_{\text{beam}}} \sin(\beta L)) - (\sinh(\beta L) + \beta L \frac{m_{\text{attached}}}{m_{\text{beam}}} \cosh(\beta L)) \tag{6.31}$$

$$z_3 = \cot(\beta L)(\cos(\beta L) + \beta L \frac{m_{\text{attached}}}{m_{\text{beam}}} \sin(\beta L)) + (\sin(\beta L) + \beta L \frac{m_{\text{attached}}}{m_{\text{beam}}} \cos(\beta L)) \tag{6.32}$$

$$z_4 = \cos(\beta L \frac{a}{L}) - \cot(\beta L) \sin(\beta L \frac{a}{L}) \tag{6.33}$$

$$z_5 = \frac{\sinh(\beta L)}{\sin(\beta L)} \sin(\beta L \frac{a}{L}) + \sinh(\beta L \frac{a}{L}) \tag{6.34}$$

$$z_6 = \frac{\cosh(\beta L)}{\sin(\beta L)} \sin(\beta L \frac{a}{L}) + \cosh(\beta L \frac{a}{L}) \tag{6.35}$$

Substituting the equations for the coefficients (Eqs. (6.24)-(6.35)) into the boundary condition from Eq. (6.12), a relationship between $a4$ and $b4$ is obtained. For brevity, this expression is not presented here. The mode shapes are determined for the multi-span beam by substituting all coefficient expressions in terms of $a4$ into Eq. (6.3).

Normalizing at $a_4 = 1$, the first five mode shapes for the clamped-pinned-free beam with a mass at the free end are plotted in Figs. 6.7-6.10 for a = 100, 200, 300, and 400 mm with $\frac{m_{\text{attached}}}{m_{\text{beam}}} = 0.2$. The red triangle on the plots denotes the pin location.

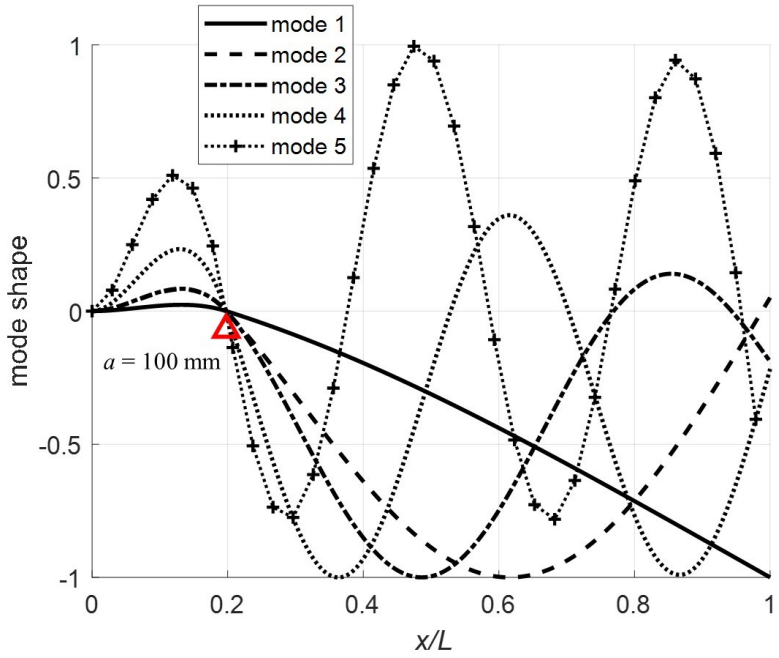

Figure 6.7: Mode shapes for pinned at $a = 100$ mm and $\frac{m_{\text{attached}}}{m_{\text{beam}}} = 0.2$

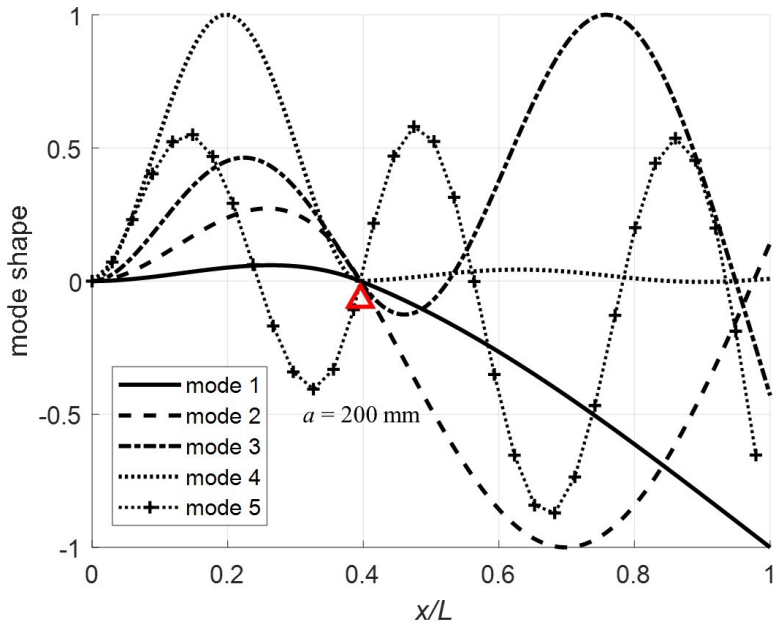

Figure 6.8: Mode shapes for pinned at $a = 200$ mm and $\frac{m_{\text{attached}}}{m_{\text{beam}}} = 0.2$

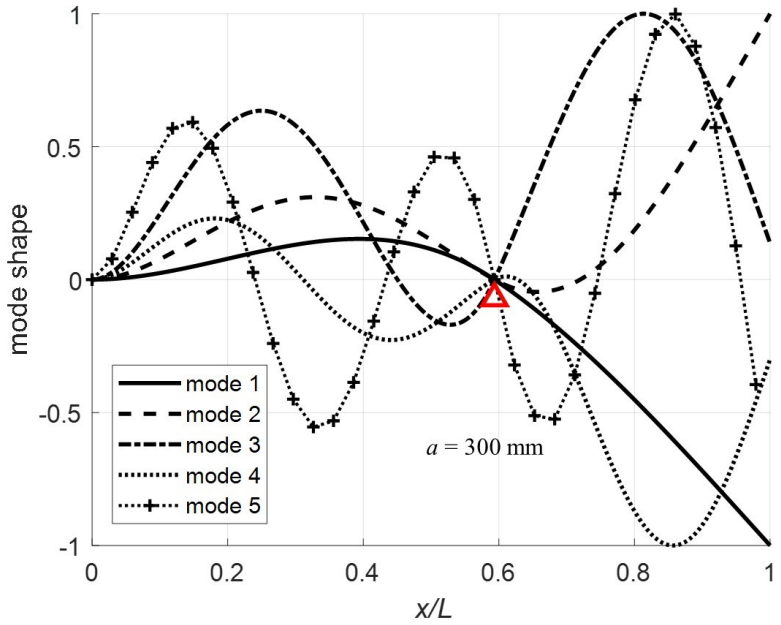

Figure 6.9: Mode shapes for pinned at $a = 300$ mm and $\frac{m_{\text{attached}}}{m_{\text{beam}}} = 0.2$

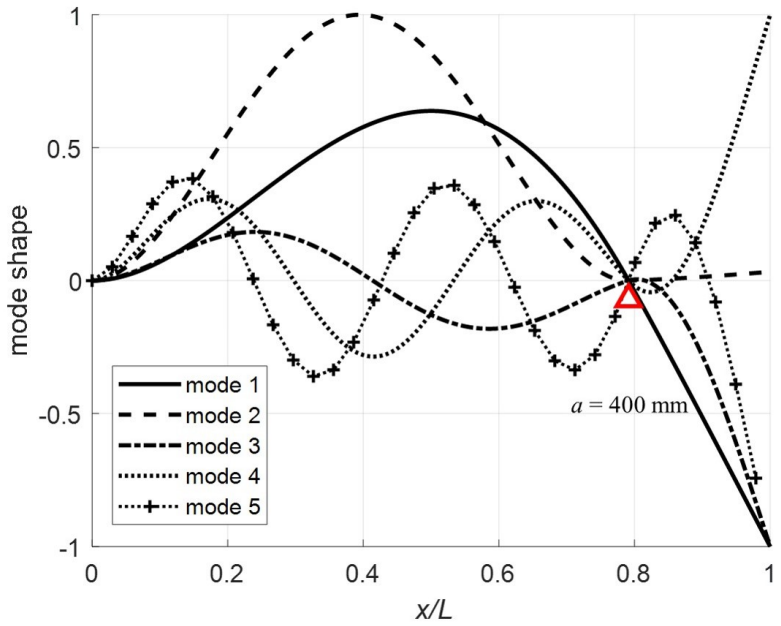

Figure 6.10: Mode shapes for pinned at $a = 400$ mm and $\frac{m_{\text{attached}}}{m_{\text{beam}}} = 0.2$

6.5 Experimental Validation

In this section, the theoretical results are compared with experimental data. The experimental setup is illustrated in Fig. 6.11. A cart with rollers is used as a moving pin along the beam. Accelerometers are attached at locations 300 mm and 400 mm. The mass of the accelerometers is assumed to have a negligible effect. Each accelerometer weighs 1.7 gm, not including cables, which is 0.2% of the weight of the beam. At the free end, an electromagnet is used to simulate the mass. The specifications of the experiment are listed in Table 6.4.

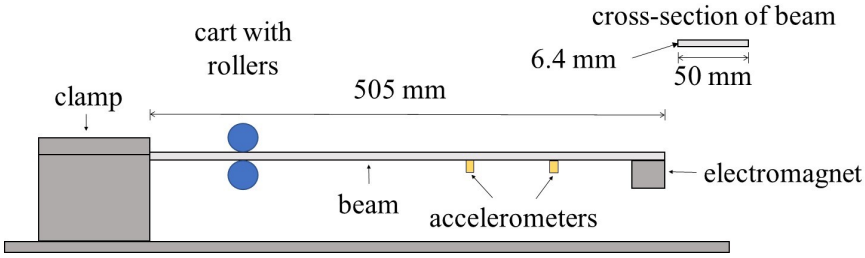

Figure 6.11: Illustration of the experimental setup

Table 6.4: Specifications of the experimental setup

Parameter	Value
L	505 mm
base	50 mm
height	6.4 mm
ρ	7970 kg/m^3
E	190 GPa
m_{attached}	0.259 Kg

The accelerometers are single axis PCB 353B17. They are connected to a NI-9234 IEPE analog input module seated in an NI cDAQ-9172 chassis. A PCB 086C01 modal hammer with a white ABS

plastic tip is used to excite the beam at 300 mm. Five tests under each condition are conducted and averaged in the frequency domain to generate frequency response functions (FRFs) using the H_v algorithm [10]. The FRFs for the different tests are plotted in Figs. 6.12-6.15. The vertical red dashed lines represent the theoretical modes computed from the proposed model. To better understand the differences, the modes are extracted and tabulated in Tables 6.5-6.8.

For every test conditions, modes 4 and 5 have larger differences. Three possible explanations are 1) the electromagnet vibrates separate from the beam, 2) the beam vibrates within the rollers, and 3) the rotational inertia from a large mass at the end of a long beam impacts the higher frequencies. In Figs. 6.13 and 6.15, the coherence for mode 5 drops significantly such that it cannot be said with certainty that the frequencies are correct. Percent difference is used to quantify how different the theoretical frequencies are from the experimental. All frequencies fall below 20% difference with the exception of mode 4 in Table 6.5.

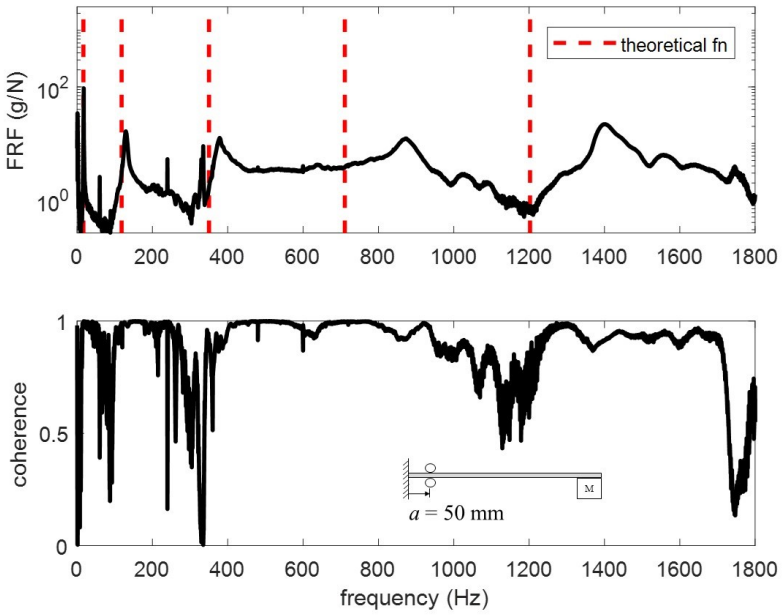

Figure 6.12: FRF for pinned at $a = 50$ mm and $\frac{m_{\text{attached}}}{m_{\text{beam}}} = 0.2$

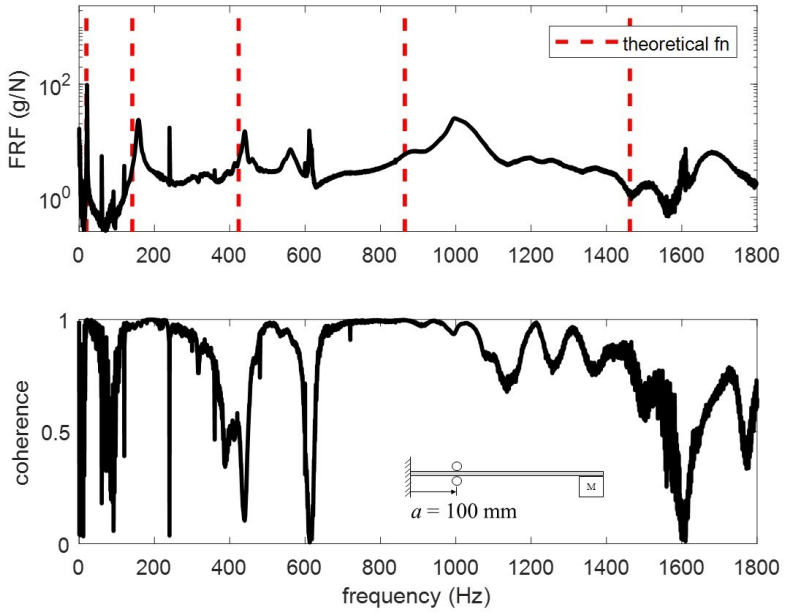

Figure 6.13: FRF for pinned at $a = 100$ mm and $\frac{m_{\text{attached}}}{m_{\text{beam}}} = 0.2$

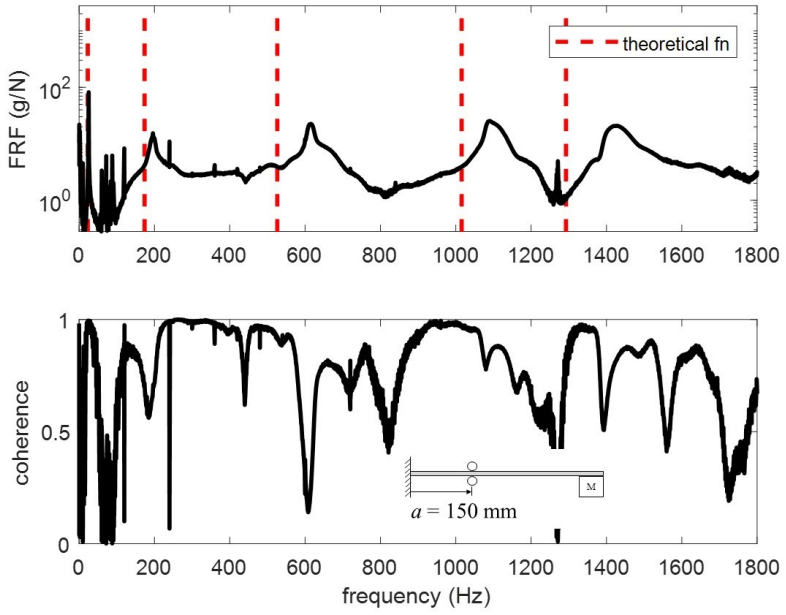

Figure 6.14: FRF for pinned at $a = 150$ mm and $\frac{m_{\text{attached}}}{m_{\text{beam}}} = 0.2$

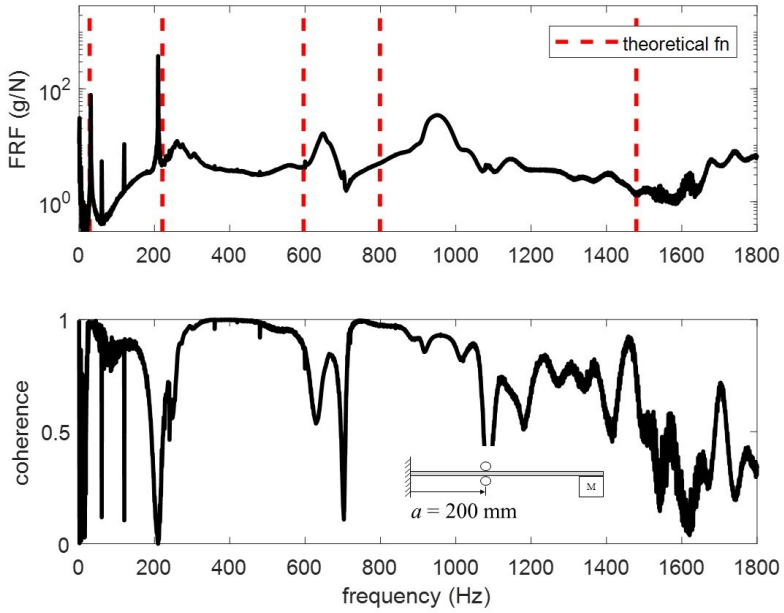

Figure 6.15: FRF for pinned at $a = 200$ mm and $\frac{m_{\text{attached}}}{m_{\text{beam}}} = 0.2$

Table 6.5: Pinned at $a = 50$ mm and $\frac{m_{\text{attached}}}{m_{\text{beam}}} = 0.2$

	Proposed model	Experiment	Difference
Mode	(Hz)	(Hz)	(%)
1	16.73	17.75	6.1
2	118.28	128.88	9.0
3	350.24	378.68	8.1
4	710.71	872.01	22.7
5	1202.46	1400.19	16.4

Table 6.6: Pinned at $a = 100$ mm and $\frac{m_{\text{attached}}}{m_{\text{beam}}} = 0.2$

Mode	Proposed model (Hz)	Experiment (Hz)	Difference (%)
1	19.48	21.37	9.7
2	141.29	157.37	11.4
3	423.53	440.11	3.9
4	864.86	996.16	15.2
5	1462.39	1680.39	14.9

Table 6.7: Pinned at $a = 150$ mm and $\frac{m_{\text{attached}}}{m_{\text{beam}}} = 0.2$

Mode	Proposed model (Hz)	Experiment (Hz)	Difference (%)
1	23.09	25.87	12.0
2	173.89	195.62	12.5
3	526.12	614.09	16.7
4	1015.61	1088.84	7.2
5	1292.51	1421.86	10.0

Table 6.8: Pinned at $a = 200$ mm and $\frac{m_{\text{attached}}}{m_{\text{beam}}} = 0.2$

Mode	Proposed model (Hz)	Experiment (Hz)	Difference (%)
1	28.02	31.39	12.0
2	221.20	259.65	17.4
3	595.97	646.99	8.6
4	798.79	950.15	18.9
5	1479.27	1741.16	17.7

6.6 Conclusion and Future Works

A high-rate experimental test bed is studied. The test bed is characterized as being a clamped-pinned-free beam with a mass at the free end. Euler-Bernoulli beam theory is applied to derive the transcendental equation for a general case applicable to the system pinned at an arbitrary location and with an arbitrary mass. The eigenvalues and mode shapes were presented under various test conditions. Experimental tests were conducted and results compared with the theoretical calculations of the first five natural frequencies. The comparison of results exhibited a good match in frequency values for the first three modes. The errors increase with the higher modes. The difference in higher modes can be attributed to the electromagnet vibrating separate to the beam, the beam vibrating within the rollers, and the rotational inertia of the mass not taken into consideration. Nevertheless, the percent difference of all modes between the theoretical and experimental values fell below 20% except for one case. These results confirm that within reason, the theory matches the experimental results. Such analytical model can be useful in designing and assessing structural health monitoring solutions validated using the high-rate experimental setup.

There still exists a need to validate algorithms on a high-rate system. Future studies will 1) address the differences in higher modes in the finite element modeling process, 2) develop a hybrid observer, and 3) implement the hybrid observer real-time on the system described in Fig. 6.11.

6.7 References

[1] J. Hong, S. Laflamme, J. Dodson, and B. Joyce, "Introduction to state estimation of high-rate system dynamics," *Sensors*, vol. 18, no. 217, pp. 1–16, 2018.

[2] R. Lowe, J. Dodson, and J. Foley, "Microsecond prognostics and health management," *IEEE Reliability Society Newsletter*, vol. 60, pp. 1–5, 2014.

[3] J. Hong, S. Laflamme, and J. Dodson, "Study of input space for state estimation of high-rate dynamics," *Structural Control and Health Monitoring*, vol. 25, no. 6, p. e2159, 2018.

[4] B. Joyce, J. Dodson, S. Laflamme, and J. Hong, "An experimental test bed for developing high-rate structural health monitoring methods," *Shock and Vibration*, vol. 2018, 2018.

[5] R. Blevins, *Formulas for natural frequency and mode shape*. Krieger, 2001.

[6] D. J. Gorman, "Free lateral vibration analysis of double-span uniform beams," *International Journal of Mechanical Science*, vol. 16, pp. 345–351, 1973.

[7] P. A. A. Laura, J. L. Pombo, and E. A. Susemihl, "A note on the vibration of a clamped-free beam with a mass at the free end," *Journal of Sound and Vibration*, vol. 37, no. 2, pp. 161–168, 1974.

[8] S. Timoshenko and D. Young, *Vibration problems in engineering*. New York: Wiley, 1974.

[9] T. C. Chang and R. R. Craig, "Normal modes of uniform beams," *Journal of Engineering Mechanics*, vol. 95, pp. 1027–1031, 1969.

[10] P. Avitabile, *Modal testing*. Wiley, 2018.

CHAPTER 7. SUMMARY

A new area of research was identified and a path for solving the high-rate problem through adaptive data-driven techniques was determined. To overcome the longer convergence times of adaptive systems, the input space of observers was studied and found to be unique to each high-rate event and it was concluded that proper selection of input space was critical to accurate estimations with fastest convergence rates. An adaptive wavelet network (AWN) estimator with self-organizing mapping was used for automatic crack detection of point cloud data generated from a terrestrial laser scanner. Through this study, the power of the universal approximation capabilities was demonstrated for the AWN. Combining the input space selection and AWN, a novel variable input observer (VIO) was developed. The VIO incorporated mutual information and false nearest neighbors algorithms to sequentially adapt the input space for utilization of a vast quantity of input observations to reduce convergence times by real-time identification of essential dynamics. Thus, a path for microsecond structural health monitoring has been established.

In particular, the contributions that this research made to the scientific community are listed as follows.

- Established a new area of research identified as high-rate state estimation, identified associated key research challenges, and presented a path to solving the problem through the use of adaptive data-driven observers determined by a literature search.
- Determined the proper input space selection has the ability to dramatically reduce the convergence times of adaptive observers.
- Validated an adaptive wavelet network for automatic crack detection.
- Developed a novel variable input observer with automatic input space selection using the embedding theorem. Through which, the application of the embedding theorem that was

previously limited to stationary data sets was made applicable to nonstationary systems by applying the theorem to stationary segments of data. Developed a smooth transitioning method between input spaces for better estimations. Identified that hybrid methods of adding knowledge of a system have the potential to outperform purely data- and model-driven strategies.

- Derived the theoretical solution to a high-rate laboratory apparatus identified as a clamped-pinned-free beam with mass at the free end using the Euler-Bernoulli beam theory. The transcendental equation was derived for a general case of the system with an arbitrary pin location and mass.

Future studies will focus on real-time application of high-rate state estimation techniques to the clamped-pinned-free beam with a mass at the free end.